Structural-Functional Brain Connectivity Underlying Integrative Sensorimotor Function After Stroke

Benjamin Thomas Kalinosky
Marquette University

STRUCTURAL-FUNCTIONAL BRAIN CONNECTIVITY UNDERLYING INTEGRATIVE SENSORIMOTOR FUNCTION AFTER STROKE

by

Benjamin T. Kalinosky, B.S.

A Dissertation submitted to the Faculty of the Graduate School,
Marquette University,
in Partial Fulfillment of the Requirements for
the Degree of Doctor of Philosophy

Milwaukee, Wisconsin

May 2016

ABSTRACT

STRUCTURAL-FUNCTIONAL BRAIN CONNECTIVITY UNDERLYING INTEGRATIVE SENSORIMOTOR FUNCTION AFTER STROKE

Benjamin T. Kalinosky, B.S.

Marquette University, 2016

In this dissertation research project, we demonstrated the relationship between the structural and functional connections across the brain in stroke survivors. We used this information to predict arm function in stroke survivors, suggesting that the tools developed through this research will be useful for prescribing individualized rehabilitation strategies in people after stroke. Current clinical methods for rehabilitating sensorimotor function after stroke are not based on the locus of injury in the brain. Instead, therapies are generalized, treating symptoms such as weakness and spasticity. This results in outcomes that are highly variable, with severity of impairment immediately following stroke as the best predictor of recovery. By using measures of brain structural and functional relations, we can better prognosticate and plan rehabilitation interventions.

This research study utilized diffusion and functional magnetic resonance imaging (MRI) to quantify anatomical connectivity and functional networks of the brain after stroke. In the first aim, diffusion MRI was used to track the white matter pathways throughout the entire brain. A new imaging biomarker sensitive to stroke lesions was developed that quantifies the level of anatomical connections between every point in the brain. It was found that cortical areas most responsible for integration of sensorimotor and multisensory integration were the best predictors of motor impairments in chronic stroke subjects. Our second aim investigated the role of multisensory integration during sensorimotor control in healthy adults and stroke survivors. A novel functional MRI task paradigm involving wrist movement was developed to gain insight into the effects of multimodal sensory feedback on brain functional networks in stroke subjects. We found that the loss of functional interactions between the cerebellum and lesioned sensorimotor area were correlated with loss of movement function. Our final aim investigated the relationship between structural and functional connectivity after stroke. A model that marries diffusion MRI fiber tracking and resting-state functional MRI was designed to enhance indirect functional connections with structural information. The technique was capable of detecting changes in cortical networks that were not seen in functional or structural analysis alone. In conclusion, structure is essential to functional networks and ultimately, recovery of functional movements after stroke.

ACKNOWLEDGEMENTS

Benjamin T. Kalinosky, B.S.

Dr. Brian D. Schmit has been a great mentor. He is the embodiment of outstanding. I would like to thank Mary Wesley for being extremely helpful. My family has kept me alive. I thank God for them. I would also like to thank everyone in the Integrated Neural Engineering and Rehabilitation Laboratory (INERL) for their assistance in pilot experiments, feedback at lab meetings, and fellowship. Dr. Sheila Schindler-Ivens and Dr. Nutta-on Promjunyakul collected the data used in my first aim. Dr. Reivian Berrios completed the clinical assessments in my second two aims.

I am honored to have had a PhD committee of rock stars, including Dr. Scott Beardsley, Dr. Peter LaViolette, Dr. Tugan Muftuler, Dr. Christopher Pawela, Dr. Sheila Schindler-Ivens, and Dr. Taly Gilat-Schmidt. They provided me with excellent feedback over the last few years.

TABLE OF CONTENTS

LIST OF TABLES

LIST OF FIGURES

CHAPTER 1: INTRODUCTION & BACKGROUND

1.1 THESIS STATEMENT

Changes in integrative structural and functional brain networks after stroke can predict functional outcomes.

1.2 IMPAIRMENT AND RECOVERY OF MOTOR FUNCTION AFTER STROKE

1.2.1 Neurophysiology of an infarct

Stroke is an event of massive cell death within the brain that results from hemorrhage or a blockage of blood from reaching the neurons. Ischemic stroke is commonly caused by an embolism of the internal carotid artery. Atherosclerotic plaques collect in the blood vessels, producing conditions that precede a stroke.

In the acute phase after stroke, there is an area around the lesion with reduced water diffusion that is thought to be irreducibly damaged. A similar area of impaired perfusion often exceeds the spatial extent of tissue with reduced water diffusion. This perfusion-diffusion mismatch area, known as the *penumbra* (Olivot et al., 2008), has enhanced oxygen extraction. An infarct can grow during the first 24 hours after an occlusion, with the amount of necrosis proportional to the drop in cerebral blood flow (Keir and Wardlaw, 2000). Inflammatory infiltration and vasogenic edema lead occur six days after the infarction. Additionally, macrophages and lymphocytes accumulate near the vasculature.

Diaschisis is the hypometabolism and neurovascular uncoupling that occur near a lesion after stroke (Wieloch and Nikolich, 2006). There are three phases to functional

recovery, which include repair from diaschisis, modification of existing networks, and new connections formed through neuroplasticity. Imaging studies have found that functional recovery is positively associated with ipsilesional supplementary motor area recruitment, while contralesional parietal and frontal activity is more reflective of incomplete recovery (Murphy and Corbett, 2009).

1.2.2 Neural basis of sensorimotor impairments after stroke

Impairments result from destroyed gray matter structures and white matter pathways. Functional deficits depend on the location and extent of the lesion. Patients with motor impairments typically have lesions to the corticospinal tract or the primary motor cortex. Damage to integrative circuits involving the cerebellum, basal ganglia, thalamus, and association cortices may also impact fine motor control and recovery.

Loss of function after stroke is not limited to motor networks, but can span a vast array of disorders in cognition, memory, language, visual perception, and auditory processing. For example, Bates *et al*. found that stroke survivors with deficits in auditory comprehension had a common lesioned area in the middle temporal gyrus (Bates et al., 2003) .

Neural repair mechanisms are limited after cortical damage, especially after the brain has fully matured. Some neurons are added to CNS throughout life. Neural stem cells exist in all ventricles but are usually dormant. Only two regions give rise to new cells. Stem cells in the subgranular zone of the dentate gyrus produce new granule cells, while stem cells in the subventricular zone of lateral ventricles produce new inhibitory neurons that migrate to the olfactory bulb.

1.2.3 Neural plasticity following stroke

Animal studies have shown that movement may be controlled through alternate motor fibers after severe damage to the corticospinal tract (Lang and Schieber, 2004). Corticospinal tract integrity measured with diffusion tensor imaging (DTI) also predicts the amount of motor cortex activation during movement in stroke (Stinear et al., 2007). One study found that during unilateral movements, the contralesional sensorimotor cortex had an inhibitory impact on the ipsilesional sensorimotor cortex that was correlated with impairment (Grefkes et al., 2008). The ipsilesional supplementary motor area had reduced functional connectivity with the contralesional sensorimotor cortex during bimanual movements. The functional connectivity within the motor network has been correlated with impairment (Sharma et al., 2009). The corticospinal tract splits into ventral and dorsal paths at the ventral pons, and the dorsal path integrity best correlates with motor function after stroke (Lindenberg et al., 2010). Also, integrity of the contralesional corticospinal tract correlates with motor skill in chronic stroke survivors (Schaechter and Fricker, 2009).

Complex tasks involving enhanced environments with interacting sensory integration and sensorimotor processes may be beneficial in stroke rehabilitation. Multisensory training has been shown to be more effective than unimodal approaches in healthy adults. Multimodal stimulation activates a broader range of functional cortical areas, and it may promote plasticity during recovery after a stroke (Johansson, 2011). Such therapies may include music, cognitive tasks, exercise, virtual reality, and

massages. Stroke survivors with left hemineglect have shown improved visuomotor performance while listening to music (Funes and Guzma, 2009).

1.3 NEURAL MECHANISMS IN SENSORY INTEGRATION AND MOVEMENT

1.3.1 Sensorimotor and multisensory integration

The motor components in the brain are organized both in hierarchy and in parallel loops (Kandel et al., 2000). Association areas "decide" that movement is needed. Premotor cortices devise a plan and pass it on to the primary motor areas, which then send commands to motor neurons. The cerebellum is heavily involved in motor planning and learning. It optimizes the error between somatosensory input and motor output by filtering commands from the primary motor cortex. The basal ganglia also modulate activity of the primary motor cortex via thalamic nuclei. However, the basal ganglia are involved in forming parallel processing loops in the brain circuitry. Motor commands from the neocortex are carried by corticospinal fibers, which pass through the posterior limb of the internal capsule. While half of the corticospinal fibers are provided by primary motor cortex and pass through the posterior limb of the internal capsule, the premotor cortex and supplementary motor area provide a third of corticospinal fibers that travel more anterior.

Without sensory feedback, fine movements are not possible. Sensory information is processed from bottom up (Kandel et al., 2000). Peripheral sensory fibers synapse to their dorsal root ganglion, which then connects to the spinal cord. This somatosensory information is relayed through a thalamic nucleus to the primary sensory cortex, S1. Low-level somatotopic cortical processes are forwarded to the somatosensory association

cortex, where neurons respond to complex combinations of somatotopic inputs. Some of this unimodal association information is sent to the prefrontal and posterior parietal multimodal association areas for planning movement. These multisensory neurons are responsible for integrating visual, auditory, and somatosensory information, which is then forwarded to the premotor cortex.

Evidence from functional imaging studies suggest that there are superadditive bimodal neurons in the posterior parietal association cortex that show high gains in activation during multisensory stimulation (James and Stevenson, 2015). It was discovered that under stimuli with a high signal to noise ratio, audiovisual activation did not reach the sum of individual auditory and visual activations. However, superadditivity was observed when stimuli with lower SNR were presented. Regions that were found to be sensitive to multimodal integration under this "inverse effectiveness" effect included superior temporal gyrus, inferior parietal lobule, medial frontal gyrus, and parahippocampal gyrus.

There exists limited knowledge of the distinguished roles of the posterior and anterior association areas in sensorimotor integration. Filimon *et al.* suggested that motor commands sent by frontal motor areas are forwarded to the posterior parietal cortex, which integrates an efference copy with sensory feedback in order to predict the current limb state (Andersen and Cui, 2009; Pynn and DeSouza, 2013). This suggests that commands begin in frontal areas before reaching the posterior parietal areas. In Filimon 2010, they pointed out that task-based fMRI and resting state fMRI both find connectivity of anterior precuneus to premotor, SMA, the posterior precuneus to the visual cortex, and the between area to the frontal association areas (Filimon, 2010).

In addition to its role as an integrator of multisensory information and motor commands, the posterior parietal cortex (PPC) projects efferents to the premotor areas for planning movements (Kandel et al., 2000). Buerze *et al*. found that the bilateral posterior parietal cortex and premotor cortex are involved in integrating target and arm cues for planning movement (Beurze et al., 2007). The parietal cortex had the greatest activity during reaching. Also dorsal premotor cortex and medial intraparietal sulcus had greater BOLD signal during uncued versus cued reaching. Another study by Filimon et al. concluded that the superior portion of the parieto-occipital sulcus participates during reaching in visual feedback (Filimon et al., 2009).

The cerebellum and basal ganglia also play an important role in both sensorimotor and multisensory integration. Loss of cerebro-cerebellar circuits due to lesions in rats impaired the ability to guide behavior with somatosensory feedback (Proville et al., 2014). Conscious awareness of a phantom limb occurs due to reduced afferent information and reorganization, specifically an abnormal open basal-ganglia-thalamocortical loop (Romero-Romo et al., 2010). There is strong evidence of integrative multisensory neurons in caudate nucleus and substantia nigra (Nagy et al., 2006). Within these structures there was an extensive coverage of multiple sensory fields.

1.4 MAGNETIC RESONANCE IMAGING

1.4.1 The MRI Signal

Each hydrogen atom from water in the human body has a single-proton nucleus that spins with a net positive charge. This high velocity charge creates a current loop, inducing a magnetic field. The magnetic moment of a proton is oriented along its spin axis. When exposed to an external magnetic field, $\mathbf{B}_0$, the magnetic moments of protons become aligned either parallel or anti-parallel to the direction of the external field. These two configurations are low energy and high energy states. Slightly more protons are in a low energy state, leading to a net magnetization, $\mathbf{M}$, in the direction of $\mathbf{B}_0$. Due to the proton's mass, its angular momentum causes the magnetic moment to tip away from the $\mathbf{B}_0$. This tipping causes the proton to precess, or wobble like a top, at the particle-specific Larmor frequency that is proportional to the magnetic field strength.

The external magnetic field is much greater in strength than the net magnetization of protons. Thus, the portion of the $\mathbf{M}$ that is parallel with $\mathbf{B}_0$, called the longitudinal magnetization M_Z, cannot be measured. However, if an external radio-frequency pulse at Larmor frequency is applied to the biological tissue, the precessing water hydrogen protons become excited. This causes more protons to enter the higher energy state, which tips the net magnetization into the transverse plane away from $\mathbf{B}_0$. Additionally, the RF pulse causes the spins to become phase-locked. Since the magnetic moments are phase-locked, their net transverse magnetization M_{XY} can be measured within the axial plane. Note that M_{XY} is the amplitude of the measured MRI signal. Once the RF pulse is turned off, the magnetic moments of the protons return to rest over time. As more protons return

to the low energy state, M_Z increases back M_0. In an independent process, the transverse magnetization M_{XY} decays back to zero due to spin dephasing. The regrowth of M_Z and decay of M_{XY} are known as T1 and T2 relaxations. T1 and T2 relaxation times are unique for white matter, gray matter, and corticospinal fluid in the brain. MRI pulse sequences are designed to give greater weight to T1 or T2 within the measured signal with amplitude M_{XY}.

1.5 DIFFUSION MRI OF WHITE MATTER

1.5.1 Diffusion-weighted MRI

Diffusion of water follows the laws of Brownian motion. If a population of water molecules beginning at the same location are allowed to move freely, they will randomly move in all directions with a spatial distribution that is Gaussian with an increasing standard deviation with time.

During an RF excitation pulse, the water protons will become phase aligned and the MRI signal will increase. If an additional magnetic field gradient is applied along one 3D direction for a fixed duration and then turned off, the protons will have differences in phase based on spatial location in that direction. This dephasing will lead to a drop in the MR signal. If a negative gradient is then applied with the same direction and duration, the protons will rephased and the MRI signal will return close to its original magnitude. However, if water molecules are allowed to diffuse over a longer period of time between the dephasing and rephasing gradients, their phase is no longer a function of location along the gradient direction. After the rephasing gradient is applied, protons of water molecules that diffused along the gradient direction will have different phases. This net

dephasing leads to an MRI signal loss due to diffusion. The diffusion coefficient of a specific tissue can be accurately estimated from this amount of signal loss by comparing the final MRI signal with and without the diffusion weighting gradients. If $S(t)$ is a diffusion weighted signal and $S_0(t)$ is the signal without diffusion weighting, then the diffusion coefficient is $D = -\frac{\ln\left(\frac{S(t)}{S_0(t)}\right)}{b}$. The b-value is a diffusion-weighting parameter controlled by the time interval between dephasing and resphasing gradients as well as the field strength of the diffusion-weighting gradient.

1.5.2 Diffusion anisotropy in white matter

It was discovered that diffusion of water in the brain's white matter is anisotropic (Chenevert et al., 1990). White matter consists of axonal fibers that are organized in parallel as densely packed fiber bundles, or fasciculi (Douek et al., 1991). Water molecules cannot penetrate the axonal membranes and are thus constrained to diffuse primarily along the fiber bundle orientation. Thus, diffusion is anisotropic in that it has a preferential direction or orientation. Basser *et al.* formulated a model that expresses the 3-dimensional distribution of diffusion coefficients as an ellipsoid, expressed mathematically as a positive-definite symmetric 3x3 tensor (Basser et al., 1994). This diffusion tensor requires at least 6 diffusion-weighted images with noncollinear gradient directions. By diagonalizing the diffusion tensor, the largest eigenvector provides the principle direction of diffusion, which was shown to match the direction of white matter fibers.

1.5.3 Models for fiber orientation

A diffusion tensor image defines an ellipsoid at every voxel, with the principle eigenvector indicating the orientation of the fiber orientation (Alexander et al., 2001). This inference is only valid under the assumption that a single orientation occupies the voxel. However, it has been shown that most voxels in the brain contain multiple fiber orientation populations due to crossing, kissing, or branching. If the partial volumes of these orientations are similar, then there is not a unique preferential direction of diffusion. Thus, the diffusion tensor becomes isotropic and fractional anisotropy misleadingly decreases.

High angular resolution diffusion MRI involves acquiring many (150-200) diffusion-weighted images in order to support higher order tensor models (Tuch et al., 2002). These models are used to calculate a voxel's diffusion Orientation Distribution Function (ODF), which is a continuous spherical function of calculated by radially integrating over the diffusion measurements (Tuch et al., 2003). Q-ball imaging uses HARDI data to model the diffusion ODF (Tuch, 2004; Tuch et al., 2003). Every diffusion measurement is expressed as a vector in q-space, where the direction matching the diffusion gradient direction and the magnitude equaling the diffusion coefficient. The b-value is kept fixed for all DWI's in order to sample a "ball" in q-space. The ODF is continuous, which requires that the HARDI data be fit a set of parameters. Some q-ball imaging studies fit the data to a linear combination of spherical harmonic basis functions or "shells". These models are effective if a high b-value is used. However, increasing the diffusion gradient strength decreases the signal-to-noise ratio considerably.

Alternative models can still detect subtler local maxima in the ODF at lower b-values. The ball-and-sticks approach (Behrens et al., 2003), supports multiple sharp local maxima overlaying a nonzero baseline level of diffusion.

1.5.4 Tractography

1.5.4.1 Deterministic Tractography

At each voxel, the primary direction of diffusion is inferred from the diffusion tensor or q-ball model. Furthermore, fiber trajectories can be reconstructed from this vector field using tractography techniques. In streamlined tractography, seed points are distributed throughout the brain or a region of interest. From each seed, a trajectory is grown by taking small steps along the principle eigenvector until a stopping condition is met. Typical stopping criteria include a minimum FA threshold or maximum tract curvature. This approach is deterministic in that each seed point has one possible trajectory, and it is used most often applied to diffusion tensor image data. Mori *et al.* in 1999 developed a fiber-assigned continuous tractography (FACT) method for streamlined tractography that could be applied to diffusion tensor image data. Note that with this deterministic approach, any seed that is placed along a fiber with result in the same reconstructed fiber. Thus, there are many degenerate fiber paths.

1.5.4.2 Probabilistic Tractography

Probabilistic tractography takes advantage of higher order diffusion models in order to estimate a full-brain spatial map of fibers connected to each voxel. The

limitations of the second order diffusion tensor model and tractography can be partially alleviated by using such an approach. If enough diffusion-weighted gradient directions are acquired to estimate the orientation distribution function, multiple fiber orientations can be modeled at each voxel. These techniques, such as q-ball imaging, allow for multiple possible fiber paths to be reconstructed from the same starting point (Behrens et al., 2003). Unlike deterministic tractography, every voxel is densely seeded from which thousands of fiber trajectories are reconstructed. The fiber reconstruction process is similar to the deterministic approach, except that the path is perturbed at every other step. These small deviations in the path are randomly introduced from the local orientation distribution, and directions with higher diffusion coefficients have greater weight. After reconstructing many fibers from a voxel, fiber counts are binned within other voxels to calculated a structural connectivity probability map. Thus, each voxel has a trajectory distribution.

A unique feature of probabilistic tractography is path propagation under uncertainty. Behrens developed an algorithm for this purpose (Behrens et al., 2003). The orientation space, estimated from the diffusion parameters, is defined as a probability density function $P(\theta, \varphi|\mathbf{Y})$, with θ and φ being 3D polar angles. Tractography is performed with a Marov Chain Monte Carlo (MCMC) Simulation using many Markov Chains (Behrens et al., 2003). Probability density function *P* is estimated with the diffusion coefficients. Directions are sampled from *P* with greater preference for directions with higher probability. The propagation is initiated with the diffusion tensor orientation estimated by least-squares. During propagation, a random direction is selected randomly from *P*, and the current trajectory **z** is moved distance *s* along the

selected direction. The first 500 steps were made without sampling P as a "burnin" (Behrens et al., 2007), after which P was sampled after every other step for up to 2000 steps.

1.6 STRUCTURAL CONNECTIVITY

Every cortical area in the human brain is densely connected to other regions, and the topology of these interactions determines its functional capacity. This provides a basis for describing the brain as a structural network, with gray matter nodes containing neuron cell bodies that communicate with other nodes through edges made up of white matter axonal fiber bundles (Kötter and Sommer, 2000).

1.7 FUNCTIONAL MRI OF GRAY MATTER

1.7.1 Neuronal activity and the BOLD signal

Ogawa *et al.* discovered that T2* signal in gradient-echo MRI scans is sensitive to the level of blood oxygenation in the brain (Ogawa and Lee, 1990). The paramagnetic properties of deoxyhemoglobin make it an intrinsic contrast agent in MR imaging. Under steady state conditions, the flow of deoxyhemoglobin in the venous beds creates a local magnetic field gradient along the blood vessel. This magnetic field gradient promotes proton spin dephasing, and thus a faster rate of T2* decay and decrease in the MRI signal. The signal change measured in these regions is known as the blood-oxygen level dependent (BOLD) contrast.

In the case of brain activation, neurons will consume ATP after firing and lead to increased levels of oxidative phosphorylation in the mitochondria. This furthermore

leads to an increase in levels of deoxyhemoglobin, which causes the T2* signal to briefly decrease. Decreased levels of oxygen lead to an autoregulatory increase in blood flow to the brain area. As blood flow increases deoxyhemoglobin is flushed out, no longer promoting spin-spin interactions. Thus, protons remain in phase longer, and the BOLD signal increases. The BOLD signal will rise for 5 seconds and then drop back slowly over another 5-10 seconds. Another consequence of increase blood flow is the dilation of veins, which causes more blood to be present without a fixed voxel volume. Since the veins are still dilated after flow returns to normal, the T2* signal undershoots the baseline. However, it rises back to baseline as the buildup of blood is relieved. This physiological process is the tissue's hemodynamic response to brain activation. Importantly, the BOLD signal is an *indirect* measure of brain activity.

1.7.2 Functional MRI acquisition

Echo-planar imaging is used to collect functional MRI data. A gradient-echo sequence allows for fast image acquisition, with a full volume collected every one to three seconds.

1.7.3 Slice-time correction, motion correction, detrending

During an EPI acquisition, data are collected slice-by-slice. Thus, the timing between slice acquisitions is equal to the repetition time (TR). Moreover, the last slice of one volume is acquired only one TR before the first slice of the next volume. In an event-related fMRI experiment, task-related activity may be detected correctly for only a small range of slices due to phase shifts throughout the volume. Furthermore, temporal

correlations may be falsely introduced or lost between different slices. The solution is slice-time correction, which involves resampling the slice data in the temporal domain such that time is uniform throughout each volume. In an interleaved approach, all even slices and then all odd slices are collected.

Subject motion is another common source of data artifacts. If a voxel is occupied by two different substances (e.g. air and gray matter), the effective signal intensity would be an average of the two uniform substance intensities. This phenomenon is known as the partial volume effect. If a subject moves during an EPI sequence, the boundary between tissues may move within or between voxels. Thus, the signal will change uniquely in each voxel based on its partial volumes. If the motion is correlated with the task parameters, then voxels with tissue boundaries oriented normal to the motion direction will be contaminated with erroneous brain activity. The image volumes can be spatially registered across time to correct for motion. However, the original data must be interpolated to calculate the corrected images. This interpolation does not correct for partial volume of multiple tissues. Motion cannot be completely corrected.

Scanner drift is another source of false changes in the BOLD signal over time. Due to nonideal scanner hardware, magnetic field heterogeneities and external field sources can lead to a low frequency drift in signal over the course of an experiment. This artifact introduces false correlations across all voxels, it is typically spatially uniform. The drift can be removed from each voxel by zeroing the mean signal and normalizing the variance over the course of a single session.

1.8 FUNCTIONAL CONNECTIVITY

Functional connectivity is the interactive communication between neural units over time. A set of voxels in the brain that share a common activation pattern form a macroscale functional network.

1.8.1 Correlation-based Functional Connectivity

The first functional connectivity MRI techniques were based on temporal correlation in the BOLD signal of two or more voxels (Friston, 1994). Behavior-related changes in functional connectivity have been observed in task-based fMRI paradigm. However, these coactivation patterns were also observed in the motor cortex at rest (Biswal et al., 1995). Calculating the correlation coefficient of a voxel's time course with the entire brain reveals one or more widely distributed functional networks. Joel *et al.* showed that seed-based connectivity maps are a weighted combination of independent spatial network maps that are extracted with later techniques based on independent component analysis (Joel et al., 2011).

1.8.2 Independent Component Analysis

The neurons within a single voxel may participate in one or more functional networks. If a voxel has high membership within multiple cortical networks, its functional connectivity distribution is greatest locally in regions that are also part of the same networks. The high degree of overlap between seed-based connectivity maps allows for common patterns to be extracted. Independent component analysis (Beckmann and Smith, 2004; Hyvarinen, 1999) techniques have been introduced to

automatically extract network components from resting-state fMRI datasets. Each independent component output from the analysis can be interpreted as a functional network. It has a time course and a spatial map that specifies the contribution of each voxel. Multiple subjects and sessions can be concatenated in time to perform a group ICA (Beckmann and Smith, 2005; Li et al., 2012), from which networks common to the group are derived. ICA requires a selected number of independent components, and methods have been proposed for automating this task based on the data (Ray et al., 2013). Subject-specific spatial maps and amplitude time courses for each network can be recalculated from the group components by using a dual regression technique (Zuo et al., 2010). From these maps, voxel-based analysis can be performed to localize network-specific changes.

1.9 STRUCTURAL AND FUNCTIONAL BRAIN NETWORKS

1.9.1 Human Connectome

The Human Connectome Project (Van Essen et al., 2013) is a current effort to map the structural and functional connections within the human brain (Sporns, 2013, 2011; Sporns et al., 2005). The term "connectome" was initially exclusive to the anatomical connections (Sporns et al., 2005). Techniques from graph theory were applied to study full-brain structural connectivity measured with diffusion MRI tractography (Bullmore and Sporns, 2009; Hagmann et al., 2008, 2007; Rubinov and Sporns, 2011, 2010). Nonetheless, the scope has evolved to incorporate functional connectomes from fMRI (Castellanos et al., 2013; Meskaldji et al., 2013; Smith et al., 2013), approaching a unified structural-functional connectome (Horn et al., 2013).

1.9.2 Predicting function from structure

Using converging evidence from functional MRI and positron emission tomography (PET), Raichle *et al.* demonstrated that a set of cortical areas form a default-mode network in the brain (Raichle et al., 2001). This network is most active when an individual is at rest with the eyes closed and is deactivated during tasks (Forn et al., 2013). It includes the posterior cingulate gyrus (BA 31/7), bilateral supramarginal gyrus (BA 40), and prefrontal cortex (BA 10), where BA is Brodman's area. These same regions were also found with diffusion MRI to have the densest anatomical connectivity, forming a structural core of the human brain (Hagmann et al., 2008). The high correspondence between the default-mode network and the structural core has been shown (Greicius et al., 2009). Since the discovery of the default-mode network, many other resting-state networks have been identified with fMRI (van den Heuvel and Hulshoff Pol, 2010).

1.9.3 Structure-function relationship in plasticity after stroke

Clinical applications of functional connectomes have been proposed (Castellanos et al., 2013). Specifically, resting-state fMRI allows for individuals to be imaged while relaxing rather than requiring a specific task. This allows for a fMRI to be incorporated into a sequence of clinical MRI scans.

1.10 IMAGING BIOMARKERS IN STROKE

1.10.1 Diffusion MRI

Diffusion weighted imaging (DWI) has become a clinical standard for acute stroke patients because it provides unprecedented contrast for ischemic tissue (Rordorf et al., 1998). Edema within the white matter near the blood-brain barrier leads to constrained water diffusion, making ischemic tissue in DWIs hypointense. Apparent diffusion coefficients of less than 5e-4 mm^2/sec indicate irreversibly damaged tissue (Seitz et al., 2005).

With the advent of diffusion tensor imaging, measures such as fractional anisotropy can detect breakdown in perilesional white matter structure even where apparent diffusion coefficients appear normal (Thomalla et al., 2004). Decreased FA within the posterior limb of the internal capsule is an indicator of motor impairment (Jang et al., 2005). Diffusion MRI tractography techniques have shown that corticospinal tract integrity is the best predictor of motor function in chronic stroke subjects (Stinear et al., 2007).

1.10.2 Functional MRI

Functional MRI has provided insight into altered cortical function following a stroke. However, resting-state paradigms have made fMRI clinically relevant due to the ease of imaging patients at rest.

1.10.3 Personalized rehabilitation based on network models

Determining the optimal strategy for rehabilitating lost function after stroke has been difficult due to high variability in functional outcome. Grouping stroke survivors into standardized treatment plans has shown to be ineffective in improving the level of recovery. Due to the limited success of standardized treatments in after stroke, there has been a recent shift in direction for towards personalized rehabilitation. Structural and functional connectivity models can account for the interactions between areas outside of the lesion. Furthermore, plastic changes in cortical organization during recovery may be explained by network models.

1.11 SPECIFIC AIMS

This study uses novel imaging and behavioral testing paradigms to examine chronic stroke sensorimotor deficits in performance involving coordinated fine motor control. Our approach will investigate fine motor performance during a coordinated wrist and forearm task. Imaging techniques will be used to characterize the associated changes in structural and functional connectivity of the entire brain. Our task will incorporate multiple conditions of wrist and forearm movement and different combinations of targeted sensory pathways. We will first characterize the relationship between global anatomical brain connectivity and chronic stroke impairments with a diffusion tensor imaging voxel-based analysis. We will then delineate functional networks involved in sensorimotor and multisensory integration using fMRI in chronic stroke subjects age-matched controls. Our last aim is to demonstrate that structural connectivity in stroke

survivors can predict differences in functional connectivity and sensorimotor impairment. Explaining differences in objective voxel-level connectivity will offer insight into how changes in overall brain structure lead to plastic changes involved in impairment and recovery in the context of complex fine motor control. Our specific aims are:

1.11.1 AIM 1: Determine whether full brain white matter structural connectivity can predict motor impairment in chronic stroke.

In our first aim, we will determine whether motor outcomes after stroke can be determined by the volume of brain tissue anatomically connected to the lesion boundary. This aim will provide the first metric based on voxel-wise structural connectivity and its application in quantifying a lesion's impact on functional outcomes after stroke. Chronic impairments in function after stroke are better predicted by overall anatomical brain circuitry than differences in regional volumes or conventional DTI metrics.

1.11.2 AIM 2: Show that functional connectivity underlying sensorimotor and multisensory integration is associated with motor function after stroke.

In our second aim, we will invoke highly integrative sensory networks in chronic stroke subjects to perturb fine motor control. This model could identify mechanistic changes in how the brain integrates sensory information during movement after stroke. We hypothesize that altered functional subnetworks involving sensorimotor integration will predict fine motor control impairment. In upper extremity motor control of higher

functioning chronic stroke subjects, perilesional voxels will have increased functional connectivity with voxels in highly integrative cortical areas.

1.11.3 AIM 3: Demonstrate the relationship between resting-state cortical networks and their anatomical connections in chronic stroke survivors.

In our final aim, we will use a novel model that incorporates voxel-based structural and functional connectivity information to identify specific neuroanatomical networks involved in sensorimotor integration and visuospatial attention during fine motor control. This aim's results will offer the first quantification of temporal and spatial motor coordination associated with the cost of multimodality sensory processing in stroke.

CHAPTER 2: WHITE MATTER STRUCTURAL CONNECTIVITY IS ASSOCIATED WITH SENSORIMOTOR FUNCTION IN STROKE SURVIVORS

2.1 INTRODUCTION

Diffusion tensor imaging (DTI) of brain white matter structural connectivity may have prognostic value for acute stroke patients at risk of motor impairment. In particular, DTI of the corticospinal tract has been a primary focus for predicting stroke severity and clinical outcome (Thomalla et al., 2004; Puig et al., 2010). In the corticospinal tract of stroke survivors, DTI measures that indicate structural integrity in white matter correlate with muscle strength (Chen et al., 2008; Puig et al., 2010; Schulz et al., 2012), walking ability (Jayaram et al., 2012) hand function and motor recovery (Thomalla et al., 2004; Schaechter and Fricker, 2009; Lindenberg et al., 2010; Vargas et al., 2012). Corticospinal tract size and damage to the corticospinal tract, estimated using DTI in the acute setting, also correlate with long-term recovery (Parmar et al., 2006; Pannek et al., 2009; Zhu et al., 2010). In addition to the natural recovery from stroke, information about corticospinal tract loss predicts the extent of motor recovery obtained from therapeutic interventions (Stinear et al., 2007; Riley et al., 2011). Thus, the predominant approach in developing imaging biomarkers in stroke survivors has been corticospinal tract-specific measures based on manually-identified or atlas-based regions of interest (Borich et al., 2012). These previous approaches highlight the potential value in utilizing DTI data to predict functional outcomes; however, analyses based on specific regions of interest require subjective region selection, and might not account for impairments associated with damage to or connections to other regions of the brain. The purpose of the current study was to develop and test a new imaging parameter as a biomarker for

sensorimotor function in stroke survivors based on a whole brain, voxel-wise analysis of anatomical connectivity.

Although DTI measures of the corticospinal tract provide valuable information about stroke, a whole brain voxel-based analysis of brain structure might have advantages over corticospinal tract region of interest approaches. Namely, voxel-based analyses are simple to apply, objective, and test the structural changes across the entire brain. A voxel-based analysis involves the normalization of images (through registration and spatial filtering) followed by statistical comparisons of DTI parameters of the resulting maps (Wright et al., 1995; Ashburner and Friston, 2000). These analyses have been applied to DTI parameters of the brain in normal development and aging (Della Nave et al., 2007; Snook et al., 2007), following traumatic injury (Bendlin et al., 2008; Chu et al., 2010) and during progressive disease (Agosta et al., 2007; Thivard et al., 2007; Sage et al., 2009). Conversely, there are limitations to voxel-based analyses including dependence on the quality of image registration across subjects and effects of smoothing applied to the images (Ashburner and Friston, 2001; Bookstein, 2001; Abe et al., 2010; Van Hecke et al., 2011). Consequently, an alternative voxel-based approach for assessing brain white matter, Tract-Based Spatial Statistics (TBSS) (implemented within the FMRIB Software Library (FSL)) has been developed (Smith et al., 2006). This technique accounts for the registration and smoothing issues by using a tract ‘skeleton’ obtained from fractional anisotropy (FA) values. In addition to a number of other applications, TBSS has been applied to the brain of stroke survivors and detects FA changes in white matter tracts that correlate to upper extremity function (Schaechter and Fricker, 2009).

Incorporating measurements of white matter structural connectivity of the brain within DTI voxel-based approaches may offer additional opportunities for the characterization of structural changes after stroke. The loss of white matter tracts after stroke has implications throughout the brain, including functional processes that require the integration of information from multiple brain areas. The primary tool for characterizing the structural connectivity between brain regions is DTI tractography (Conturo and Lori, 1999; Jones and Simmons, 1999; Mori et al., 1999). The results of tractography models have been used to identify anatomical tracts and features of the tractography analysis, such as the number of fibers passing through a voxel (Roberts et al., 2005; Calamante et al., 2010). A structural connectivity matrix can then be obtained by combining white matter fiber trajectories with gray matter anatomical regions of interest segmented from a high resolution anatomical MR image (Hagmann et al., 2007; Sporns, 2011). This matrix represents the anatomical connectivity of the specific regions of the brain, but depends on the parcellation of specific regions of gray matter as nodes in the connectivity matrix. In contrast, voxel-based connectivity models make no assumptions about the parcellation of voxels into ROIs, nor do they require a proiri knowledge about the physiology of the tissue within that voxel (Scheinost et al., 2012). The absence of assumptions in a voxel-based approach is appealing for generalizing connectivity models for clinical application.

In this study, we developed a unique metric of structural connectivity as a biomarker for loss of sensorimotor function in subjects with chronic stroke. Our metric characterized the anatomical connectivity of each voxel of the brain based on diffusion tractography (i.e. a voxel-wise indirect structural connectivity (VISC)). This VISC

metric was designed to have high sensitivity to lesions of prominent white matter tracts, which normally connect large numbers of voxels. A voxel-based analysis of stroke and control brains was conducted on the VISC metric and compared to a voxel-based analysis of FA and mean diffusivity in the same samples. Sensitivity to sensorimotor function was tested by correlating the volume of differences in VISC, between stroke subjects and controls, with sensorimotor impairment measured by the Fugl-Meyer Assessment (Fugl-Meyer, 1975).

2.2 METHODS

2.2.1 Data Collection

2.2.1.1 Subject Recruitment and Fugl-Meyer Testing

Ten subjects with chronic post-stroke hemiparesis (5 female, age 55.20 ±7.06 years, at least 1.1 years since stroke) and nine age-matched control subjects (6 female, age 53.40 ±13.10 years) participated in this study. Each subject provided written consent to the experimental protocol, which was approved by the Institutional Review Boards at Marquette University and the Medical College of Wisconsin. In recruiting subjects, a sample of convenience was used. General inclusion criteria were ability to provide informed consent and the ability to move the legs with no contraindications to light exercise. Additional inclusion criteria for stroke survivors were a single cortical or subcortical stroke at least 6 months earlier, clinically detectable movement impairment on one side of the body, communication adequate to follow instructions for the experiment,

and no neurological impairments other than stroke. Control subjects had to be free of stroke or other neurological impairments.

Each stroke subject completed a slightly modified upper extremity (UE) and lower extremity (LE) portions of the Fugl-Meyer (FM) Assessment (Fugl-Meyer, 1975) for global impairment (maximum possible score is 130 for UE and 96 for LE). The scoring system for the FM Assessment is shown in Table 2-1, and the FM scores for each subject are shown in Table 2-2. Note that lower scores indicate greater impairment. FM assessments were completed by a physical therapist with 9 years of clinical experience. Reliability and validity assessments were not done for this study; however, the FM has been shown to have excellent construct validity, good concurrent validity with other stroke motor scores, satisfactory predictive validity for functional level at discharge from hospital (r=0.72), and excellent intra- and inter-tester reliability (ICC=0.98) (Gladstone et al., 2002; Hsueh et al., 2008). The maximum score for the UE portion of FM is 130 because it includes UE reflexes (max=6), UE movements in and out of synergy (max=30), voluntary movements of the wrist and hand (max=24), and UE coordination (max=6), parachute responses (max=4), UE light touch (max=4), UE proprioception (max=8), UE ROM (max=24), and UE pain (max=24). Nevertheless, the scale required adjustment to better reflect the possible range of scores. Since the control subjects did not have any lesions and the Fugl-Meyer assessment is a measure of impairment, sensorimotor function in control subjects was not tested.

2.2.1.2 MRI Scans

After completing MRI safety screening, the nineteen subjects were imaged with a 3T clinical MR system (GE Signa Excite, GE Healthcare, Milwaukee). For each subject, an axial DTI sequence was acquired with one b0 image, 25 noncollinear, equally spaced diffusion directions, b-value = 1000 s/mm2, matrix = 128 x 128, FOV = 24 cm, slice thickness = 4 mm, TE = 86.5 ms, TR = 10 s, NEX = 2. As an anatomical reference, a sagittal T1-weighted image with 1 mm isotropic resolution was acquired using a spoiled gradient recalled (SPGR) pulse sequence.

Fugl-Meyer Scoring System	Maximum Possible Score
Grand Total	226
UE + LE Motor	100
UE + LE Balance	14
UE + LE Sensation	24
UE + LE ROM	44
UE + LE Pain	44
UE Total	130
UE Motor	66
Parachute Responses	4
UE Light Touch	4
UE Proprioception	8
UE ROM	24
UE Pain	24
UE Motor Total	66
UE Reflexes	6
UE Movements in and out of Synergy	30
Voluntary Movements of Wrist and Hand	24
UE Coordination	6
LE Total	96
LE Motor	34
Standing Balance	8
Sit without Support	2
LE Light Touch	4
LE Proprioception	8
LE ROM	20
LE Pain	20
LE Motor Total	34
LE Reflexes	6
LE Movements in and out of Synergy	22
LE Coordination	6

Table 2-1: Description of the Fugl-Meyer scoring system used in this study.

Table 2-2: Descriptive characteristics of stroke survivors.

UE=upper extremity, LE=lower extremity, max=maximum possible score obtainable, f=female, m=male.

Subject ID	Sex	Age (years)	Time Since Stroke (years)	Lesion Location	Paretic Side	Fugl-Meyer UE + LE Score						Fugl-Meyer UE Only		Fugl-Meyer LE Only	
						Total (max=226)	Motor (max=100)	Balance (max=14)	Sensation (max=24)	ROM (max=44)	Pain (max=44)	Total (max=130)	Motor (max=66)	Total (max=96)	Motor (max=34)
S01	f	60	20.4	Cort	R	170	75	11	3	37	44	93	45	77	30
S02	m	53	8.3	Cort	L	143	51	10	7	31	44	70	26	73	25
S04	m	61	5.3	Cort	R	207	87	10	23	43	44	130	66	77	21
S10	f	58	6.1	Cort	L	169	71	10	22	30	36	90	47	79	24
S11	f	53	17.4	Subcort	R	218	92	14	24	44	44	127	61	91	31
S13	m	46	4.4	Subcort	R>L	169	58	10	24	33	44	99	39	70	19
S14	f	52	4.3	Cort	L	152	49	8	24	37	34	68	22	84	27
S15	m	48	8.1	Cort	R	144	35	10	22	33	44	71	18	73	17
S17	f	65	6.2	Cort	L	124	32	8	4	36	44	58	14	66	18
S19	m	55	6.4	Cort	R	194	74	12	24	40	44	101	42	93	32

2.2.2 Subject-Specific Data Processing

2.2.2.1 Diffusion Tensor Calculation

From the diffusion weighted images acquired for each subject, twenty-five diffusion coefficients were calculated at each voxel as the signal loss between the diffusion-weighted signal and zero-diffusion signal. These diffusion coefficients were fit to a second order tensor model by the least squares method. The diffusion tensor matrix was then diagonalized to derive three eigenvalues and eigenvectors. The three eigenvalues ($\lambda_1, \lambda_2, \lambda_3$) were used to calculate the MD and FA (Basser et al., 1994).

2.2.2.2. Image Registration

Anatomical brain images from all control and stroke subjects were registered to a reference image (Fig 2-1b) in order to compare DTI metrics between individual stroke subjects and the control group. The control subject with characteristics closest to Talairach space was selected as the reference. Each subject's T1-weighted image was then registered to the reference subject using a deformable image registration framework implemented in Tactful Functional Imaging Research Environment (TFIRE, http://www.eng.mu.edu/inerl/tfire), an in-house Java-based software platform. A nine-parameter affine transform was performed before proceeding with Thirion's demons deformable image registration method (Thirion, 1998). The output from this process was a 3D displacement field that mapped each voxel center in the fixed reference control space to a physical location in the subject space.

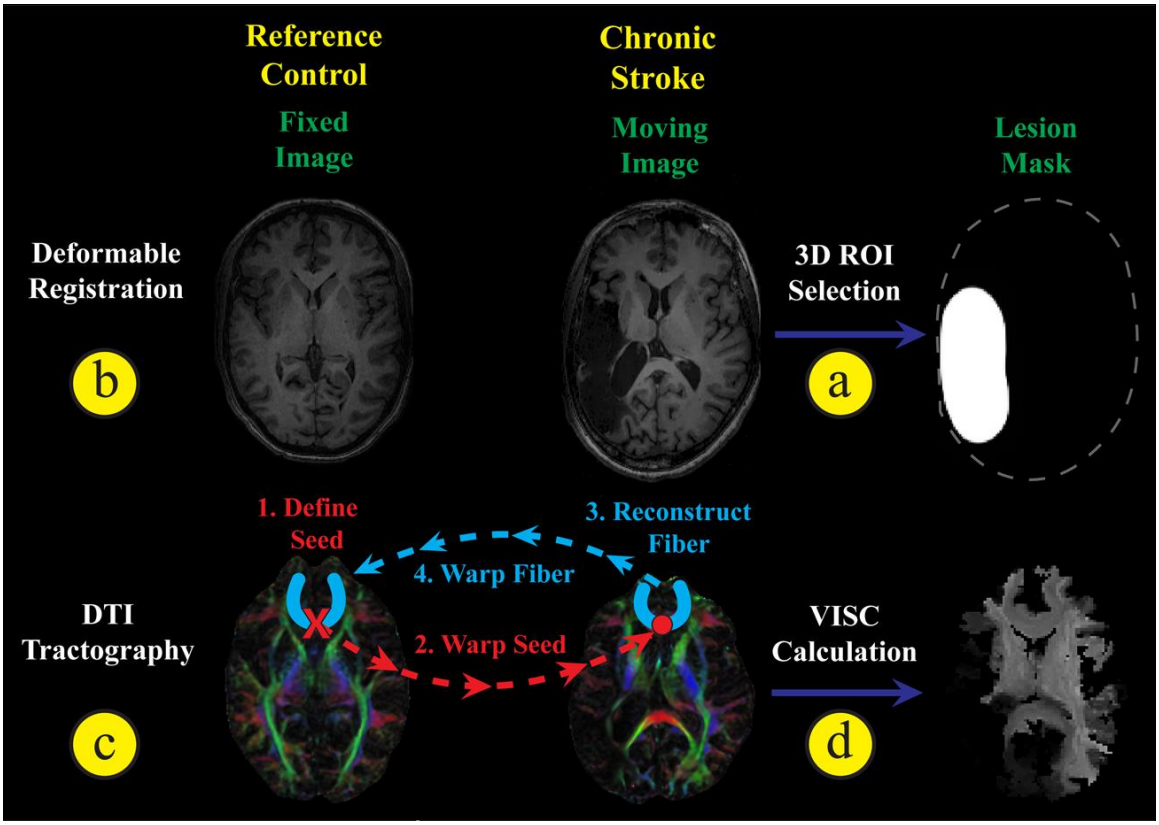

Figure 2-1: Overview diagram of image processing.

Overview of image registration, DTI tractography, and VISC calculation. (a) A lesion mask was manually selected from the stroke subject's SPGR image, and then (b) the stroke subject was registered to the reference control subject. (c) The registration transform was used to warp seeds from the reference control space to perform DTI tractography in the stroke subject's space. Reconstructed fibers were then transformed back into the reference control space and (d) used to perform structural connectivity analysis. Furthermore, a novel voxel-wise indirect structural connectivity (VISC) metric was calculated.

2.2.2.2.1 Stroke Lesion Selection and Correction

Initial registration results for stroke subjects were determined unacceptable based on visual observation. In particular, areas in the control image were mapped to the lesion boundary of the stroke subject. Lesion masking and a modified smoothness constraint were introduced to preserve anatomical features near the lesion boundary (Fig 2-2). A lesion mask was manually identified for all slices using a custom user-interface.

Although some lesions were discontinuous in some slices, they were not broken up volumetrically. Only one contiguous unilateral lesion was selected for each subject. During the registration, displacements that mapped the fixed image to locations inside the lesion mask region were not updated. An edge-preserving Gaussian filter was used to impose piece-wise continuity. This modified filtering allowed tissue surrounding the lesion to register, while preserving the lesion features.

2.2.2.2.2 Inverse Deformation Estimate

Aside from challenges with stroke lesion mapping, the deformable registration was performed in a small deformations setting, which led to a non-invertible deformation field. However, an inverse transform was needed for our subsequent tractography approach. We mitigated this problem by approximating an inverse with the following method. First, a 3D displacement field was initialized to zero at each location. The forward transform was used to map each physical coordinate in the fixed subject image space to a location in the reference (control) image space. The displacement of the inverse transform at this location was forced to map back to the fixed image coordinate. Since this update step resulted in inhomogeneous mappings in the fixed image space, the inverse transform was smoothed with a 2 mm full-width half-max Gaussian filter. The update and smoothing steps were repeated for 10 iterations. This iteration number was chosen heuristically to balance the tradeoff between computation time and residual error. The mean and standard deviation of the final error magnitude across subjects was 0.5622 ± 0.3326 mm. This process produced forward and inverse transformations between each

subject and the reference control based on the anatomical (T1 weighted) images. These transformations were subsequently used for the diffusion image data.

2.2.2.2.4 Diffusion to Anatomical MRI

In order to use the anatomical image transformations for aligning the subjects in DTI space, each subject's T1-weighted image was registered to his or her FA image. The SPGR and FA images were histogram-matched, and then a nine-parameter 3-dimensional affine transformation was optimized using a gradient descent algorithm with a mean squared difference cost function.

2.2.2.3. Tractography and Voxel-wise Indirect Structural Connectivity Metric

2.2.2.3.1 DTI Tractography

Our in-house software, TFIRE, was also used for DTI tractography (Fig 2-1c) and structural connectivity analysis (Fig 2-1d). We chose to define of a voxel by the location of its center. This convention allowed for a straight-forward one-to-one mapping between a connectivity matrix and an image space. Further detail is provided in the Appendix.

Using the reference control DTI image, tractography was initialized by seeding with uniform 1 mm spacing in all areas with an FA above 0.3. The coordinate of each seed was transformed from control into subject space. The FACT method (Mori et al., 1999) was implemented in TFIRE and used to reconstruct fiber trajectories seeded at each voxel center. Specifically, the principle eigenvector with an FA magnitude was

integrated using a 4th order Runge-Kutta technique with a step size of 0.1 mm. A maximum angle of curvature of 60 degrees was used to terminate propagation at voxels with crossing white matter fiber bundles. Since the endpoints of fibers often converge at gray matter voxels, a minimum FA stopping criterion of 0.15 was used to allow the fibers to propagate into the gray matter. Including white matter voxels in the VISC calculation was intended to account for bifurcating and converging fiber pathways. After construction was completed, all fibers with length < 1 cm or > 14 cm were excluded. Each reconstructed white matter fiber was transformed back into the reference control space using the inverse registration transform.

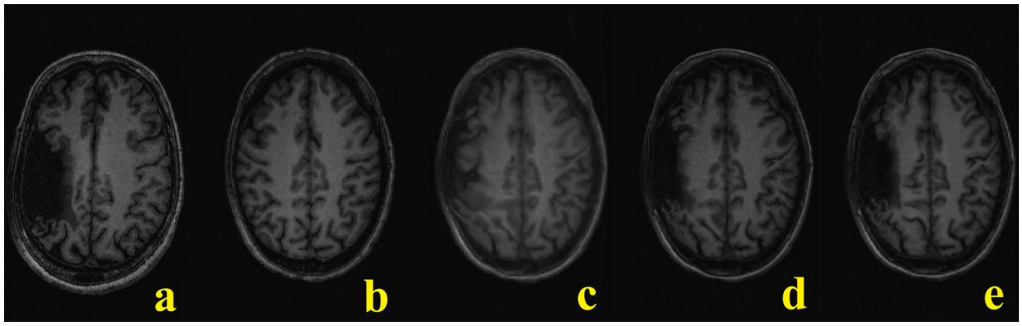

Figure 2-2: Stroke image registration.

In registering a stroke brain (a) to the template control (b), the original deformation algorithm (c) was modified to include lesion masking (d) and anisotropic smoothing (e) to produce the best result.

2.2.2.3.2 Theoretical Framework

In order to model the effects of a stroke lesion at the voxel-level, a measure of voxel-wise indirect structural connectivity (VISC) was developed. The desired properties of VISC were to reproducibly amplify lesion-induced effects on white matter structural

connectivity of the entire brain, and to intrinsically measure these effects at the voxel-level. We started by defining the structural connectivity of the whole brain based on the voxel-wise direct and indirect connections obtained from DTI tractography (Fig 2-3). As an example, consider an axonal fiber pathway that structurally connects three voxels; A, B, and C in Figure 2-3. We defined B and C to be direct neighbors to A by their structural connection. There are also axonal pathways that connect B or C to voxels other than A. These pathways indirectly connect A to voxels D, E, and F, which we define as indirect neighbors of voxel A. A connectivity graph for this example is shown in Figure 2-3b. The VISC of voxel A is the average number of connections to indirect neighbors D, E, and F. Since F has one direct connection, and D and E each have two direct connections, the VISC of A is 5/3.

2.2.2.3.3 Voxel-wise Indirect Structural Connectivity (VISC) Calculation

As a foundation for deriving a voxel-wise connectivity metric, the reconstructed fiber trajectories were expressed as sets of coordinates in the template control subject's DTI image-space. Binary matrix $\tilde{\mathbf{X}}$ represents the direct connectivity between the voxels penetrated by one reconstructed fiber, where $\tilde{x}_{ij}$ is 1 if the i^{th} and j^{th} voxels are both penetrated by that fiber and 0 otherwise. Matrix $\mathbf{X}$ represents the direct connectivity between all voxels in an image, where x_{ij} is 1 if the i^{th} and j^{th} voxels are both penetrated by at least one fiber and 0 otherwise. Thus, $\mathbf{X}$ is the union of individual $\tilde{\mathbf{X}}$ across all fibers. Directly calculated from $\mathbf{X}$, matrix $\mathbf{Y}$ represents the indirect connectivity between all voxels in an image, where y_{ij} is 1 if the i^{th} and j^{th} voxels share a

directly connected voxel but are not directly connected to one another. Then row vector $\mathbf{y}_{(i)}$ from $\mathbf{Y}$ represents the indirect connections of the i^{th} voxel. Using 1 as the summation vector, the VISC of the i^{th} voxel in an image is its total number of direct connections to its indirect neighbors (expressed as $\mathbf{y}_{(i)}\mathbf{X1}$) divided by its total number of indirect neighbors (expressed as $\mathbf{y}_{(i)}\mathbf{1}$).

$$\mathrm{VISC}_i = \frac{\mathbf{y}_{(i)}\mathbf{X1}}{\mathbf{y}_{(i)}\mathbf{1}} = \frac{\sum_j^N \left(y_{ij} \sum_k^N x_{jk} \right)}{\sum_j^N y_{ij}} \qquad \text{(Eq. 1)}$$

Previously introduced voxel-wise metrics based on DTI tractography, such as fiber count and mean fiber length (Roberts et al., 2005), are correlated with FA. In order to consider whether fiber count information affected the correlation of VISC with FA, we incorporated a connection count weighting factor α. This contrast mechanism gives weight to the total number of connections to a voxel's indirect neighbors. As α is decreased from 1 to 0, the VISC approximates the *total number* rather than the *mean number* of direct connections to a voxel's indirect neighbors, with VISC parameterized by α as

$$\mathrm{VISC}(\alpha)_i = \frac{\mathbf{y}_{(i)}\mathbf{X1}}{(\mathbf{y}_{(i)}\mathbf{1})^{\alpha}} . \qquad \text{(Eq. 2)}$$

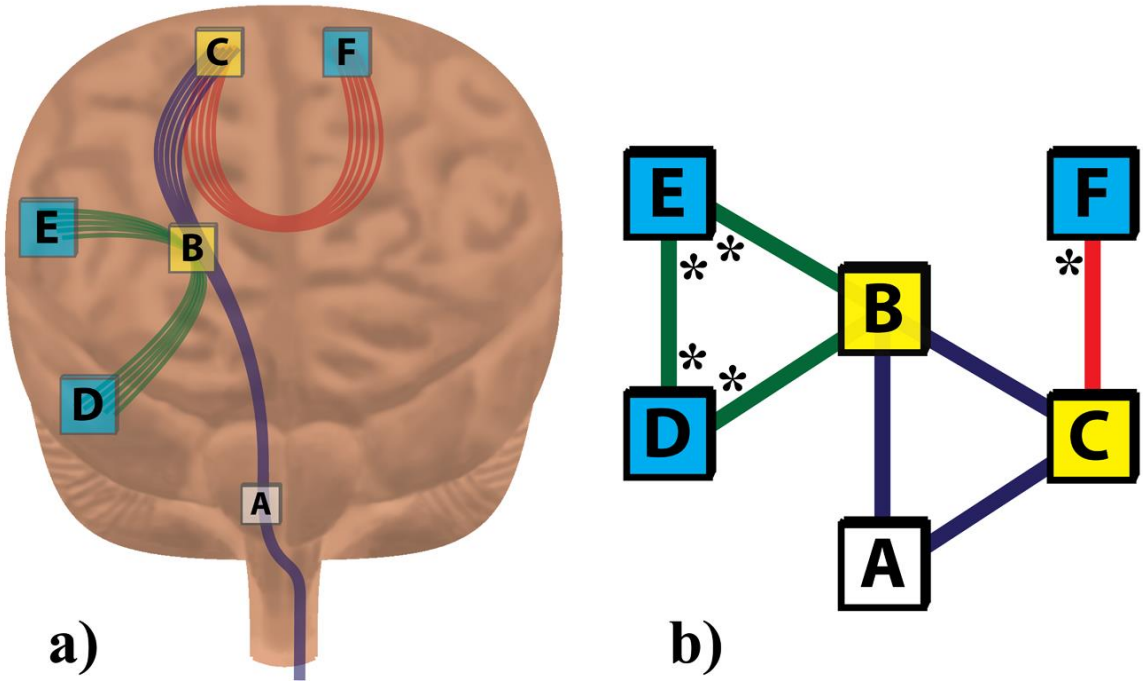

Figure 2-3: Example calculation for VISC.

The "anatomical" diagram (a) and the theoretically equivalent network graph (b) provide the information necessary to calculate the VISC of voxel A. Voxels B and C (yellow) are directly connected to voxel A by at least one common fiber. Voxels D, E, and F (aqua) are indirect neighbors to voxel A because they are not directly connected to A by any fiber but do share a common direct neighbor (B or C) with A. The VISC of voxel A is the average number of direct connections to its indirect neighbors. These direct connections are marked with an * in (b). Since there are 5 total direct connections for its 3 indirect neighbors, the VISC of voxel A is 5/3.

2.2.2.4 Effect of tractography parameters and contrast parameter α on VISC

Parameters used for tractography and VISC connection weighting were manipulated to determine their effect on the final VISC value. Since VISC is derived from DTI tractography, it is expected to depend on the stopping criteria for fiber propagation. We considered that VISC might decrease as FA threshold increased due to a more conservative stopping criterion. If the minimum FA is increased, then propagation ends more readily and reconstructed fibers are shortened. Thus, the spatial distribution of reconstructed white matter fibers decreases in volumetric extent as FA threshold increases. Since VISC is based on structural connectivity with surrounding and distant voxels, it can also be interpreted as a volume-based metric. If the volume of the spatial extent of fibers decreases proportionally with increased FA threshold, then the percent change in volume is higher at lower FA thresholds. Thus, the logarithm of the volume of VISC was expected to be negatively correlated with the FA threshold. To test this hypothesis, we calculated the mean VISC of 3 voxels selected from the center of each of the cerebral peduncles, which are known to have a high anatomical fiber density. The purpose of selecting only 3 voxels was to understand how the VISC in ipsilesional voxels and their contralesional "equivalent" were affected by FA threshold in anatomical regions of high fiber density. We manipulated the FA threshold from 0.10 to 0.40 in increments of 0.05, and the mean VISC of the cerebral peduncle ROI was calculated for each FA threshold setting. Correlation analyses were performed between the mean VISC and FA threshold. The analysis was repeated for the left and right ROIs of the control subjects, and the ipsilesional and contralesional ROIs of the stroke subjects. A whole-

brain analysis was also performed in which the VISC and FA were correlated across all voxels with nonzero VISC in the reference control brain.

Since high FA may be an indicator of anatomical white matter fiber density, a voxel-wise metric based on DTI tractography might correlate with FA. For example, the fiber density index (FDi) introduced by Roberts *et al*. represents the number of fibers penetrating a voxel and was found to be correlated with FA (Roberts et al., 2005). In every subject, the FA and VISC were regressed across all voxels in the reference space. This whole-brain correlation analysis was repeated for 11 settings of α in order to understand the effects of α on the correlation between VISC and FA. The mean and standard deviation of R^2 values were plotted for each VISC setting. The R^2 values with FA were also plotted for mean fiber length and fiber count for visual reference.

Beyond the effects of tractography stopping criteria, we also considered that the total number of connections to a voxel might influence VISC or its correlation to FA. If the number of structural connections to a voxel increases with greater FA, then it is possible that greater connection number weighting (decreasing parameter α) might increase the correlation between FA and VISC. The direct effect of total connections on VISC was qualitatively analyzed by manipulating α from 0 to 1 and visualizing the changes in the contrast of the reference control's VISC image.

2.2.2.5. Statistical analyses

2.2.2.5.1. Whole-brain analysis

A whole brain voxel-based analysis was used to compare each stroke subject to the controls. For each voxel, a one-tailed Student's t-test was performed on the differences of the 9 controls with a single stroke subject, with a zero mean difference null hypothesis. The resulting number of significant voxels, or difference volume, was considered as a possible predictor of Fugl-Meyer score. This difference volume can also be interpreted as the percent of effected brain volume. As the difference volume becomes large, a further increase leads to a lower percent change in volume. Consequently, we expected that increasing the size of a small difference volume would lead to a greater percent change in impact on function. Thus, we hypothesized that the log number of significant voxels, or logarithmic difference volume (LDV), would increase as Fugl-Meyer score decreased. A simple linear regression was performed for each DTI metric, with its LDV as a predictor of Fugl-Meyer score in stroke subjects. Separate regressions were conducted for FA, VISC, and MD using Matlab (R2009b, The Mathworks, Natick, MA). For each regression, an F-test was used to test the slope for significance. In a second set of simple linear regressions, the mean FA and VISC in the ipsilesional hemisphere were regressed against total FM score. In order to prevent voxels with zero VISC from contaminating the mean VISC, the means were first calculated for only voxels with a nonzero VISC. However, the regression was also repeated with all iplesional voxels included. In summary, nine simple linear regressions were performed in the whole-brain analysis, with three tests per voxel-based measure.

Four multiple linear regressions were performed to determine the unique relationships between the differences in DTI measures and sensorimotor impairments. The Fugl-Meyer score was divided into subcomponents with two strategies. The first approach split the FM score into its five domains; motor (100 max), balance (14 max), sensation (24 max), range of motion (44 max), and pain (44 max). The second approach divided the total FM into two groups: upper extremity (130 max) and lower extremity (96 max). The whole-brain LDVs of VISC, FA, and MD were regressed as predictors of each set of FM subscores. Two more multiple linear regressions were performed, with the *mean* VISC, FA, and MD in the ipsilesional hemisphere as the independent variables. In all multiple regression tests used in this study, multiple comparisons correction was performed by dividing the Type I Error rate, α, by the number of metrics, being 3.

Although the VISC metric was developed for the purpose of enhancing detection of the effects of brain lesions, the unknown variability of VISC in the control group could compromise the calculation of the difference volume. The intersubject reproducibility of VISC within the control group was tested by calculating the whole-brain LDV between each control subject and the other controls. We found zero significantly different voxels in every control subject. Lesion selection could also affect the reproducibility of VISC in an image. A second investigator reselected all lesions, and then image registration and analyses were repeated. Across all voxels and subjects, the percent difference in VISC due to lesion selection was 1.52 ±0.37%. Lesion-selection did not change the findings in this study.

2.2.2.5.2. Region-based *post hoc* analysis

Since we expected the logarithmic difference volume (LDV) within specific brain region to reflect its volume of effect, a region-based correlation analysis was performed. Using the same registration algorithm performed on the T1-weighted images, the fractional anisotropy image of the template control was registered to the Johns Hopkins University "Eve" atlas (Oishi et al., 2009) in Talairach coordinates, also named JHU-Talairach-ss in MRIStudio. The registration transform was used to warp 85 ipsilesional regions of interest (ROIs) from the atlas space into the reference control space. For each ipsilesional ROI, the same set of simple linear regressions used in the whole-brain analysis was repeated.

If the total number of significantly different voxels in a particular region were correlated with Fugl-Meyer, then the raw measurement itself may share that correlation. To address this question, linear regressions were performed with the *mean* VISC, FA, and MD of every ipsilesional ROI in stroke subjects as a predictor of FM score. As with the regressions involving the log difference volumes, an F-test was used to test each slope for significance. In comparison to mean FA and MD, we expected that the mean VISC would correlate with FM score in an additional set of effected regions distant from a lesion.

2.3 RESULTS

2.3.1 Comparison of VISC, fiber count, and mean fiber length

VISC was compared with fiber count and mean fiber length by adjusting parameter α (Fig 2-4a, 2-4b). Fiber count was calculated as the number of fibers penetrating a voxel, and mean fiber length was calculated as the average physical length of these fibers. These two measures were sensitive to the number of degenerate fibers passing through a voxel, which led to undesired local hyperintensities. If α was set to zero in Eq. (2), then the denominator of VISC became 1, which equated VISC with its numerator, . In this case, VISC was greatest in voxels with a high calculated fiber count and number of direct connections. As α was increased from 0 to 0.7, the VISC metric provided an enhanced contrast similar to mean fiber length. This similarity was a consequence of including all white matter voxels in the VISC calculation. Setting $\alpha = 1$ was determined to minimize inter-subject variability between controls. Although α was an important parameter in developing the VISC metric, Eq. (1) was used to calculate VISC in all group analyses.

2.3.2 Weak correlations of FA with VISC, mean fiber length, and fiber count

In order to compare the correlations of FA with multiple DTI tractography-derived metrics, the coefficient of determination between each metric and FA was calculated in each subject across all voxels with an FA above 0.15 (a stopping criterion during tractography). These metrics included mean fiber length, fiber count, and VISC at

11 different settings of α from 0.0 to 1.0 (Fig 2-4b). The R2 values of individual subjects are listed in Table 2-3. Subject sample mean and standard deviation of R2 values were calculated for each metric. The correlation of FA with VISC suggested a small but significant portion of VISC variability can be predicted by the FA (R2=0.184±0.033). As a point of reference, the correlations between FA and mean fiber length (R2=0.199±0.041), and fiber count (R2=0.140±0.041) were comparable. As α was decreased from 1.0 to 0.0, the correlation between VISC and FA increased until α=0.7, which then decreased as α was further adjusted 0.7 to 0.0.

2.3.3 Tractography minimum FA stopping criterion correlates with VISC

As expected, the mean VISC decreased exponentially as minimum FA threshold (tractography stopping criterion) increased. The logarithm of the mean VISC metric was strongly correlated (R2=0.991±0.007) with tractography FA threshold across subjects. The log mean contralesional and ipsilesional VISC were both lower than controls for all FA thresholds (Fig 2-4c); however, FA thresholds less than 0.15 led to the greatest contrast between control and stroke VISC. At greater FA thresholds, the difference in VISC between the left and right cerebral peduncles increased in control subjects and decreased in stroke subjects. Although we selected an FA threshold of 0.15 in correspondence to past literature (e.g. An FA threshold of 0.18 was used in (Chen et al., 2008)), our results suggested that this threshold was optimal for contrasting controls with chronic stroke subjects. Across all voxels in the normalized space, the correlation between VISC and FA threshold was R=-0.950±0.044, and the correlation between log(VISC) vs. FA threshold was R=-0.978±0.025.

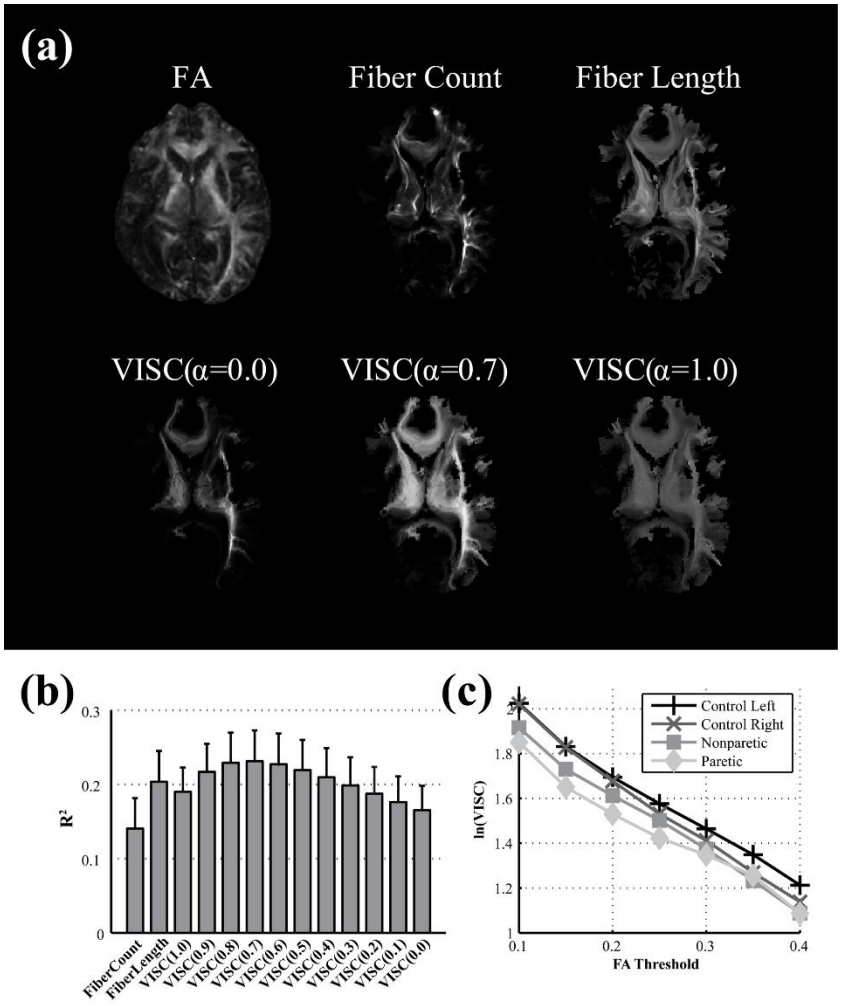

Figure 2-4: VISC correlations and contrasts.

(a) Visual comparison of VISC, fiber count, and mean fiber length for a central axial slice of a stroke subject at the level of the internal capsule. The indirect connectivity weighting factor, α, was manipulated from 0 to 1 to observe its effect on the spatial contrast of VISC. (b) The R2 values of FA with several tractography-derived measures. The VISC at different settings of α are labeled as VISC(α) (e.g. VISC(1.0) for α=1.0). The mean and standard deviation in R2 values are across all 19 subjects included in this study are shown. (c) The natural log of the mean VISC in the cerebral peduncles is plotted against the minimum FA threshold used as a stopping criterion for DTI tractography. The same bilateral ROIs were used to report this relationship in the paretic/ipsilesional (diamond) and nonparetic/contralesional (square) hemispheres of stroke subjects, and the left (+) and right (x) hemispheres in control subjects.

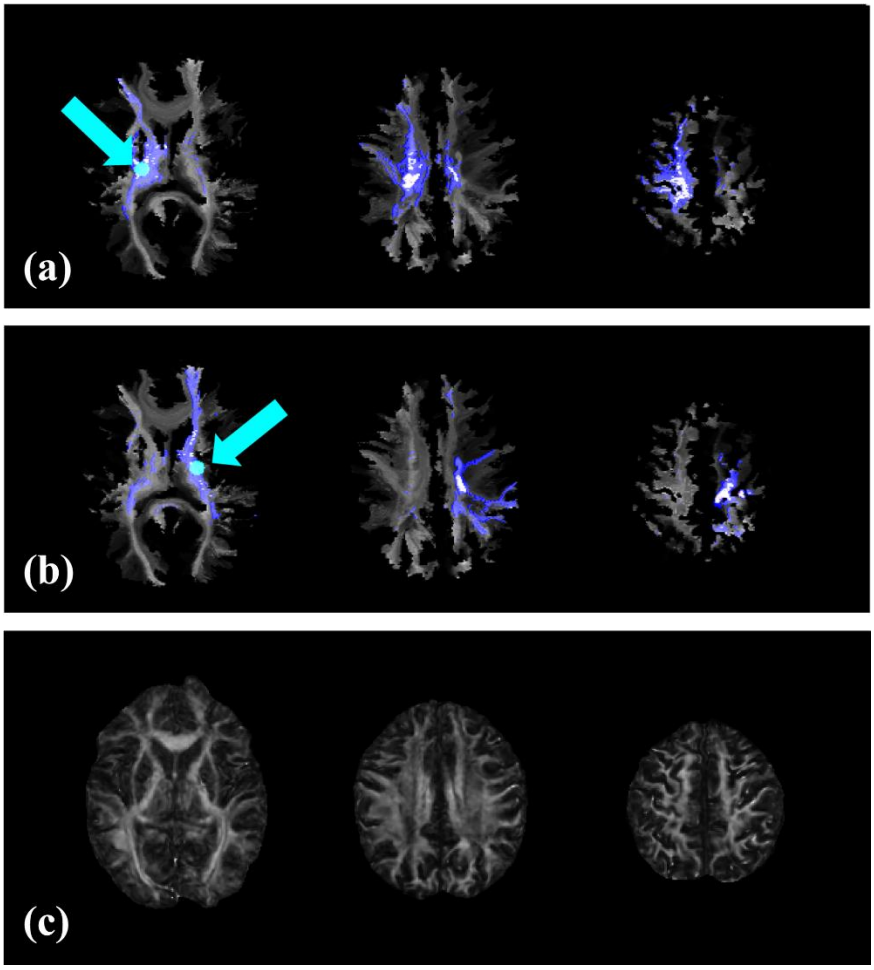

Figure 2-5: Changes in VISC distant from a lesion

Bilateral voxels were selected from the posterior limb of the internal capsule (PLIC) in a chronic stroke subject with a lesion localized to the right anterior limb of the internal capsule (ALIC). Overlaid on lesioned (panel a) and non-lesioned (panel b) sides of the subject's VISC image, the direct neighbors (white) and their direct connections (blue) of each selected voxel (cyan) encompass the sensorimotor area in the most superior slice. Although the fractional anisotropy (panel c) in the cortex of the lesioned hemisphere indicates structural integrity, VISC (panels a and b) is reduced due to the ALIC lesion.

2.3.4 VISC highlighted brain areas distant from the lesion

Voxel-based analyses of VISC, FA and MD were conducted to locate and quantify differences between each stroke survivor and the controls. Each of the three

measures identified differences in specific ipsilesional areas of the brain. The VISC revealed ipsilesional regions with lesion-induced changes in structural connectivity, and these differences were not apparent with MD or FA. Between-group differences (stroke versus control) exclusive to VISC (and not seen with FA or MD) were consistently located outside of the lesion volume (Fig 2-5, 2-6d, 2-7d). The voxels with significantly different MD (Fig 2-6b, 2-7b) were commonly found inside or near the boundary of the lesion volume (Fig 2-6a, 2-7a), and differences in FA (Fig 2-6c, 2-7c) were largely found in the white matter portion of the lesion volume. In all stroke subjects, VISC detected differences within the lesion volume that were revealed by FA and MD. However, VISC exclusively detected additional voxels affected by the lesion that extended along fiber pathways and within the cortical volume superior to the lesion (Fig 2-5). Across all subjects, the number of significantly different voxels between stroke and control groups was always lowest for FA and greatest for MD, with the VISC between the other metrics (Fig 2-8).

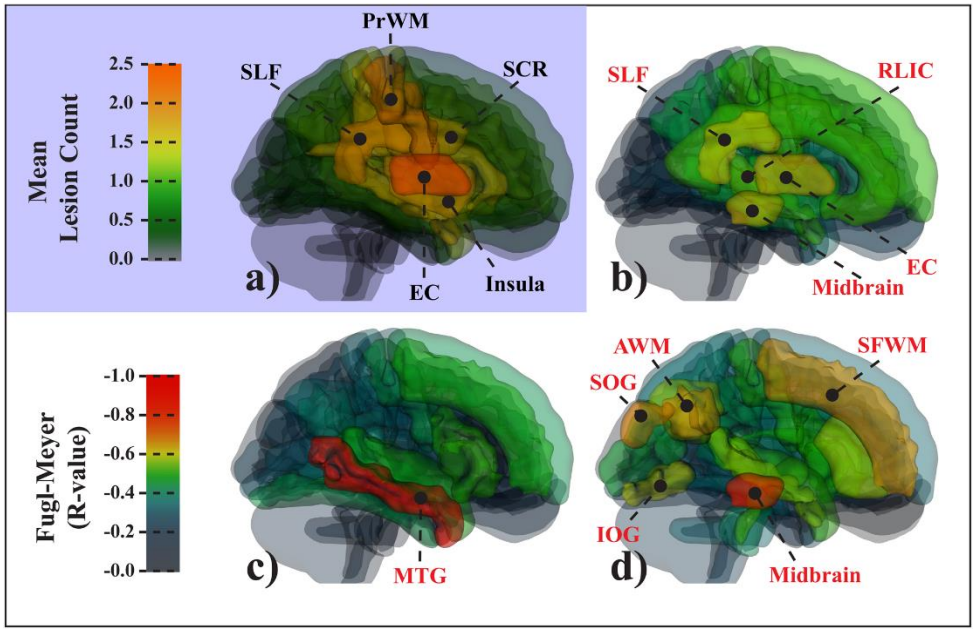

Figure 2-6: Region-based difference volume versus Fugl-Meyer score

Diagram of ipsilesional ROIs in the control template space, showing the lesion distribution and the correlation coefficients of logarithmic difference volume and composite Fugl-Meyer (FM) score. (a) The lesion distribution of the stroke group was most dense in the EC, SLF, PrWM, SCR, and Insula. (b) The MD log difference volume and FM score were not significantly correlated in any ROI. (c) Correlations with total FM score were significant ($p < 0.01$) for FA log difference volume in the middle temporal gyrus. (d) The VISC log difference volume was correlated ($p < 0.01$) with FM score in the midbrain.

Acronyms: angular gyrus white matter (AWM); external capsule (EC); middle temporal gyrus (MTG); precentral gyrus white matter (PrWM); superior corona radiata (SCR); superior frontal gyrus (SFG); superior frontal white matter (SFWM); superior longitudinal fasciculus (SLF); superior temporal gyrus (STG).

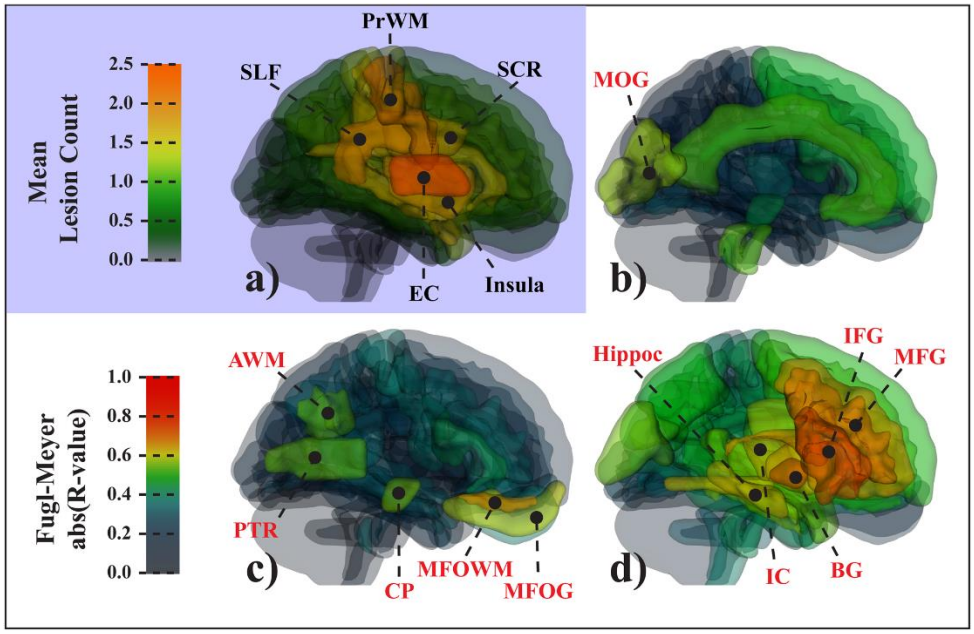

Figure 2-7: Region-based metric means versus Fugl-Meyer score.

Diagram of ipsilesional ROIs in the control template space, showing the lesion distribution and the correlation coefficients of the regional mean versus composite Fugl-Meyer (FM) score. (a) The lesion distribution of the stroke group was most dense in the EC, SLF, PrWM, SCR, and Insula. (b) Correlations between mean MD and total Fugl-Meyer score were significant ($p < 0.05$, corrected) in the MOG. (c) Correlations between mean FA and total Fugl-Meyer score were significant ($p < 0.05$, corrected) in the MFOG, CP, PTR, and AWM. (d) Mean VISC was significantly ($p < 0.05$, corrected) correlated with Fugl-Meyer score in but not limited to the IFG, MFG, IC, BG, and the IFO.

Acronyms: angular gyrus white matter (AWM); basal ganglia (BG); cerebral peduncle (CP); cingulate gyrus (CingG); external capsule (EC); middle occipital gyrus (MOG); middle temporal gyrus (MTG); internal capsule (IC); inferior frontal gyrus (IFG); inferior occipitofrontal fasciculus (IFO); middle frontal gyrus (MFG); middle fronto-oribital gyrus (MFOG); posterior thalamic radiation (PTR); precentral gyrus white matter (PrWM); superior corona radiata (SCR); superior frontal gyrus (SFG); superior longitudinal fasciculus (SLF).

	Fiber Count	Fiber Length	VISC(1.0)
C13	0.131	0.200	0.195
C17	0.174	0.217	0.192
C18	0.176	0.220	0.204
C19	0.134	0.220	0.204
C20	0.075	0.166	0.192
C21	0.175	0.211	0.201
C23	0.120	0.171	0.154
C26	0.139	0.225	0.179
S01	0.168	0.248	0.206
S02	0.208	0.256	0.249
S04	0.125	0.199	0.174
S10	0.143	0.207	0.186
S11	0.166	0.203	0.176
S13	0.150	0.222	0.192
S14	0.154	0.206	0.193
S15	0.142	0.175	0.170
S17	0.026	0.072	0.084
S19	0.118	0.153	0.158
Mean	0.140	0.199	0.184
Stdev	0.041	0.041	0.033

Table 2-3: Subject information.

For each subject, three tractography derived metrics (fiber count, mean fiber length, and VISC) are compared in terms of their correlation (R^2 value) with fractional anisotropy.

2.3.5 VISC metric enhances lesion-related differences

In order to visually compare changes in FA and VISC near the lesion boundary, four isosurfaces were extracted from one stroke subject's FA and VISC images and visualized in 3D (Fig 2-9). FA was sensitive to changes local to the lesion, while VISC reflected changes in regions distant from the lesion. VISC effectively thickened white matter regions that were densely connected to surrounding regions, while thinning those regions less connected to surrounding structures. In Figure 2-9, the FA showed an

asymmetry in the size of the cerebral peduncles, which were not part of the lesion. This asymmetry was enhanced in the VISC image since the paretic cerebral peduncle had a greater decrease in structural connectivity.

2.3.6 Whole-brain VISC correlates with Fugl-Meyer score

The whole-brain log difference volume (LDV) of each metric in the entire brain was regressed with FM score. In comparison with FA and MD, the LDV of VISC had a greater correlation with Fugl-Meyer score. The relationships between Fugl-Meyer score :of the association between difference volume and total Fugl-Meyer score was greater for VISC (R2=0.796, p=0.0005) than for the MD (R2=0.512, p=0.0199) and FA (R2=0.674, p=0.0036).

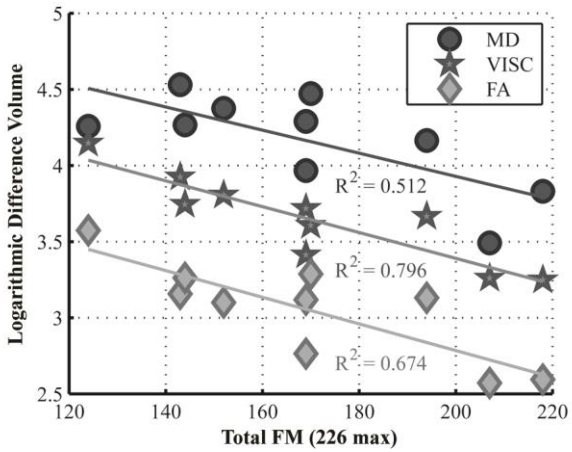

Figure 2-8: Scatterplot of log difference volume versus Fugl-Meyer.

In stroke subjects, the log difference volumes of each DTI metric were correlated with the Fugl-Meyer scores. Log difference volume (LDV) of fractional anisotropy (FA, diamond), mean diffusivity (MD, circle), and voxel-wise indirect structural connectivity (VISC, star) versus Fugl-Meyer (FM) score. The log difference volumes of MD (R^2=0.512), FA (R^2= 0.674), and VISC (R^2=0.796), were significantly correlated with FM score. In each subject, the size of the difference volume was smallest in FA and greatest in MD. The difference volume in VISC was greater than in FA and less than in MD.

In the stroke group, the mean FA and VISC in the ipsilesional hemisphere were regressed against total FM score (Fig 10). Means were first calculated for only voxels with a nonzero VISC, and then again for all voxels. Although the mean FA across ipsilesional voxels with a nonzero VISC was poorly correlated (R2=0.165, p=0.2442) with FM score, the mean VISC in these same voxels was significantly correlated (R2=0.633, p=0.0059) with FM. Across all voxels in the ipsilesional hemisphere, the mean FA had a strong correlation (R2=0.570, p=0.0117) with the behavioral measurements, and mean VISC held its strong correlation (R2=0.676, p=0.0035). The mean MD across voxels with nonzero VISC was moderately correlated (R2=0.304, p=0.0985) with FM, while this correlation was poor (R2=0.194, p=0.2030) for the mean of all ipsilesional voxels.

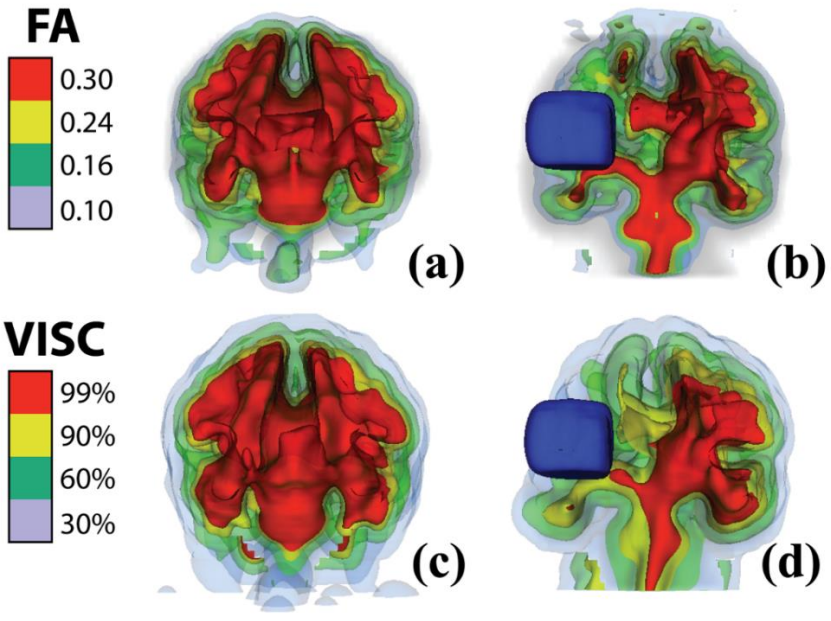

Figure 2-9: 3D isosurfaces of VISC and FA

A visual comparison of FA (top) and VISC (bottom) in a control (left) and a stroke (right). The manually-selected lesion volume is shown with a blue surface.

2.3.7 Association between VISC and Fugl-Meyer Score

The first multiple linear regression analysis tested DTI parameter LDVs as predictors of Fugl-Meyer domain scores. No significant ($p < 0.05$, corrected) associations were detected in this regression. Next, the second multiple regression tested DTI parameter LDV's as predictors of full upper extremity and full lower extremity FM scores. In this case, the LDV of VISC was a significant ($R2=0.821$, $p < 0.05$, corrected) identifier of the upper extremity score. As shown in Figure 11, the upper extremity subscore of the Fugl-Meyer test was strongly associated with LDV for VISC ($R2=0.879$, $p=0.00006$), but the lower extremity subscore was not significantly correlated with LDV ($R2=0.177$, $p=0.226$). Significant correlations ($p < 0.05$, corrected) were found specifically between the log number of significant voxels in VISC and the full upper extremity score (max 130). Two equivalent tests were repeated with the mean DTI parameter across all voxels in the iplesional hemisphere as a predictor of the FM subscores. The mean ipsilesional VISC and FA were both significantly ($p < 0.05$, corrected) correlated with the pain domain score of the Fugl-Meyer. We did not further consider this correlation with pain as a reliable result since eight of the ten stroke subjects scored perfectly (44 out of 44) in the pain domain. No other significant associations were

found in these four tests.

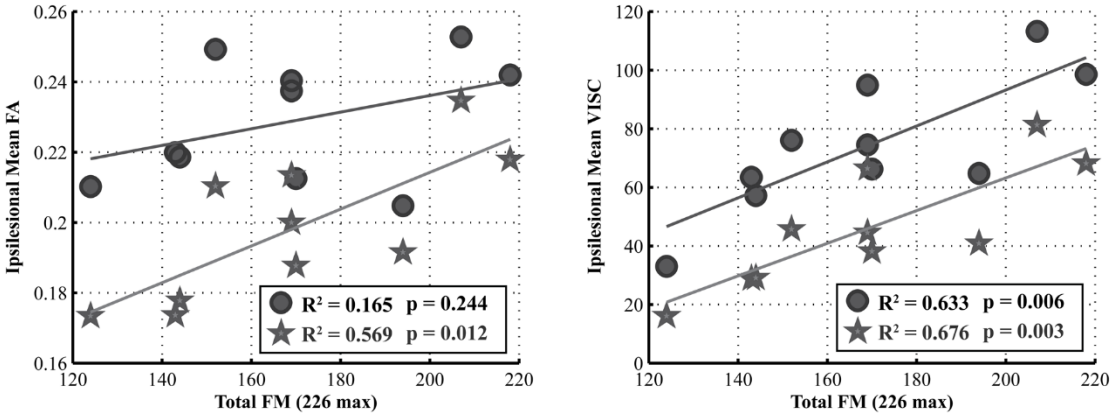

Figure 2-10: Scatter plots of mean FA and VISC versus Fugl-Meyer score.

In the stroke group, the mean FA (left) and VISC (right) in the ipsilesional hemisphere were regressed against total FM score. Means were first calculated for only voxels with a nonzero VISC (star), and then again for all voxels (circle). Although the mean FA across ipsilesional voxels with nonzero VISC was poorly correlated (R^2=0.1649, p=0.2442) with FM score, the mean VISC in these same voxels was significantly correlated (R^2=0.6332 , p=0.0059) with FM. Across all voxels in the ipsilesional hemisphere, the mean FA had a strong correlation (R2=0.5691, p=0.0117) with the behavioral measurements, and mean VISC held its strong correlation (R2=0.6763 , p=0.0035).

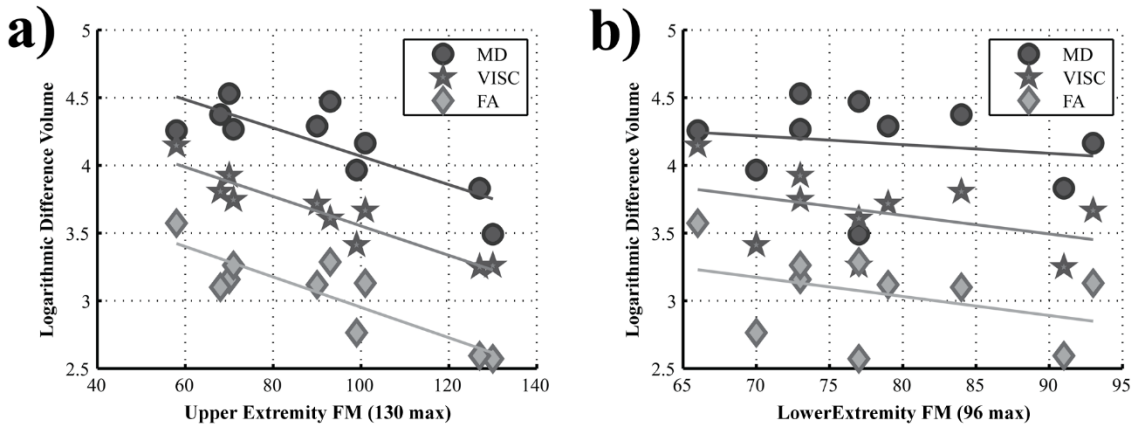

Figure 2-11: Scatter plots of VISC differences versus clinical score.

Scatter plots of the logarithm of significant voxels versus the Fugl-Meyer subscores. (a) The upper extremity FM score was highly correlated with the differences volumes of FA (R^2= 0.7453, $p < 0.01$), MD (R^2= 0.6549, $p < 0.01$), and VISC (R^2= 0.8795, $p < 0.0001$). (b) However, the lower extremity FM score was not correlated with the difference volumes of FA (p = 0.23), MD (p = 0.62), or VISC (p = 0.27).

2.3.8 Post-hoc region-based results

There were significant correlations ($p < 0.05$, corrected) between the logarithmic difference volume and the total FM score with respect to specific ipsilesional ROIs and metrics (Fig 2-6). The correlations were generally strongest with the VISC metric as the predictor in both whole-brain and region-based analyses. The LDV of VISC in the midbrain and association areas (Fig 2-6d) was correlated with total FM. The FM score was also correlated with the LDV of MD (Fig 2-6b) in the midbrain and LDV of FA in the middle temporal gyrus (Fig 2-6c). Table 2-4 lists the levels of significance in the

VISC			MD			FA		
Mdbrain	0.00155	**	EC	0.01746	*	MTG	0.00003	*
SOG	0.01290	*	Mdbrain	0.02202	*	IFG	0.06732	
SFWM	0.01582	*	SLF	0.02359	*	SFWM	0.07459	
AWM	0.01689	*	RLIC	0.04980	*	STG	0.07861	
IOG	0.03041	*	CingG	0.05828		PrCWM	0.11204	
ACR	0.03494	*	PrCWM	0.05860		STWM	0.11483	
AG	0.03515	*	STWM	0.05942		Fu	0.11843	
STWM	0.04184	*	SFG	0.06571		SFG	0.13267	
RLIC	0.04844	*	PoCWM	0.07137		AWM	0.16955	
GP	0.06572		MFWM	0.08297		SCC	0.17872	
STG	0.06706		Ins	0.08956		IOG	0.19262	

Table 2-4: Clinical Correlations with Region-based Mean.

Significance levels of correlations between the ROI mean of each DTI metric and the total Fugl-Meyer (226 maximum).
* indicates the first level of significance (corrected $p < 0.05$). ** indicates the second level of significance (corrected $p < 0.01$).

Acronyms: anterior limb of the internal capsule (ALIC), angular gyrus white matter (AWM), caudate nucleus (Caud), cingulum (CGC), cingulate gyrus (CingG), cerebral peduncle (CP), globus pallidus (GP), hippocampus (Hippo), inferior frontal gyrus (IFG), inferior frontal white matter (IFWM), lateral fronto-orbital white matter (LFOWM), middle frontal gyrus (MFG), middle fronto-orbital gyrus (MFOG), middle fronto-orbital white matter (MFOWM), middle frontal white matter (MFWM), medial lemniscus (ML), middle occipital gyrus (MOG), posterior limb of the internal capsule (PLIC), pons (Pons), precentral gyrus (PrCG), posterior thalamic radiation (PTR), putamen (Put), gyrus rectus (RG), superior frontal gyrus (SFG), superior frontal white matter (SFWM), sagittal stratum (SS)

correlations between the ROI log number of significant voxels and FM score. The mean VISC in the basal ganglia, posterior limb of the internal capsule, and middle and inferior frontal gyri (Fig 2-7d) was strongly correlated with the FM score and its upper extremity subscore. Mean MD was correlated with FM score in the middle occipital gyrus (Fig 2-7b), and mean FA was significantly correlated with FM score in the fronto-orbital gray and white matter, cerebral peduncle, angular white matter, and posterior thalamic radiation (Fig 2-7c). Table 2-5 lists the levels of significance in the correlations between the ROI mean and FM score.

VISC			MD			FA		
IFG	0.00568	**	MOG	0.03746	*	MFOWM	0.01453	*
IFWM	0.00622	**	Pons	0.05387		MFOG	0.02856	*
GP	0.00662	**	CingG	0.05538		CP	0.04144	*
MFWM	0.01019	*	SFG	0.08993		AWM	0.04931	*
MFG	0.01331	*	IFWM	0.10148		PTR	0.04999	*
Caud	0.01511	*	ML	0.10301		IFWM	0.12120	
Put	0.01836	*	CP	0.12125		RG	0.19977	
Hippo	0.02196	*	CGC	0.12518		PrCG	0.20301	
PLIC	0.02262	*	MFOWM	0.13135		LFOWM	0.20901	
SS	0.02323	*	SFWM	0.13771		MFWM	0.22168	
ALIC	0.02412	*	PLIC	0.21877		ML	0.24035	

Table 2-5: Clinical Correlations with Region-based Difference Volume.

Significance levels of correlations between the ROI log number of significant voxels of each DTI metric and the total Fugl-Meyer (226 maximum). * indicates the first level of significance (corrected $p < 0.05$). ** indicates the second level of significance (corrected $p < 0.01$).

Acronyms: anterior corona radiata (ACR), angular gyrus (AG), angular gyrus white matter (AWM), cingulate gyrus (CingG), external capsule (EC), fusiform gyrus (Fu), globus pallidus (GP), inferior frontal gyrus (IFG), insular cortex (Ins), inferior occipital gyrus (IOG), midbrain (mdbrain), middle frontal white matter (MFWM), middle temporal gyrus (MTG), postcentral white matter (PoCWM), precentral white matter (PrCWM), retrolenticular part of the internal capsule (RLIC), splenium of the corpus callosum (SCC), superior frontal gyrus (SFG), superior frontal white matter (SFWM), superior longitudinal fasciculus (SLF), superior occipital gyrus (SOG), superior temporal gyrus (STG), superior temporal white matter (STWM).

2.4 DISCUSSION AND CONCLUSIONS

The results of this study suggest that VISC provides unique information about sensorimotor impairment after stroke. VISC was weakly correlated with FA ($R^2<0.2$) on a voxel-by-voxel basis. Furthermore, the mean VISC and FA across ipsilesional voxels with an FA above 0.15 were correlated with FM score. This suggests that each metric accounts for a different portion of the variance in impaired function in chronic stroke. In both ROI analyses, the VISC metric enhanced a broader set of brain regions. Thus, the VISC metric uniquely identified areas whose structural connectivity may be involved in sensorimotor function after stroke.

Our novel VISC metric differed in chronic stroke survivors compared to controls in brain regions outside the lesion site. Further, the number of voxels with significantly different VISC values correlated with sensorimotor impairment. Although VISC and FA were significantly correlated with Fugl-Meyer, they were weakly correlated with one another. This suggests that VISC and the other DTI metrics each explain a significant amount of variance in motor impairment of chronic stroke subjects. Multiple regression revealed that both the whole-brain log difference volume and ipsilesional mean of VISC provide unique information about upper extremity sensorimotor impairment after stroke. Furthermore, VISC and FA identified different regions with differences between stroke and controls, which suggests that the VISC provides unique information about the effect of a lesion on brain structure. The ipsilesional mean and log number of significant voxels in the VISC metric both had a greater correlation with sensorimotor impairment than the conventional DTI metrics, MD and FA. This observation may indicate that a broader set

of brain areas associated with sensorimotor function can be assessed with the VISC metric as compared to MD and FA. The correlations also seen with MD and FA suggest that local white matter structural diffusion properties near the lesion are associated with higher function. The region-specific correlations exclusive to the VISC metric support that white matter structural connectivity is key to sensorimotor recovery in chronic stroke survivors.

VISC could serve as a unique tool for voxel-wise structural network analysis based on DTI tractography in stroke subjects. Rather than integrating the voxel-wise z-scores of stroke subjects, weighted by a metric derived from region-based structural network analysis (Kuceyeski et al., 2011), or lesion overlap with specific fiber bundles (Riley et al., 2011), the VISC metric is intrinsic and derived directly from DTI tractography. Our conclusion that DTI tractography-based metrics correlate with FM score after stroke is consistent with other studies (Lindenberg et al., 2010; Riley et al., 2011; Zhu et al., 2010).

The VISC metric bears some resemblance to the region-based indirect structural connectivity metric introduced for ROI analysis (Sporns, 2011). This metric is computed for an ROI by summing the product of structural connectivity for all connections through level 2, from all regions, divided by the ROI's number of connections with level 2. In addition to being a voxel-wise metric, VISC is different in that it is the mean number of direct (level 1) connections over only indirect neighbors (level 2). Sporns et al. found that region-based direct structural connectivity has a higher correlation with regional resting-state functional connectivity as compared to regional indirect structural connectivity. We found that at the voxel level, indirect structural connectivity is more

reproducible in the control population than direct structural connectivity. It is possible that since it is a measure of mean connectivity, VISC is more robust to voxel-level misregistrations. We incorporated the α parameter into VISC so that setting α to 0 leads to simply the sum of all direct (level 1) connections to indirect (level 2) neighbors, which is similar to region-based indirect connectivity measures.

Results from the whole-brain analyses revealed the ability of VISC to detect lesion-induced changes in structural connectivity in voxels where FA was not significantly affected. However, the ROI analyses used in this study associated different sets of brain areas with measurements of sensorimotor impairment. Our log difference volume analysis accounted for the mean and variance in the control group at every voxel. This approach identified areas inside of the lesion (as with MD), near lesion boundaries (FA and VISC), and distant integrative association areas (as with VISC). On the other hand, the means of FA and VISC were correlated with FM score in prefrontal areas and the basal ganglia. A change in a regional mean could be caused by a large localized change or a moderate change distributed throughout the region. Due to this uncertainty, the correlations with regional means are difficult to interpret. In combination, the two ROI analyses do not necessarily agree on which regions are associated with sensorimotor impairment after stroke. Inconsistencies between the results of the ROI analyses places limits on the insights gained about the roles of specific brain areas in sensorimotor function after stroke. Whole-brain voxel-based analyses may serve as an objective and more reliable tool for assessing stroke lesions; however, this study was limited by the relatively small number of stroke subjects, and it is possible that the sample size impacted the region-based results.

The voxel-based approach used for the VISC metric in the current study has some advantages over ROI analyses. Voxel-based analysis is not subject to region of interest selection and a priori information. This is important since ROI segmentation may be sensitive to lesion-related changes in structure in stroke survivors. Voxel-wise metrics also provide more sensitive and specific localization of spatial variations, and contrast maps may be visualized in a standardized image space. The VISC metric is also intrinsic and excludes direct neighbors from the average, being based on number of neighbors rather than number of connections. Scheinost et al. introduced a similar intrinsic voxel-wise functional connectivity metric to alleviate the need for a threshold in resting state functional resonance imaging analysis (Scheinost et al., 2012), which produced advantages similar to the voxel-based VISC analysis for DTI data.

Correlations between the upper extremity Fugl-Meyer score and DTI metrics, along with the absence of a correlation between DTI metrics and lower extremity Fugl-Meyer score, could provide insight into the role of white matter structural connectivity in motor impairment. Specifically, correlation analyses between FM subcomponents and VISC volume of significance may suggest that structural connectivity of integrative brain regions may play a larger role in upper extremity motor function than in lower extremity function. The FA of association cortical regions has been previously shown to correlate with upper extremity motor function in stroke subjects with severe impairment. For example, one study found that upper extremity Fugl-Meyer score was correlated with fiber number asymmetry ($R = -0.80$; $p < 0.001$) and regional fractional anisotropy asymmetry ($R = -0.71$; $p < 0.001$) in the corticospinal tract (Lindenberg et al., 2010). Although such past work and this study did not find correlations between DTI measures

and lower extremity Fugl-Meyer scores, other measures of lower extremity function may lead to positive results.

Partial volumes of fiber populations in a voxel will affect the calculation of VISC because the metric is based on a union of direct connections via multiple penetrating fibers. Image resolution likely has some effect on VISC, but we suspect that normalizing VISC based on resolution may be sufficient to preserve its intensity at each point. If every voxel theoretically included only one white matter fiber, then the connectivity would be based solely on indirect connections via fiber end points. In this case, the indirect neighbors to any voxel would reside in gray matter, and the VISC would reduce to their average joint volume of connected fibers. Even at high image resolution, voxels would often contain multiple fibers from the same bundle. VISC would still take advantage of this partial volume effect since different fibers from the same bundle can bifurcate and converge. A high percent of voxels contain multiple fiber bundle populations at current resolution. On the other hand, the VISC calculation is likely affected by the diffusion tensor model, which fails to resolve crossing or kissing white matter fiber bundles. This is a limitation of the current study, and it must be considered in the physiological interpretation of VISC.

Our tractography technique suffers from the limitations introduced in any DTI tractography method. The diffusion tensor model assumes that any voxel is populated by white matter fibers with only one fiber orientation. This assumption is not valid in the majority of voxels. A higher-order tensor model would improve the physiological relevance of VISC. Also, we did not account for crossing white matter fiber bundles in our tractography algorithm. If a higher order tensor model were used, then the indirect

voxel-based connectivity would need to account for voxels with multiple fiber populations.

Tractography methods and their application to stroke subjects have been criticized because they are correlated with fractional anisotropy. For example, fiber density, calculated as the number of reconstructed fibers that intersect a voxel or region, is correlated with FA (Roberts et al., 2005). We also considered the correlation of VISC and FA for different indirect connectivity weighting factors, α. The VISC and FA of voxels with FA above 0.15 were weakly correlated, as shown in Fig 2-4b. As the influence of total connection count on VISC was increased by adjusting α from 1.0 to 0.0, the correlation of VISC with FA increased until α=0.7 and then decreased. This suggests that the number of indirect connections to a voxel and the average brain volume connected to these indirect neighbors may each provide unique information about local FA.

Another criticism of DTI tractography is the issue of performing tractography in brain images that contain lesions. Although DTI metrics of brain structure based on tractography have been formulated (Buch et al., 2012; Riley et al., 2011) many investigators have avoided performing tractography in the stroke population due to complex changes in diffusion anisotropy associated with the lesion (Budde and Frank, 2010). As an alternative to performing tractography in stroke subjects, (Buch et al., 2012) calculated tractography-based voxel-wise statistics and local structural network measures for a control group within a spatially normalized image space, and then each stroke subject's lesion was warped into the standardized space to localize abnormal anatomy. Our results suggest that a voxel-wise metric based on DTI tractography is

useful for predicting sensorimotor impairment in stroke subjects. Thus, while tractography-based metrics must be interpreted with caution, they may have value is assessing the implications of a brain lesion.

Key limitations of this study include concerns with the image registration technique, multiple comparisons correction in voxel-wise analysis, and manual lesion selection. Diffeomorphic registration algorithms have been used previously for aligning diffusion tensor images (Beg et al., 2005). An advantage of diffeomorphic registration is that the transform is guaranteed to have a smooth inverse. Thus, applying a forward transform followed by its inverse leads to negligible error. In this study, a noninvertible registration algorithm was used to align the anatomical MR images. An inverse transform was approximated with an error distribution of 0.5622 ± 0.3326 mm. This error could have increased both false positive and false negative voxel-wise t-tests. Diffeomorphic registration is also superior to other techniques in preserving anatomical topology (Beg et al., 2005). We chose a method with less assumptions of topology since stroke lesions may alter the topology of the anatomy. Note that this likely led to higher registration errors in voxels distant from the lesion. Nonetheless, our analysis accounted for the distribution in error due to misregistration at each voxel because the same registration method in this study was used in the control group.

Another minor concern with this study was that the voxel-wise analysis did not account for misregistration errors. Concerns have been raised with voxel-based approaches when used for group comparison because of image misregistration (Bookstein, 2001). There are a number of studies that have addressed registration in voxel-based approaches. Voxel-based morphometry (Ashburner and Friston, 2000) is an

attractive technique in that it allows for objective full-brain analysis between populations. This technique reduces effects of registration errors by performing of spatial smoothing prior to voxel-wise Student's T-tests, and then corrects for multiple comparisons by determining significant clusters of spatially connected voxels. Tract-based spatial statistics (TBSS) (Smith et al., 2006) attenuates the effects of misregistration on voxel-based analysis without spatial smoothing. TBSS skeletonizes the mean FA across spatially normalized subjects, and then uses the FA from a voxel near the skeleton in each subject. The VISC metric of the current study may have been less sensitive to misregistration errors because it based on a mean of fiber volumes that, together, represent global white matter structural connectivity of the brain. Being based on the union of multiple fiber pathways, VISC may also be robust against degenerate fibers that contaminate metrics based on fiber counts or mean fiber length. Although VISC can intrinsically detect changes in global white matter structural connectivity at the voxel level, differences in VISC between neighboring voxels should still be interpreted with caution.

This study's third limitation was the manual delineation of the lesion volume. Initially, registering each stroke subject to a control without any correction resulted in distorted morphology near the lesion boundary. Thus, we manually selected a 3D lesion ROI from the structural MR image and then masked the lesion during registration. Few methods have been proposed for automatically segmenting stroke lesions from an anatomical MR image. One technique automatically calculates a lesion mask by thresholding the displacement of the uncorrected deformation map, and then performs registration with lesion masking (Buch et al., 2012). We decided not to use such an

approach since some lesions were too small to be detected by the displacement mapping but still led to misregistration near the lesion boundary. Another study optimized local correlations between T1-weighted images in order to register abnormal anatomy with controls (Avants et al., 2008). Although this approach may have provided more consistent registration in stroke subjects, we feel that our method, which accounted for lesion information, was sufficient for the statistical analyses in this study. Overall, we believe that the errors associated with manual selection were minor compared to the advantages it provided in registration.

Voxel-based analyses of structural connectivity in the stroke population can be used to objectively identify brain areas involved in sensorimotor function and may be a useful tool for understanding impairments. The voxel-wise indirect structural connectivity (VISC) measure opens opportunities to investigate the impact of a stroke lesion on extralesional anatomical connectivity. VISC and conventional DTI measures each explain a significant amount of variance in upper extremity motor impairment after stroke. Future investigations will validate VISC with analyses that are based on artificial lesions in healthy control subjects. The sensitivity of VISC to image resolution must also be investigated. Although VISC was not predictive of lower extremity Fugl-Meyer scores, it may associate with other measures of lower extremity function. In order to confirm that this method may be used across a spectrum of lesion sizes and locations, this technique should be performed in a larger sample of stroke subjects. Future studies investigating the percent damage or change in mean value of ROIs should interpret the results with caution in that these widely-used approaches may lead to strikingly different results. Increasing the subject sample size may reduce these inconsistencies. We

conclude that our novel VISC metric based on DTI tractography can provide unique information about upper extremity sensorimotor impairment in chronic stroke.

2.5 ACKNOWLEDGEMENTS

The contents of this manuscript were developed under a grant from the Department of Education, NIDRR grant number H133E100007. However, the contents do not necessarily represent the policy of the Department of Education, and you should not assume endorsement by the Federal Government. This study was also conducted with support from the Ralph and Marion C. Falk Medical Research Trust.

2.6 APPENDIX – Voxel-wise Indirect Structural Connectivity Derivation

In this study, we defined a voxel by the position of its center rather than its vertices. In the Digital Imaging and Communications in Medicine (DICOM) standard, the Image Position (Patient) header element with tag (0020,0032) defines the x, y, z coordinates of both the upper left hand corner of the image and the center of the first voxel. Since the DICOM standard defines a voxel by its center in the patient coordinate system, we elected to use this convention in our software and nomenclature.

As a foundation for deriving a voxel-wise connectivity metric, the reconstructed fiber trajectories were expressed as sets of coordinates in the template control subject's DTI image-space with the following mathematical formulation. An image here has n_z slices, each with n_y rows and n_x columns, giving a total of N voxels.

Let each reconstructed fiber be represented as a matrix, $\mathbf{F}$, of 3D fiber trajectory coordinates, where

$$\mathbf{F} = \begin{bmatrix} f_{1,x} & f_{2,x} & \cdots & f_{M-1,x} & f_{M,x} \\ f_{1,y} & f_{2,y} & \cdots & f_{M-1,y} & f_{M,y} \\ f_{1,z} & f_{2,z} & \cdots & f_{M-1,z} & f_{M,z} \end{bmatrix} \quad f_{j,d} \in \mathbb{R} \qquad \text{(Eq. A1)}$$

M is the number of points in the reconstructed fiber and $f_{j,d}$ is the *d*th dimension continuous coordinate of the *j*th point along the trajectory. Using nearest neighbor interpolation, the 3D continuous coordinates from $\mathbf{F}$ are converted into 1D voxel indices. Let these indices be represented in vector $\tilde{\mathrm{f}}$, with

$$\tilde{f}_j = \left\lfloor f_{j,x} + 0.5 \right\rfloor + n_x \left\lfloor f_{j,y} + 0.5 \right\rfloor + n_x n_y \left\lfloor f_{j,z} + 0.5 \right\rfloor. \quad j \in \left[1, 2, \ldots, M-1, M\right]$$

Next, we represent the set of voxels penetrated by fiber $\mathbf{F}$ as an inclusion mask over the entire image. Let vector p of length *N* (# of voxels) be the voxel-wise inclusion mask of *one* fiber, where

$$p_i = \begin{cases} 1 & \exists j : \tilde{f}_j = i \\ 0 & \text{otherwise.} \end{cases} \qquad \text{(Eq. A2)}$$

If $p_i = 1$, this indicates that fiber $\mathbf{F}$ penetrates the *i*th voxel. Note that all voxels included in p are described here as being structurally connected. An $N \times N$ connectivity matrix, $\tilde{\mathbf{X}}$, is used to represent the direct connections between the voxels masked by p with

$$\tilde{\mathbf{X}} = \left(\mathbf{p}^T \mathbf{p}\right) - \mathrm{diag}(\mathbf{p}). \qquad \text{(Eq. A3)}$$

Note that

$$\mathrm{diag}(\mathbf{p}) = \begin{bmatrix} p_1 & & 0 \\ & \ddots & \\ 0 & & p_N \end{bmatrix}.$$

If $\tilde{\mathbf{X}}_k$ is the connectivity matrix for the k^{th} fiber, then let $\mathbf{X}$ be the union of connectivity matrices across all Q fibers, where

$$\mathbf{X} = \bigcup_{k=1}^{Q} \tilde{\mathbf{X}}_k \quad . \qquad \text{(Eq. A4)}$$

If x_{ij} , an element of $\mathbf{X}$, is 1, then the i^{th} and j^{th} voxels are penetrated by least one common fiber. Thus, $\mathbf{X}$ is a voxel-wise direct connectivity matrix. Next, if the i^{th} and j^{th} voxels share at least one common direct neighbor but are not directly connected by a fiber, then we define them as indirect neighbors. Let matrix $\mathbf{Y}$ be the voxel-wise indirect structural connectivity (VISC) matrix, where

$$y_{ij} = \begin{cases} (1 - x_{ij})\left(1 - \prod_{k=1}^{N}(1 - x_{ik}x_{kj})\right) & i \neq j \\ 0 & \text{otherwise.} \end{cases} \qquad \text{(Eq. A5)}$$

Note that term $(1 - x_{ij})$ excludes voxels that are direct neighbors, and term $\left(1 - \prod_{k=1}^{N}(1 - x_{ik}x_{kj})\right)$ includes pairs of voxels that *share* at least one direct neighbor. Finally, the VISC index for the i^{th} voxel is

$$\mathrm{VISC}_i = \frac{\mathbf{y}_{(i)}\mathbf{X}\mathbf{1}}{\mathbf{y}_{(i)}\mathbf{1}} = \frac{\sum_{j}^{N}\left(y_{ij}\sum_{k}^{N}x_{jk}\right)}{\sum_{j}^{N}y_{ij}} \qquad \text{(Eq. 1)}$$

Where $\mathbf{1}$ is the summation vector of length *N* and $\mathbf{y}_{(i)}$ is the *i*th row vector from matrix $\mathbf{Y}$.

Note that the denominator of VISC is the total number of voxels indirectly connected to the *i*th voxel, whereas the numerator is the summation of direct connections to these same voxels. The nested summation in the numerator of Eq. (1) is over x_{jk}, which gives the total number of *direct* connections to the *j*th voxel. The y_{ij} terms are inclusive to only *indirect* connections to the *i*th voxel.

Previously introduced voxel-wise metrics based on DTI tractography, such as fiber count and mean fiber length (Roberts et al., 2005), are correlated with FA. In order to consider whether fiber count information affected the correlation of VISC with FA, we incorporated a connection count weighting factor α. This contrast mechanism gives weight to the total number of connections to a voxel through structural connectivity level 2 (Sporns, 2011) neighbors. As α is decreased from 1 to 0, the VISC approximates the *total number* rather than the *mean number* of direct connections to a voxel's indirect neighbors, with VISC parameterized by α as

$$\mathrm{VISC}(\alpha)_i = \frac{\mathbf{y}_{(i)}\mathbf{X}\mathbf{1}}{(\mathbf{y}_{(i)}\mathbf{1})^{\alpha}}. \qquad \text{(Eq. 2)}$$

CHAPTER 3: CEREBELLAR FUNCTIONAL CONNECTIVITY IN MULTISENSORY INTEGRATION DURING MOVEMENT AFTER STROKE

3.1 INTRODUCTION

Brain areas known for integrating multiple forms of information may be a central hub of communication that allows humans to process sensory information during movement. The primary sensory areas pass information to unimodal association areas, which then converge in multimodal sensory integration areas. The posterior association area is located in the intraparietal sulcus, while the anterior association area is located in the prefrontal cortex. Communication between the premotor cortex and posterior parietal cortex has been shown to be critical in fine motor skill (Buch et al., 2012). Structural and functional human brain mapping based on magnetic resonance imaging contrasts can be used to measure these interactions. Diffusion MRI tractography is a technique that allows mapping axonal pathways that connect brain areas at the macroscopic level. Functional MRI (fMRI) measures a signal that is sensitive to the level of blood oxygenation in the brain, known as the blood-oxygen level dependent (BOLD) signal.

Although current measures of structural and functional connectivity can characterize the nature of communication between the network hubs and other brain areas, the role of the association areas has not been explored in a paradigm of multimodal sensory integration during fine movement. In order to understand the interaction between movement and sensory integration, functional connectivity must be measured during sensorimotor integration with and without movement.

In this study, we developed an experimental paradigm that invokes sensory integration pathways during movement. Additionally, we developed a novel metric

based on functional and structural brain connectivity that may serve as a potential future biomarker in stroke patients.

The purpose of this study was to characterize differences in multimodal sensory integration circuits in stroke survivors with motor impairment. In a number of prior studies, attention has focused on the functional effects of stroke lesions in the primary motor pathways (Cheng et al., 2012; Sharma et al., 2009; Wang et al., 2010; Ward et al., 2003). However, brain lesions might have even stronger impact on integrative networks that process multisensory inputs and plan movements in a functional context. These networks are widespread, making it more likely that they will be affected by a stroke at a number of possible locations. Lesions affecting sensorimotor integrative networks of the brain may play a critical role in recovery and further, damage to these networks could lead to chronic impairment as they are important to motor learning and recovery (Bosnell et al., 2011; Buch et al., 2012; Evans, 2013; Lotze et al., 2012; Murphy and Corbett, 2009; Sharma et al., 2009; Ward et al., 2003). In order to characterize the function of sensorimotor networks in stroke survivors, we measured brain connectivity with functional magnetic resonance imaging (fMRI) using a task that invoked key features of sensorimotor and multisensory integration.

fMRI has been used to characterize differences in brain activation patterns in stroke survivors and to document cortical plasticity with recovery or following therapeutic interventions. Ward et al. looked at correlations of task-based fMRI with sensorimotor function in stroke subjects with an intact primary motor cortex. They found that the intensity of brain activation within the motor system decreased over multiple sessions in lower functioning stroke survivors, and that these changes correlated with

recovery (Ward et al., 2003). Hypoactive cortical areas have also been documented during continuous pedaling during fMRI (Promjunyakul et al., 2015). During finger movement, stroke survivors have increased cortical activation with a broader spatial extent in the ipsilesional hemisphere as well as contralesional activity absent in controls (Rehme et al., 2011). The level of perilesional hyperactivation has been correlated with lower function. Increases in cortical activity distant from a stroke lesion are seen as evidence for cortical reorganization (Grefkes and Fink, 2011). These plastic changes may be compensatory or potentially maladaptive for functional recovery. To date, these changes have been documented primarily in activation patterns. The emergence of brain functional connectivity analyses (Biswal et al., 1995; van den Heuvel and Hulshoff Pol, 2010) raises the question of whether changes in brain function can be better documented using this approach.

Functional connectivity analyses offer potential insight into changes in brain networks after stroke. Functional connectivity MRI (fcMRI) (Biswal et al., 1995; Friston, 1994) infers coactivation of one or more cortical areas by their correlated fMRI signal over time. This analysis can then be used to identify functional networks using fMRI signals obtained at rest (Biswal et al., 1995) or during a task (Friston, 1994). In resting-state fMRI studies, the most consistent finding has been decreased functional connectivity between the ipsilesional and contralesional sensorimotor cortices (Rehme and Grefkes, 2013). The network topology in stroke subjects has been found to be nonoptimal, with a decrease in network efficiency (Cheng et al., 2012). For this analysis, nodes are defined by predetermined anatomical regions of interest or by measuring regional homogeneity of voxel-wise intrinsic functional connectivity (Yeo et al., 2011).

Edge strength is defined by the temporal correlation between the nodes. In addition, both resting-state and task-based functional connectivity can be decomposed into a set of spatiotemporal networks using an independent component analysis (Beckmann and Smith, 2004; Minka, 2000). Each independent component consists of a 3D volume that provides each voxel's contribution to the network, and a BOLD time-course that is shared by all voxels within that network. Changes in functional MRI networks have been seen in both spatial extent of nodes and in the strength of edges measured in time in diseases such as dementia (Li et al., 2012; Rytty et al., 2013).

Functional connectivity analysis might be particularly effective in quantifying functionally relevant changes in brain networks after stroke and during recovery. Large-scale cortical networks may be critical for functional recovery after stroke (Grefkes and Fink, 2014). Each cortical region may actively participate in multiple functional networks, allowing the brain to reorganize after damage to a particular node (Ward, 2005). Plasticity has been observed in the motor network in stroke (Jiang et al., 2013). The integrity of contralesional parietofrontal (Buch et al., 2012) and sensorimotor cortical networks has been associated with less motor impairment after stroke. These findings suggest that connectivity of sensorimotor integration areas may provide explanations for impairments and plasticity of these networks would provide mechanisms for restoring motor function.

In order to identify changes in sensorimotor networks in chronic stroke survivors, we calculated the functional connectivity of the brain using task-based MRI, with a unique sensorimotor task. The task was specifically designed engage integrative sensorimotor networks. We then compared the changes in these networks to a clinical

measure of upper limb function. We hypothesized that functional connectivity between brain nodes associated with sensorimotor integration would be reduced in stroke survivors, and that the reduction would be correlated to function.

3.2 METHODS

3.2.1 Data Collection

3.2.1.1 Subject Recruitment and Clinical Testing

Twelve young adults (4 female, 25.2 ± 2.4 years), ten individuals with chronic post-stroke hemiparesis (4 female, age 66.7 ± 7.94 years, at least 1.1 years since stroke), and nine age-matched control subjects (5 female, age 64.2 ± 7.73 years) participated in this study. Each subject provided informed written consent to the experimental protocol, which was approved by the Institutional Review Boards at Marquette University and the Medical College of Wisconsin. Inclusion criteria included a history of an ischemic cortical or subcortical stroke that occurred no less than 6 months prior to recruitment. Subjects with no ability to perform supination, pronation, ulnar deviation, or radial deviation of the wrist were excluded. Control subjects without history of stroke or other neurological impairments were age-matched (within 3 years) and gendered-matched to the stroke subjects. Each stroke subject completed the upper extremity (UE) portion of the Fugl-Meyer Assessment (Fugl-Meyer, 1975) for a maximum possible score is 126. Subjects also completed the Box and Blocks Test of Manual Dexterity (Mathiowetz et al., 1985), the Wolf Motor Function Test (Wolf et al., 2001) for upper extremity motor

ability (maximum score of 75), and the Modified Ashworth Scale (Bohannon and Smith, 1987).

3.2.1.3 Experimental Paradigm

Our sensorimotor integration experiment was designed with cues and feedback that contrast the effects of auditory and visual sensation. We introduce a task paradigm for studying the role of sensory integration in complex movement. Chronic stroke subjects have more difficulty coordinating sensorimotor behavior, especially in tasks with higher complexity (Hollands et al. 2012). Our task requires the subject to produce movement while integrating multiple sensory modalities.

Motion recording and audiovisual feedback: Every subject completed two sessions on separate days no more than two weeks apart. The subject was trained to perform a wrist-movement task during the first session, and the second session consisted of a task-based fMRI session using the same wrist movement task. The experimental apparatus is shown in Figure 3-1a. The forearm of the impaired limb was fixed on a small ramp to allow for radial and ulnar deviation of the wrist. The hand gripped the end of a ShapeTape device (Measurand Inc., Canada), an array of sixteen optical fiber sensor pairs that provide 3D Euclidean coordinates along the sensor region. Visual feedback was presented on a computer monitor, and speakers provided auditory feedback. Motion data were recorded every 24 milliseconds, or 41.67 Hz.

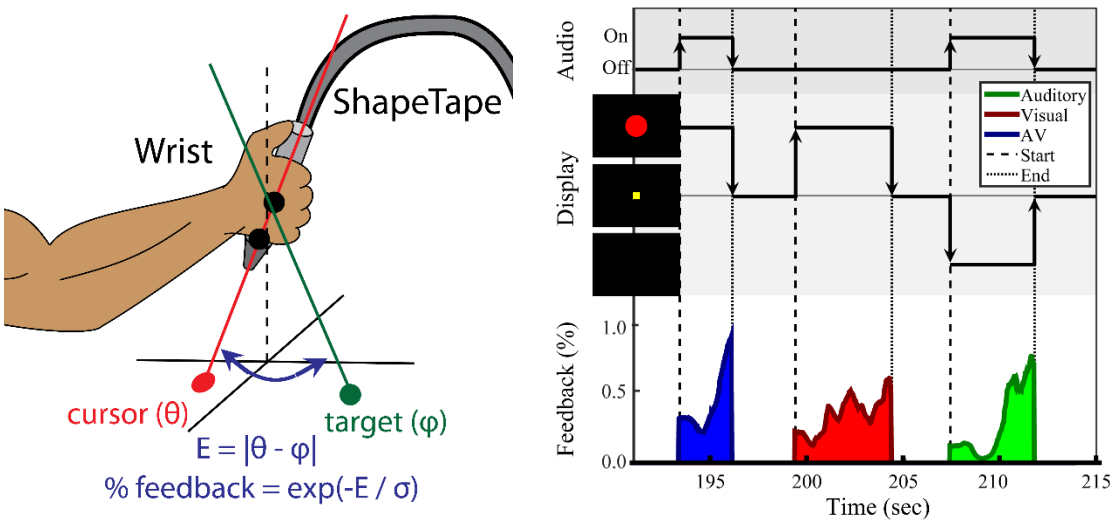

Figure 3-1: Task paradigm for wrist movement and sensorimotor integration.

(Left) Illustration of the ShapeTape apparatus. The forearm position is fixed.
(Right) Experimental design of the multisensory search task. During each trial, the subject maximizes sensory feedback using wrist joint angles to minimize error to a target angle. The subject was instructed to move the wrist to maximize the circle diameter and/or a sound volume. Auditory, visual, or audiovisual feedback were presented at the start and during each trial. After reaching the target, the subject fixated on a yellow square during a 2-4 second intertrial period. The average trial duration was 5 seconds.

Shown in Figure 3-1a, two sensor pairs at the end of the ShapeTape were used to calculate a 3D ray with angle $\boldsymbol{\theta} = \{\theta_x, \theta_z\}$ relative to the horizontal (x-z) plane, which was used to define the orientation of the wrist. Effectively, pronation/supination was mapped to the angle within the x-y plane θ_z, and radial and ulnar deviation was mapped to the angle θ_x in the z-y plane. Letting $\mathbf{p}_n$ and $\mathbf{p}_{n-1}$ be the 3D coordinates of the last two sensors, an orientation vector $\boldsymbol{v}$ was calculated as

$$\boldsymbol{v} = \frac{\mathbf{p}_n - \mathbf{p}_{n-1}}{\|\mathbf{p}_n - \mathbf{p}_{n-1}\|} \qquad \text{Eq. 1}$$

The wrist orientation was estimated as $\theta_x = \tan^{-1}(\mathrm{v}_X/\mathrm{v}_Y)$, and $\theta_Z = \tan^{-1}(\mathrm{v}_Z/\mathrm{v}_Y)$. For each search task, a target angle, $\boldsymbol{\varphi}$, was created. The error to $\boldsymbol{\varphi}$ during the search task was calculated as $E = \sqrt{(\theta_X - \varphi_X)^2 + (\theta_Z - \varphi_Z)^2}$. E was then used to provide feedback to the subject related to wrist proximity to the target. The feedback intensity, w, was calculated as $w = \exp(-E/\sigma)$, with the sensitivity parameter σ fixed at 0.1 radians for all trials. Intensity w was used to modulate visual and auditory feedback stimuli. Auditory feedback was a 440 Hz tone and its volume was modulated linearly by w. Visual feedback was presented as a solid red circle at the center of a black screen. The circle diameter was modulated linearly by w from 15 to 160 pixels or 0.38 – 4.06 cm. The screen was placed approximately 2 feet away from the eyes. The resulting aperture angle was effectively varied between 0.179 – 1.91 degrees.

Experimental design: As shown in Figure 3-1b, a search-based wrist movement task was designed to invoke brain networks involved in sensorimotor and multisensory integration. The first session began with up to five familiarization trials, in which the subject used the wrist to move a white cursor to a yellow square target at the center of the screen. These trials were also used to verify the subject's range of motion. Once comfortable reaching the square, the subject was then informed that the square and cursor would not be visible. At the start of each trial, one of three types of sensory feedback were presented. For both the training session and the fMRI session, a series of two search-task runs (6 minutes each) and one sensory-motor only run (6 minutes) were conducted.

The search-task run consisted of a series of trials, each trial including visual, auditory, or combined audiovisual feedback. In the visual-only feedback condition, a solid red circle appeared and grew larger as error decreased. Once the subject reached the target, the solid red circle was changed into an outline and then disappeared. During auditory-only trials, the subject searched for the target with feedback provided by the tone volume. Upon the subject reaching the target, the tone was altered to a fixed pitch of 880 Hz, giving a "beep" sound, and turned off. In audiovisual feedback trials, the red circle and auditory tone were mapped independently to the x-coordinate and y-coordinate errors. The goal was to maximize both feedback intensities. After the target was reached, the subject fixated at a yellow square at the center of the screen for an intertrial period with a normal random duration of **2.5 ± 0.5** seconds. Subjects were notified that the trial would end automatically after an unspecified time if they failed to reach the target. A maximum duration of 15 seconds was used for all experiments.

A control task involving isolated sensory and motor tasks was conducted after the two search-based task runs. In the motor task, the words "Keep Moving" appeared on the screen, and the subject was told to move the wrist randomly in a similar pattern as during the search task. The subject was instructed to stop moving once the words disappear. The message "Relax" was displayed on the screen for two seconds prior to the sensory only trails. For this condition, the subject was warned that there would be times during which the red circle and sound would appear and change outside of the subject's control. The subject was trained to not move and just watch and listen. The last instruction to the subject was "If you see the words "Keep moving" then move. If you do not see the words "Keep moving", then stay still no matter what happens." Throughout this final run,

the experiment would alternate between motor-only and sensory-only conditions every **12 ± 2.0 seconds.**

3.2.1.4. MRI Scans

Every subject was screened for MRI safety before entering the magnetic environment. An axial T1-weighted anatomical image was acquired using a fast spoiled gradient recalled (SPGR) pulse sequence, with TE: 3.2 ms, TR: 8.16 ms, flip angle: 12 deg, prep time: 450, bandwidth: 22.73, FOV: 240 mm, 156 1mm slices, matrix size: 256x240. Next, an axial q-ball high angular resolution diffusion imaging sequence was acquired with a single-shot echo planar imaging sequence, including 5 b=0 images, 150 diffusion-weighted directions, SENSE parallel imaging, TE: 72.3 ms, TR: 5700 ms, FOV: 250 mm, matrix size: 128x128 resampled to a 256x256 grid (2mm pixel width/height), 57 2.5 mm slices. For functional MRI, a sagittal view gradient-echo echo-planar sequence was acquired with TE: 25 ms, TR: 2000ms, flip angle: 77 deg, FOV: 240mm x 240mm, 41 slices with 35 mm thickness.

3.2.1.5. MRI experimental setup:

As the subject lay supine, the forearm was elevated with foam and fixed in place with sandbags. The ShapeTape was placed into the subject's impaired hand, or right hand in healthy adults. Visual feedback was projected to a visor attached to the head coil, and earbuds were placed into the ears to provide auditory feedback. The MRI scan session consisted of one resting-state run followed by three task-based runs. During the

6-minute resting-state run, each subject was asked to close their eyes and stay alert. After the resting-state scan, the ShapeTape was placed into the subject's hand. If the subject had difficulty gripping the device, then a surgical wrap was used to keep the hand closed. The subject completed three 6-minute runs of the same experiment conducted for the first session, including two search-based and one sensory-motor only.

3.2.2 Image registration and lesion side normalization

Intersubject and intermodality image registration was completed in both healthy adults and stroke subjects using fully automated techniques. Each subject's anatomical T1-weighted MRI volume was registered to a 152-brain MNI space using a 12-parameter affine registration, and then nonlinear image registration was performed using Maxwell's demons algorithm (Thirion, 1998). Local histogram matching was performed prior to deformable image registration in order to mitigate errors caused by lesion contrasts. The images of all stroke subjects that completed the experiment with the left arm were flipped over the sagittal plane so that all lesions were on the left side of MNI space. One of these subjects had a lesion within the left cerebellum. The flipping placed all strokes outside the cerebellum on the left side of MNI space.

3.2.3 fMRI data processing

3.2.3.1. General linear model for the search task

Task-based functional MRI analysis was performed with Analysis of Functional Neurological Images (AFNI, afni.nimh.nih.gov/afni). Data were temporally resampled in order to correct for nonuniform slice acquisition timing within each volume. BOLD signal changes related to head translation and rotation were corrected by affine coregistration between volumes using AFNI's 3dvolreg function. The data were high-pass filtered above 0.01 Hz. The motion parameters included roll, yaw, pitch, and x, y, z translations, and were treated as coregressors for all subsequent analyses.

3.2.3.2. General linear model and cortical activation maps

We were interested in stroke-related differences in cortical activity involved in sensorimotor integration during movement. As previously shown in Figure 3-1, at the start of the trial the sensory feedback is at its lowest while. On the contrary, the level of wrist motion (not displayed in the figure) is greatest at the start of the search. As the subject closes in on the target, sensory feedback increases. In this latter phase of the task, finer wrist movements must be made. Thus, wrist movement is greatest at the start of each trial, and sensory feedback is greatest at the end. In order to identify the brain activity associated with movement, wrist motion was estimated as the absolute change in $\boldsymbol{\theta}$ with time.

The sensory feedback and wrist movement signals, both produced with our in-house software from the ShapeTape data, were median filtered with a window of 2

seconds. Using the "waver" function in AFNI, the signals were then convolved with a double-gamma variate hemodynamic response function to produce modeled BOLD responses and resampled to the fMRI temporal resolution of 0.5 Hz. This method was repeated for the auditory, visual, and audiovisual feedback conditions to produce three movement regressors (A_M, V_M, AV_M) and three sensory feedback regressors (A_S, V_S, AV_S). Using the 3dDeconvolve program in AFNI, a multilinear regression was performed for each voxel, with the six task-related regressors and six head motion parameters (three rotation, three translation) contributing to the BOLD signal. The marginal t-value for the beta coefficient of each task-related movement regressor (e.g. A_M, V_M, AV_M) was resampled into 1mm MNI space. These three cortical activation maps were calculated for every stroke subject and age-matched control.

3.2.3.3. Functional network maps

Functional connectivity MRI analysis was performed with Multivariate Exploratory Linear Decomposition into Independent Components (MELODIC) Version 3.14 available with the FMRIB's Software Library (FSL, www.fmrib.ox.ac.uk/fsl). All runs and subjects were time concatenated for a single 75-run (19 subjects and 4 runs) group ICA. The sensory-motor only task run of subject S04 was not included in the analysis since data collection was not complete. The data were high-pass filtered with a cutoff frequency of 0.01 Hz (Marchini and Ripley, 2000). The first five TRs were discarded to exclude signal drifts due to system ramp-up. This left each run with 175 volumes over 350 seconds. The functional image volumes were motion corrected using the MCFLIRT implementation (Jenkinson et al., 2002). Slice-time correction was

applied using linear interpolation. Skull-stripping was automatically performed with the brain extraction tool (BET) (Smith, 2002), and the data were spatially smoothed with a 5 mm full-width half-max Gaussian kernel. The resulting brain mask was used to exclude non-brain voxels from the remaining analysis. All subjects were spatially normalized to an anatomical MNI standard template using a 12-parameter affine registration implemented in FLIRT (Jenkinson and Smith, 2001). The voxel BOLD times series were demeaned, variance normalized, and whitened.

The number of independent components was estimated using a Bayesian approach described by Minka *et* al. in (Minka, 2000). Using Probabilistic Independent Component Analysis (Beckmann and Smith, 2004), the whitened time data were projected onto a 53-dimension subspace. Fixed-point iteration optimization (Hyvarinen, 1999) was used to decompose the projected data into independent vector sets that account for variability in temporal, spatial, and subject domains. The spatial components were normalized by the variance of the residuals, and a mixture model was fit to their intensity histograms to determine a statistical threshold (Beckmann and Smith, 2004).

Once the independent components for the group were calculated, a dual regression (Beckmann et al., 2009) was used to estimate individual spatial maps and time courses for each subject and session. Components with vertical stripes in the axial view were associated with motion and excluded from further analysis. Voxel-based t-tests were performed between stroke and age-matched controls for each independent component.

3.2.3.4. Task-based network identification

Overall relationships between resting-state networks and the task conditions were estimated with temporal correlation. The BOLD response to each task condition was modeled by convolving the stimulus presentation time signal with a double-gamma hemodynamic response function. The modeled time courses were concatenated across all nineteen subjects and four runs using the same arrangement used for the time-concatenated group ICA. The relationship between an independent component and the experimental variable was estimated by correlating the spatial component's data time course to the modeled BOLD response of the experimental variable. Since the movement-only and sensory-only conditions were presented in regular 15-second intervals, their modeled time courses were used to identify the functional brain network associated with the task. Shown in Figure 3-S1, one particular task-related independent component (SM_L) had a high correlation ($r > 0.9$) with the movement-only condition. This component, shown in Figure 3-S1 below, will be referred to as the active sensorimotor network.

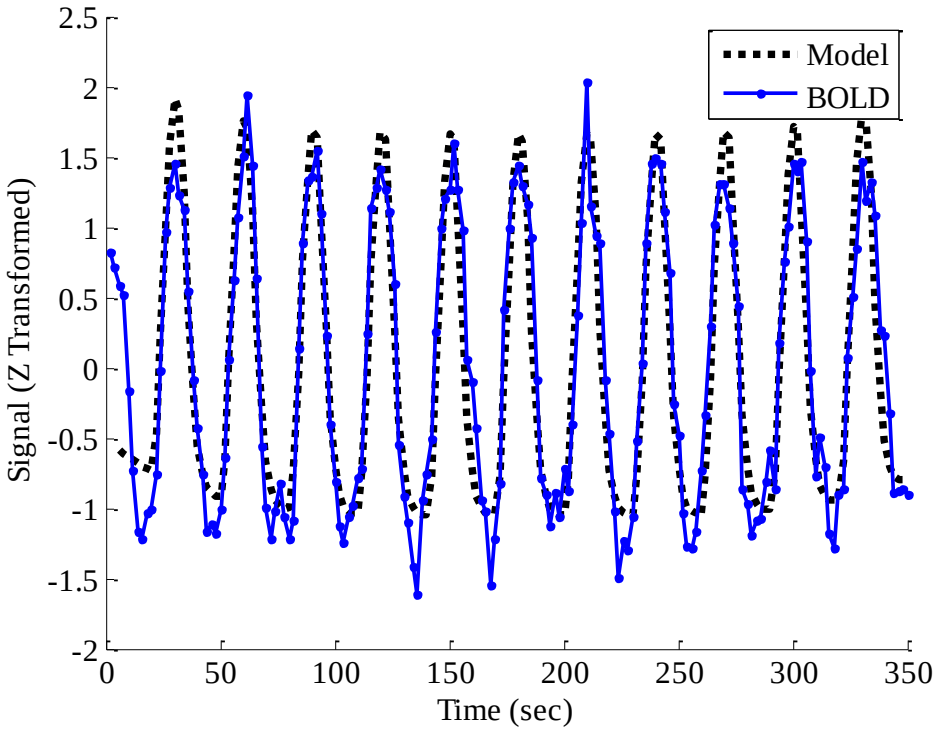

Figure S 3-1: Overlay of task-based network time-course and GLM model.

A comparison of the active sensorimotor network time-course (blue) and the modeled BOLD response to the motor-only condition (dotted black line) for a single control subject.

3.2.3.5. *Post-hoc* seed-based functional connectivity analysis

We were also interested in the functional connectivity between nodes within each identified functional network. Group ICA network maps were thresholded at a z-score of 30, and local maxima of clusters greater than 2 cm^3 were treated as nodes for a subsequent seed-based functional connectivity analysis. The z-score threshold and cluster size threshold were chosen heuristically such that only one or two clusters remained for each network. Shown in Table 3-1, a total of 27 local maxima were extracted from the left and right sensorimotor networks, the left and right parietofrontal control networks, the default-mode network, the bilateral cerebellar network, the bilateral

extrastriate visual network, the primary visual network, the left and right auditory networks, and the bilateral thalamic network. Since the task-fMRI data were also included in the ICA, the left sensorimotor network map contained three clusters. These included the left precentral gyrus, and two clusters within the right cerebellum. The inclusion of task-positive BOLD data also caused the right sensorimotor network's local maximum to occur within the postcentral gyrus. Since the contralesional sensorimotor network has been shown to be involved in motor plasticity after stroke, the nodes from left and right sensorimotor networks were reflected over the mid-sagittal plane to produce 4 additional nodes. Independent components that were related to motion or cardiac artifact were regressed out of the raw BOLD data. The six motion regressors that were calculated by the MCFLIRT function prior to the group ICA were also used to clean the original BOLD data. The temporal correlation coefficient was calculated from the cleaned BOLD time courses of each pair of seed points.

Network	Region	x	y	z
DMN	Precuneus	0	-55	26
DMN	IPL left	48	-63	30
DMN	IPL right	-40	-59	30
PF left	aPFC left	44	-55	42
PF left	IPL left	48	33	18
PF right	aPFC right	-28	-63	38
PF right	IPL right	-44	17	22
SM left	M1 left	36	-19	62
SM left	Cbl ant right	-24	-51	-30
SM left	Cbl post right	-24	-55	-58
SM left *	M1 right	-36	-19	62
SM left *	Cbl ant left	24	-51	-30
SM left *	Cbl post left	24	-55	-58
SM right	S1 right	40	-31	42
SM right *	S1 left	-40	-31	42
Cbl	Cbl left	24	-67	-38
Cbl *	Cbl right	-24	-67	-38
Vis	V1 left	-20	-91	-6
Vis *	V1 right	28	-91	-6
Visual Ext.	V5 right	44	-59	-18
Visual Ext.	V5 left	-40	-67	-10
Aud left	A1 left	64	-7	-2
Aud right	A1 right	-56	-11	2
Thal	Thal right	-24	9	-6
Thal	Thal left	28	13	-6

Table 3-1: Locations used for seed-based FC analysis.

3.2.4 Statistical analyses

3.2.4.1. Voxel-based analysis of BOLD activation maps and spatial network maps

Three BOLD activation maps from AFNI and two spatial network maps from the dual regression analysis were compared between subject groups and conditions by using voxel-based Student's t-tests. Since we were focused on sensorimotor function in this study, only the spatial maps of networks included in Table 3-1 were analyzed. Voxel-level Student's t-tests were performed to test contrasts between stroke and control groups. In the functional network maps, additional paired t-tests were performed to determine

within-group contrasts between resting-state and search. Spatial clusters of significantly different voxels ($p < 0.01$) were identified. In order to account for multiple comparisons, clusters less than 11 voxels (704 mm^3) in size were excluded from analysis. The cluster threshold was determined using the ClustSim tool in AFNI. Multiple comparisons correction was further applied for the number of contrasts performed (3 activation maps and 20 functional networks).

3.2.4.2. Functional connectivity analysis

A Student's t-test with was performed between stroke subjects and age-matched controls for the edge strength between each pair of seed points. Multiple comparisons FWE correction was applied for the number of pairwise t-tests, which was (n*(n-1)/2) = (27*26/2) = 702.

3.2.4.3. Correlational analysis with clinical functional scores

We hypothesized that stroke-related differences in task-related BOLD activation and functional network spatial maps would be correlated with the clinical evaluations of sensorimotor impairment/function. A linear regression analysis was performed with each BOLD activation contrast and functional network maps as a predictor of the Box and Blocks Score for the impaired arm. The independent components that were compared between groups included the left and right sensorimotor networks. The p-values were multiplied by the number of analyzed networks to correct for multiple comparisons.

3.3 RESULTS

3.3.1 The search task produced cortical activation patterns within motor control and multisensory integration areas.

Figure 3-2 demonstrates that in young healthy individuals and in the age-matched control group, our search task successfully produced unique cortical activation patterns for different sensory conditions. Activity is reported where the group mean is significantly positive zero ($t > 2.79$, $p < 0.01$). Search task-related activation common to all conditions was detected in contralateral sensorimotor cortex, bilateral premotor cortex, bilateral somatosensory association cortex, and bilateral anterior cerebellum. Purely visual or auditory activity was found in the primary visual and auditory cortices. An inferior-to-superior spatial gradient in overlapping activation maps were seen along the bilateral occipital surface. The superior occipital gyrus activity was exclusive to unimodal auditory feedback condition. The middle occipital gyrus responded to the auditory and audiovisual conditions.

In young adults, there was unique activation during the audiovisual feedback condition within the bilateral dorsolateral prefrontal cortex and bilateral posterior parietal cortex, corresponding to the anterior and posterior multimodal association areas. BOLD activation in the control group that was age-matched to the stroke survivors was similar with the young healthy adults. However, this group did not have unique activation within the prefrontal and posterior parietal areas.

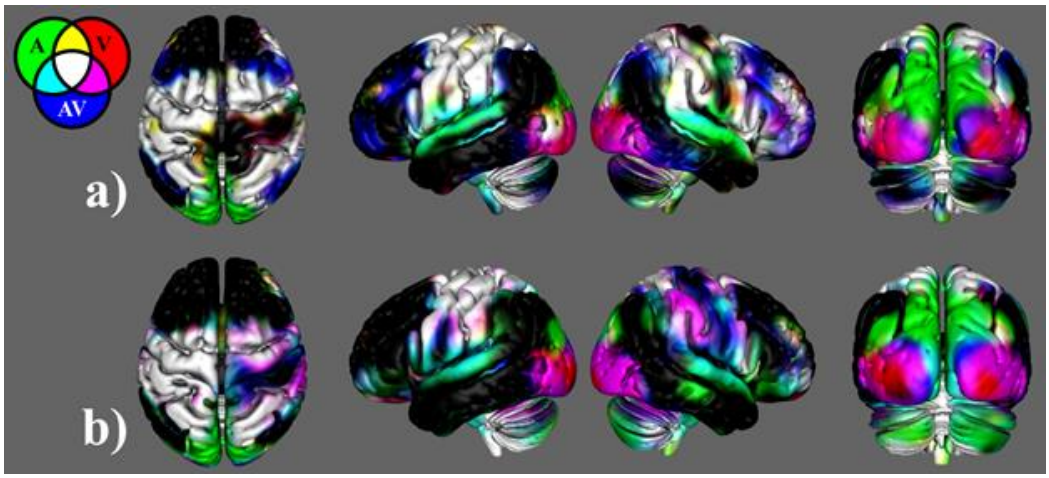

Figure 3-2: Search-task BOLD activation maps in healthy individuals.

These activations were produced from the novel search task paradigm. Mean BOLD activation for the auditory (A), visual (V), and audiovisual (AV) task conditions in (a) the young healthy adult group and (b) the control group age-matched to the stroke survivors.

3.3.2 During sensory-guided movement, BOLD activation in stroke survivors depends on sensory feedback modality.

Demonstrated in Figure 3-3 and Table 3-2, the BOLD activation in stroke survivors is dependent on the modality of sensory feedback. First, in the visual search condition, stroke survivors had similar activation to the age-matched controls within the active contralateral sensorimotor cortex. There was an increased activation in the contralesional prefrontal, posterior parietal, and sensorimotor cortices ($p < 0.01$). Increased activation was also observed within the ipsilesional prefrontal cortex ($p < 0.01$). Second, overall BOLD activity in stroke subjects was lower than controls during the auditory feedback condition. Since this effect was present in both low and high functioning stroke subjects, this decrease was not correlation with functional scores.

Thirdly, the task-related BOLD activity in stroke survivors during the audiovisual condition was not significantly different from the age-matched controls.

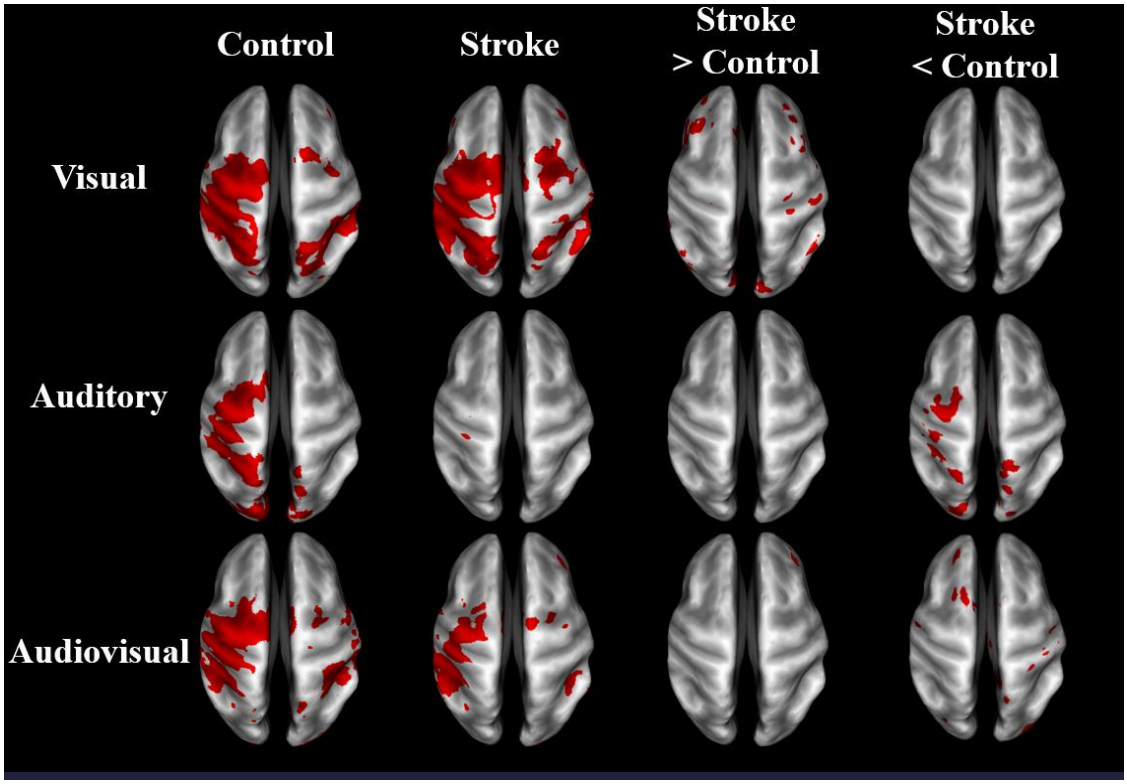

Figure 3-3: BOLD activation maps of stroke versus controls.

BOLD activation in visual, auditory, and audiovisual sensory guided movement. Group-averaged activity and significant differences ($p < 0.01$, corrected) are shown in stroke survivors (n=10) and controls (n=9) on inflated brain surfaces. The three sensory conditions had similar activation in the contralateral sensorimotor cortex, bilateral premotor cortex, and bilateral somatosensory association cortex. Stroke subjects had greater contralesional activation than controls during the visual condition and less ipsilesional activity during the auditory condition.

Table 3-2: Localized group differences in BOLD activation.

Condition	ROI	x	y	z	nVox	t	p (t)	corr B&B	p (slope)
Visual	MOG_R	46	-73	2	850	-3.16	†† 0.00636	0.716	† 0.03610
Search	STG_R	68	-17	2	655	3.49	†† 0.00321	-0.765	† 0.01972
	SPG_R	31	-62	63	35	-2.00	0.06249	0.851	†† 0.00389
	Cbl_R	10	-46	-59	12	-2.35	† 0.03182	0.697	† 0.04527
Visual	AG_L	-40	-75	49	96	2.34	† 0.03275	-0.845	†† 0.00471
Target									
Auditory	LG_L	-19	-82	-9	3616	-3.65	†† 0.00221	0.844	†† 0.00481
Search	LG_R	11	-80	-1	1234	-3.79	†† 0.00167	0.698	† 0.04486
	SPG_L	-27	-55	67	80	-2.73	† 0.01503	0.761	† 0.02112
	MCP_L	-12	-22	-33	50	-3.15	†† 0.00651	0.672	0.05666
	STG_R	30	24	-34	12	-2.00	0.06236	0.742	† 0.02676
	SPG_L	-15	-63	71	12	-4.27	†† 0.00062	0.655	0.06525
Auditory	STWM_L	-52	-21	-1	6027	-3.77	†† 0.00174	0.887	†† 0.00154
Target	Cu_L	-4	-96	6	963	-2.58	† 0.02122	0.916	†† 0.00049
	PoCWM_R	27	-35	74	528	-3.58	†† 0.00265	0.837	†† 0.00566
	Cbl_R	8	-82	-47	296	-5.21	†† 0.00009	0.698	† 0.04485
	IFG_R	35	17	14	166	-3.77	†† 0.00173	0.632	0.08274
	PrCG_L	-58	-1	24	86	-2.44	† 0.02772	0.848	†† 0.00427
	PrCG_L	-3	-30	74	37	-3.24	†† 0.00546	0.885	†† 0.00162
	STG_R	70	-22	-2	35	-3.63	†† 0.00235	0.590	0.11181
	MCP_R	21	-64	-35	34	-3.79	†† 0.00168	0.485	0.21533
Audiovisual	IOG_R	39	-77	3	643	-4.46	†† 0.00041	0.740	† 0.02721
Search	PTR_R	36	-61	0	484	-3.89	†† 0.00138	0.807	† 0.01023
Audiovisual	MTWM_L	-49	-49	1	70	4.77	†† 0.00022	-0.602	0.10391
Target	Cbl_L	-31	-88	-29	52	-1.54	0.14873	0.910	†† 0.00067
	ITG_L	-63	-53	-18	40	-3.55	†† 0.00282	0.712	† 0.03807
	STG_L	-47	-41	5	32	2.93	† 0.01033	-0.692	† 0.04777
	PoCWM_L	-39	-27	36	25	2.46	† 0.02672	-0.752	† 0.02369
	SPG_L	-31	-49	34	12	2.48	† 0.02587	-0.743	† 0.02650

†: $p < 0.05$, ††: $p < 0.01$

ROI Acronyms: IFG: inferior frontal gyrus, IOG: inferior occipital gyrus, MOG: middle occipital gyrus, STG: superior temporal gyrus, SPG: superior parietal gyrus, ITG: inferior temporal gyrus, SMG: supramarginal gyrus, LG: lingual gyrus, Cbl: cerebellum, PoCG: postcentral gyrus, PrCG: precentral gyrus, AG: angular gyrus, Fu: fusiform gyrus, MTG: middle temporal gyrus, MCP: middle cerebellar peduncle, PTR: posterior thalamic radiation

3.3.3 Stroke subjects have increased contralesional involvement within the task-related sensorimotor network

Functional connectivity information provided by the independent component analysis complemented the BOLD activation results, as shown in Figure 3-4. Figure 3-4a

presents the network that had the highest temporal correlation the recorded movement. This network includes the contralateral sensorimotor cortex, bilateral premotor cortex, and ipsilateral cerebellum had the highest temporal correlation with the modeled BOLD response (0.716 across all subjects). During both rest and the search task, this movement-related network was similar between stroke subjects and age-matched controls. In controls, the participation of sensorimotor cortices became lateralized during the task. Both hemispheres contributed to this shift in laterality, with greater positivity in contralateral sensorimotor areas and negative coefficients in the ipsilateral sensorimotor cortex. There was also an increased bilateral contribution from the supplementary motor area. These task-related network changes were not seen in stroke subjects. Rather, contralateral somatosensory cortex and ipsilateral SMA and ventromedial premotor cortex increased in network participation. Thus, stroke subjects had greater network participation in the ipsilateral hemisphere during the search task. This result also held after subtracting the resting-state network values.

As shown in Figure 3-4b, cortical areas within the ipsilateral sensorimotor network became less positive during the search task in control subjects, further suggesting task-related inhibition of ipsilateral cortex in healthy individuals. These decreases were not present in stroke survivors, but increased participation was found in the ipsilateral dorsolateral prefrontal and posterior parietal cortex.

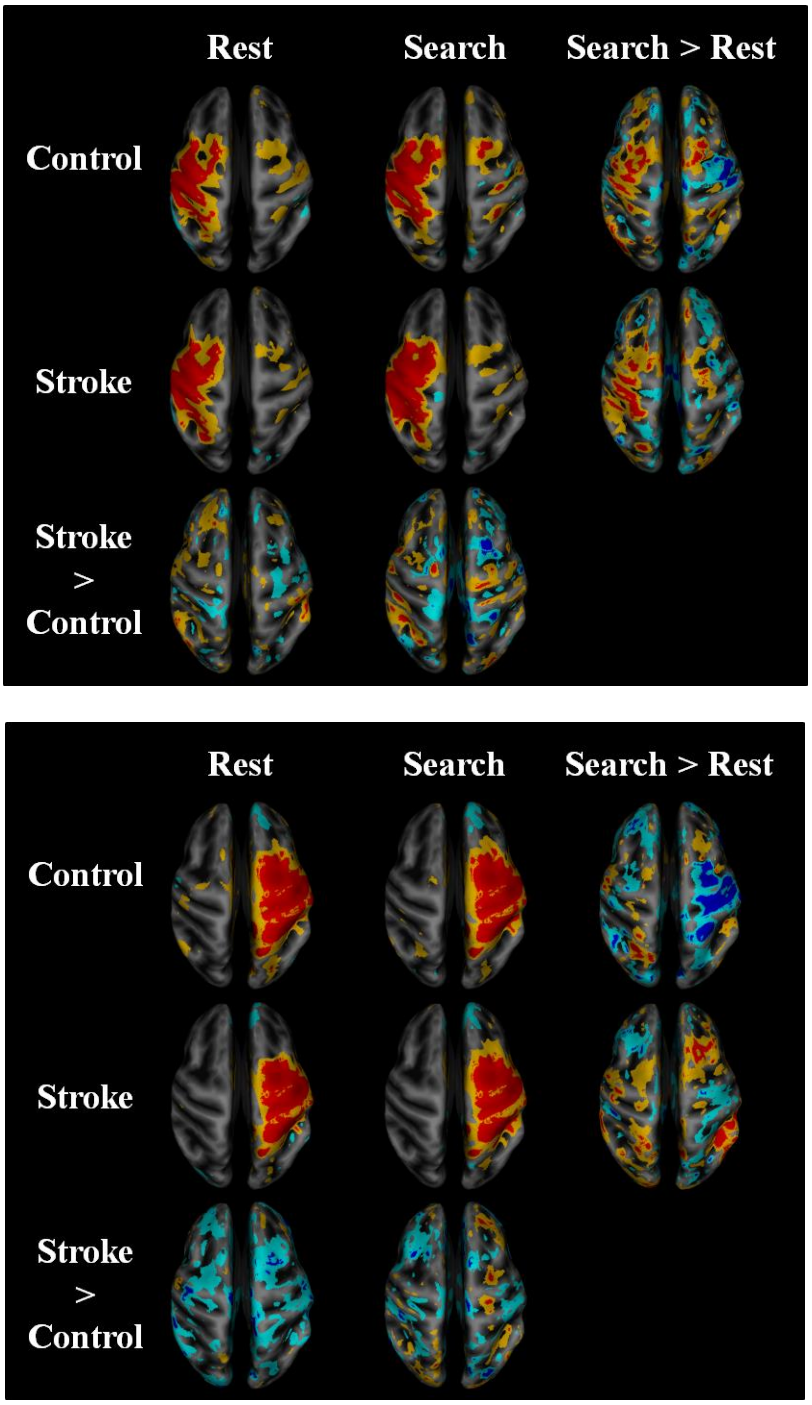

Figure 3-4: Stroke versus controls functional network maps.

Independent component spatial maps for the ipsilesional/contralateral (a) and contralesional/ipsilateral (b) sensorimotor networks. Stroke and control group averages and differences for rest and task conditions are overlaid on an inflated cortical map surface. Group averages with a mean normalized component intensity above 3 are colored red. Difference maps show clusters greater than 704 cubic millimeters after thresholding at $p < 0.01$.

Table 3-3: Localized group differences in network spatial maps.

Run	IC	ROI	x	y	z	nVox	t	p (t)	corr B&B	p (slope)
Rest	Right PF	ITG_R	44	-1	-44	13	-3.42	†† 0.00360	0.928	†† 0.00028
	DAN/CblL	SMG_R	68	-33	20	11	3.72	†† 0.00188	-0.794	† 0.01276
Search	V1 Medial	LWM_R	12	-81	0	32	-3.18	†† 0.00617	0.853	†† 0.00377
	Left SM	Cbl_R	44	-65	-40	54	3.71	†† 0.00192	-0.915	†† 0.00049
	Left SM	Cbl_R	32	-53	-24	39	-3.26	†† 0.00515	0.883	†† 0.00171
	Left SM	PoCWM_L	-20	-33	40	35	3.52	†† 0.00301	-0.857	†† 0.00347
	Left SM	PrCG_R	36	-5	60	17	-4.43	†† 0.00043	0.899	†† 0.00097
	Right PF	AWM_R	36	-53	32	11	2.99	†† 0.00900	-0.732	† 0.02957
S xor M	Right Insula	Fu_R	28	-81	-8	12	2.64	† 0.01955	-0.953	†† 0.00020
	DMNmpf	MTG_L	-60	-21	-16	11	-4.28	†† 0.00069	0.892	†† 0.00305
	Left SM	Cbl_R	50	-61	-44	22	3.12	†† 0.00720	-0.965	†† 0.00007
	Left SM	Cbl_R	36	-53	-28	17	-3.01	†† 0.00903	0.810	† 0.01711
	Central M1	Cbl_R	36	-77	-40	11	-3.81	†† 0.00177	0.913	†† 0.00152

†: $p < 0.05$, ††: $p < 0.01$

ROI Acronyms: ITG: inferior temporal gyrus, SMG: supramarginal gyrus, LWM: lingual gyrus, Cbl: cerebellum, PoCWM: postcentral gyrus, PrCG: precentral gyrus, AWM: angular gyrus, Fu: fusiform gyrus, MTG: middle temporal gyrus.

IC Acronyms: PF: parietofrontal control network, DAN: dorsal attention network, V1 medial: central visual network, SM: sensorimotor network, DMNmpf: default-mode network medial prefrontal node.

3.3.4 Stroke survivors have decreased interhemispheric connectivity and increased intrahemispheric functional connectivity to visual areas.

Functional connectivity between independent components at rest and during the search task are shown in Figure 3-5. The resting-state functional connectivity between left and right sensorimotor networks was lower ($p < 0.05$) in the stroke group, but there was no correlation with the clinical measures. The left and right parietofrontal networks also had lower internetwork and intranetwork functional connectivity during the search task.

3.3.5 Decreased functional connectivity with the cerebellum during sensorimotor integration correlates with motor impairment after stroke.

Figure 3-6 shows that decreases in functional connectivity to the cerebellum and visual association areas is correlated with Box and Blocks Score in individuals with stroke. In stroke subjects, the contralesional cerebellum had decreased functional connectivity with the active sensorimotor cortex ($p < 0.005$). As shown in Figure 3-7, this decrease is negatively correlated with Box and Blocks score ($R^2=0.744$). Lower functioning stroke survivors have reduced functional connectivity between the cerebellum and primary motor cortex correlate, as well as between the left and right extrastriate visual network nodes. These data are plotted in Figure 3-7.

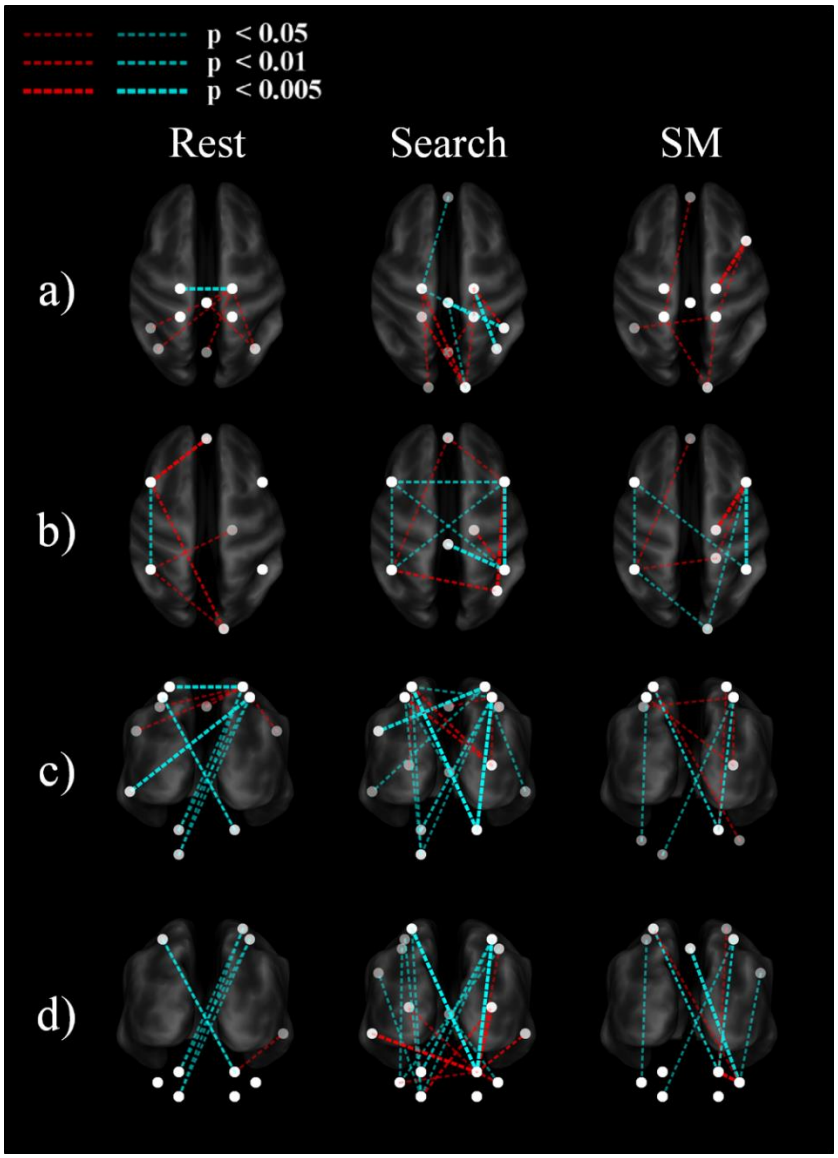

Figure 3-5: Group differences in functional connectivity.

An inflated pial surface of a template brain is shown with color-coded independent components and functional network graph overlay. Increased connections are in red and decreases are in cyan. The overhead view in a) shows the connectivity to the left and right sensorimotor network nodes and in b) presents connectivity to the bilateral parietofrontal networks. c) The posterior views show connectivity differences to four c) sensorimotor network nodes and d) eight cerebellar nodes.

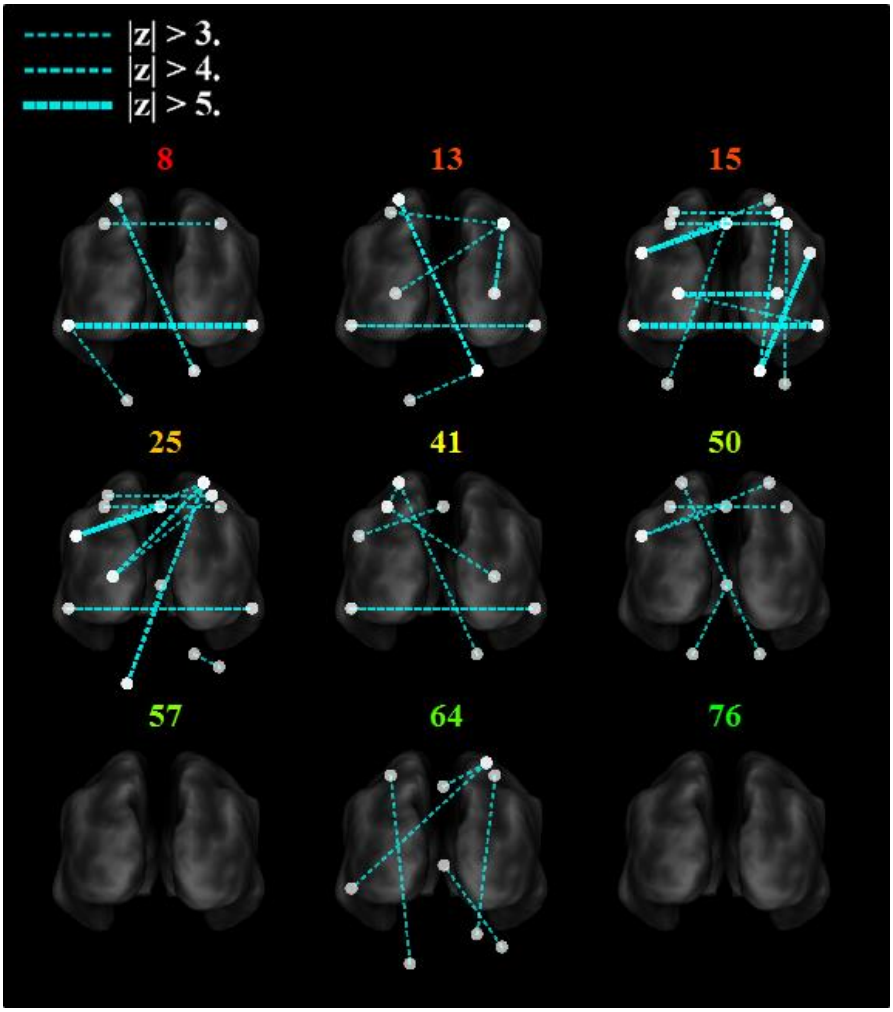

Figure 3-6: Functional trends in seed-based functional connectivity.

Differences in functional connectivity in stroke survivors during the search task correlate with Box and Blocks Score.

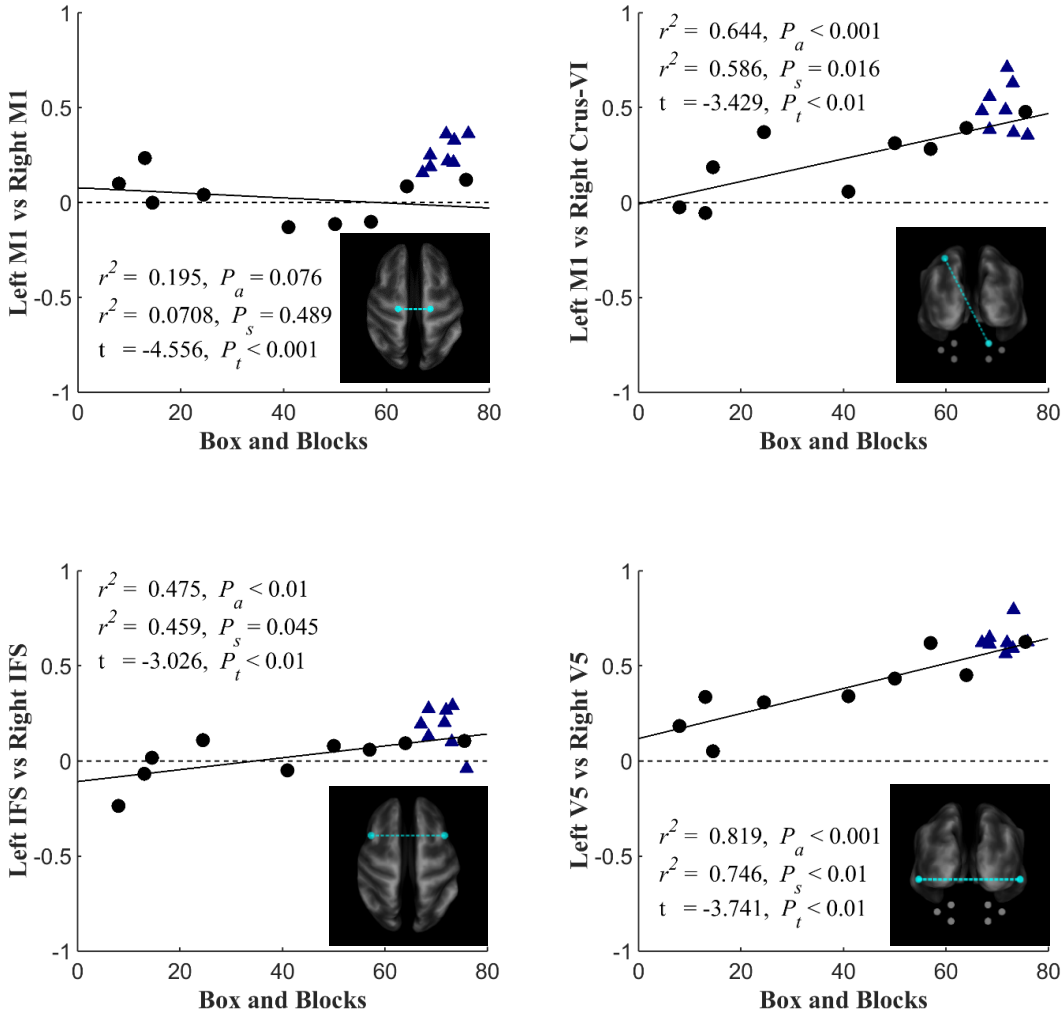

Figure 3-7: Scatterplots of seed-based connectivity versus motor function.

Stroke subjects are shown with black dots and controls are shown with blue triangles. The dependent variable in each plot is the partial correlation between two specified seed points. Linear regressions were performed within stroke subjects and repeated across all subjects (assuming that controls scored a 76). The first r^2 and P_a are the coefficient of variation and slope's p-value for the regression analysis across all subjects. The second r^2 and P_s are associated with the analysis that included only stroke survivors. Group differences are reported by t-value and corresponding P_t-value.

3.4 DISCUSSION AND CONCLUSIONS

The level of motor impairment was associated with decreased functional connectivity between the ipsilesional sensorimotor cortex and the cerebellum of the opposite hemisphere. Connectivity between sensory association areas was decreased in stroke, but these areas also increased connectivity with primary sensory and motor cortices. This suggests that association areas favor local integration over whole-brain integration. Our third observation was an increased connectivity between the sensorimotor to visual cortex, suggesting a dependence on visuomotor pathways in stroke survivors. All of these changes were correlated with Box and Blocks.

In addition to reproducing results of past studies, this work revealed new insights into cerebellar functional connectivity after stroke specifically during sensorimotor integration. Involvement of the cerebellum in different networks involving movement and multisensory integration give it a critical role in brain plasticity after stroke (Proville et al., 2014). The motor cortex and cerebellum together have been shown to be involved in plasticity during motor training and in sensorimotor integration (Baarbé et al., 2014). Voxel-based analysis of the ipsilesional sensorimotor network and seed-based correlations within this network both demonstrate a loss in connectivity to the cerebellum in lower functioning stroke subjects. Past imaging studies have shown that the cerebellum and parietofrontal networks are involved in sensorimotor function. Visual information is carried from the visual cortex to the dorsolateral pons and then passed to the cerebellum. It is thought that auditory information has a similar pathway through the pons. The two lowest functioning subjects had lesions to the pons and cerebellum.

Reduced functional connectivity between the left and right V5 was strongly correlated with fine motor control function in stroke individuals. The middle temporal gyrus plays a role in integrating visual and auditory information during movement. While this region has been classically associated with the primary language pathways, its functional connectivity has recently revealed a broader role in motor control (Bauer et al., 2012). During the search task, functional connectivity between the MTG and parietofrontal nodes increased. The MTG may also link unimodal visual association cortex with the posterior parietal multisensory association area. Lower interhemispheric functional connectivity between the bilateral middle temporal gyri in stroke survivors may allow for independent coupling within each hemisphere. The basal ganglia also integrate sensory information during movement (Bauer et al., 2012) , and in this study the contralesional lentiform nucleus was observed to increase in functional connectivity with the insular cortices.

Ipsilesional cortical activity was greater than controls during the visuomotor task, and there was an increase functional connectivity between sensorimotor and visual areas. During the auditory feedback conditions their performance was lower than controls, and auditory cortex was less active. Limited literature has shown that individuals with stroke have severe auditory processing deficits (Bamiou et al., 2012). Imaging studies have shown that stroke survivors with deficits in auditory comprehension have a common lesioned area in the middle temporal gyrus (Bates et al., 2003) . In our study, two subjects had lesions to the MTG. Individuals with stroke have been shown to rely on visual feedback for posturing (Bonan et al., 2004).

Head motion is a potential confounding factor in any study using functional activity or connectivity MRI, especially those involving task-based paradigms and patient populations. Indeed, head motion has been found in past studies to be greater in patients than in controls, but also increases with age (Van Dijk et al., 2012). Van Dijk *et* al. found in young adults that although most variability in functional connectivity was not associated with head movement, there was significantly reduced functional coupling between the parietofrontal and default-mode network nodes. Furthermore, greater mean head motion led to increased local functional coupling and interhemispheric connectivity between sensorimotor areas. Stroke subjects in this study undesirably had significantly greater mean head motion than controls ($p < 0.05$) at rest and during the search task. Thus, our findings that stroke survivors had decreased connectivity within parietofrontal networks and increased local connectivity could be in part due to increased head motion. However, we observed decreased interhemispheric connectivity, opposite to what was observed by Van Dijk *et* al. Since head motion was regressed out of the original data before our seed-based analysis, we do not believe that it was the prime contributor to our findings.

Changes in vasculature after stroke can lead to differences in neurovascular coupling near the lesion, which may influence correlations of these voxels with distant areas. Differences in brain structure can have an impact on functional connectivity metrics due to changes in the partial volume of gray matter (Dukart and Bertolino, 2014). Using simulations, Dukart *et* al. showed that between-group differences in brain structure leads to significant differences in functional connectivity between the groups. Due to the

large variability in lesion location in this study, partial volume was not expected to have a significant impact on functional connectivity results.

Non-stroke related lateralization of cortical activation and functional connectivity is a potential confounding factor in this study. Studies of healthy adults have shown significant lateralization of resting-state functional connectivity (Nielsen et al., 2013). Nielson *et* al. showed that there are twenty "lateralization hubs" that have the most lateralized functional connectivity. Some of these hubs included the dorsolateral prefrontal cortex, supplementary motor area, premotor cortex, Broca's area, insula, and junctions between the parietal, occipital, and temporal lobes. Many of these regions are unimodal and multimodal sensory association areas. Handedness of our subjects and the procedures of flipping the brain over the mid-sagittal plane could have also had an impact on the results.

In conclusion, sensorimotor and multisensory association networks decrease in interhemispheric and intranetwork connectivity. However, new intrahemispheric networks are formed between nodes from the lost networks. Future work will investigate the role of structural connectivity in these mechanistic changes between sensorimotor and sensory integration networks.

CHAPTER 4: STRUCTURO-FUNCTIONAL CONNECTIVITY REVEALS GREATER IMPACT OF STROKE LESIONS

4.1 INTRODUCTION

Resting-state functional magnetic resonance imaging and diffusion MRI together provide unprecedented insight into the structure-function relationship associated with changes in brain connectivity after stroke. This information might be useful for prognosis in the acute stages of stroke and could help to personalize rehabilitation strategies. Consequently, the purpose of this study was 1) to develop a novel connectivity model that marries structural and functional connectivity analyses, and 2) to demonstrate that it provides unique information about subject-specific changes in brain connectivity that may be used to develop new biomarkers for functional recovery.

Diffusion magnetic resonance imaging has provided potentially useful tools for detecting changes in white matter structure and structural connectivity following stroke. One such tool, high angular-resolution diffusion imaging (HARDI) (Tuch et al., 2002) involves multiple measurements of the diffusion coefficient within each voxel for many directions. From these directional data, an orientation distribution function (ODF) of white matter fibers within a voxel can be estimated with techniques such as q-ball imaging (Tuch, 2004). Diffusion MRI tractography uses these directional diffusivity measurements to model white matter fiber pathways. Deterministic tractography approaches propagate modeled fibers along the principle direction of diffusion (Zhang et al., 2009), while probabilistic approaches add random perturbations to estimate a distribution of structural connections to a voxel. Measures of structural connectivity of the brain can then be calculated based on these tractography models, and applied to the

brain of stroke survivors. Structural connectivity analyses automatically locate changes in fiber pathways after stroke (Yeh et al., 2013), and retained connectivity is associated with higher motor function (Buch et al., 2012).

Resting-state functional magnetic resonance imaging (rs-fMRI) can be used to measure low-frequency oscillations in cortical activity that are associated with functional connectivity of the brain. In this approach, measurements are made while the subject lies in a scanner with their eyes closed, making it attractive for clinical use. The rs-fMRI data are often analyzed using an independent components analysis (ICA) to automatically extract sets, or networks, of voxels that follow a common pattern of signal change (Beckmann and Smith, 2004; Beckmann et al., 2009; Du and Fan, 2013; Park et al., 2014; Rytty et al., 2013). Each independent component includes a spatial volume of voxel contributions and a common signal time-course. When applied to stroke, resting state fMRI has provided evidence of cortical reorganization associated with motor recovery, with the most common finding of reduced interhemispheric functional connectivity between sensorimotor cortices (Rehme and Grefkes, 2013). Network measures have also been used to characterize longitudinal changes in the motor execution network (Wang et al., 2010) during recovery after stroke.

Multimodal MRI techniques that combine diffusion and functional MRI approaches provide the opportunity to identify effects of structural damage on brain functional connections in stroke survivors. In healthy individuals, there is a strong correspondence between the default-mode network, a distinct brain network that demonstrates strong functional connectivity at rest, and the density of anatomical connections between its nodes (Hagmann et al., 2008). Further, an inverse relationship

has been observed between fiber distance and functional connectivity (Sporns, 2011). A combined structural-functional connectome (Horn et al., 2013) has been described using correlations between the structural and functional connections of all voxels of the brain. The combined structural and functional connectivity information might be particularly useful in describing changes in function following localized brain lesions, such as those associated with stroke (Rehme and Grefkes, 2013).

In this chapter, we introduce a new automated analysis that expresses functional connectivity in the context of structural connectivity while avoiding constraints on either individual analysis. Our approach first calculated the functional connectivity for all structurally connected voxels of the brain. We then identified average levels of functional connectivity to a voxel for regions that were structurally connected at similar distances. A novel structuro-functional correlation (SFC) that identifies maximum functional connectivity to a voxel across these distances was obtained. The SFD was then used to enhance resting-state networks derived from conventional fMRI connectivity analyses. These spatial enhancements were validated through correlational analyses with clinical assessment scores.

4.2 METHODS

4.2.1 Data Collection

4.2.1.1 Subject Recruitment and Functional Testing

Ten individuals with chronic post-stroke hemiparesis (4 female, age 66.7 ± 7.94 years, at least 1.1 years since stroke), and nine age-matched control subjects (5 female, age 64.2 ± 7.73 years) participated in this study. The experimental protocol was approved by the Institutional Review Boards of Marquette University and the Medical College of Wisconsin, and written consent was obtained from each subject. Inclusion criteria included a history of stroke that occurred no less than 6 months prior to recruitment. Stroke subject information is provided in Table 4-1. Subjects with no ability to perform supination, pronation, ulnar deviation, or radial deviation of the wrist were excluded. Control subjects were comprised of individuals without history of stroke or other neurological impairments that were age-matched (within 3 years) and gendered-matched to the stroke subjects. Each stroke subject completed the upper extremity (UE) portion of the Fugl-Meyer Assessment (Fugl-Meyer, 1975), the Box and Blocks Test of Manual Dexterity (Mathiowetz et al., 1985) and the Wolf Motor Function Test (Wolf et al., 2001) for upper extremity motor ability.

Subject ID	S04	S05	S07	S08	S10	S12	S14	S15	S16	S18
Sex	M	M	F	M	M	F	M	F	F	M
Age	65	57	83	66	69	65	64	80	62	66
Lesion Location	Cort	Subc	BS	Subc	Cort	Cort	Cbl	Subc	Subc	Subc
Lesion Side	R	L	L	L	L	R	L	L	L	L
Arm Affected	L	R	R	R	R	L	L	R	R	R
Dominant Post	R	R	L	R	R	R	R	R	R	R
Dominant Pre	L	R	R	R	R	Amb	R	R	R	R
Wolf Motor	71	72	38	72	75	54	58	74	75	74
Fugl-Meyer	124	106	82	122	124	97	120	126	124	122
Box & Blocks (ND)	24.5	62.5	8	41	75.5	14.5	13	57	50	64

Table 4-1: Stroke subject information

Cort=Cortical, Subc=Subcortical, BS=Brainstem, Cbl=Cerebellum

4.2.1.2 MRI Scans

Every subject was screened for MRI safety according to the Medical College of Wisconsin Institutional Review Board before entering the magnetic environment. An axial T1-weighted anatomical image was acquired using a fast spoiled gradient recalled (SPGR) pulse sequence, with TE: 3.2 ms, TR: 8.16 ms, flip angle: 12 deg, prep time: 450, bandwidth: 22.73, FOV: 240 mm, 156 1mm slices, matrix size: 256x240. Next, an axial q-ball high angular resolution diffusion imaging sequence was acquired with a single-shot echo planar imaging sequence, including 5 b=0 images, 150 diffusion-weighted directions, SENSE parallel imaging, TE: 72.3 ms, TR: 5700 ms, FOV: 250 mm, matrix size: 128x128 resampled to a 256x256 grid (2mm pixel width/height), and 57 2.5 mm slices. The 2.5 mm slice thickness was needed for cerebellum coverage in subjects with larger heads. For functional MRI, a sagittal view gradient-echo echo-planar sequence was acquired with TE: 25 ms, TR: 2000ms, flip angle: 77 deg, FOV: 240mm x 240mm, 41 slices with 35 mm thickness.

4.2.2 MRI Data Processing

4.2.2.1 Intersubject Anatomical Image Registration

Fully automated techniques were used for intersubject and intermodality image registration. Anatomical T1-weighted images were registered to the 152-MNI template from fMRI of the Brain Software Library (FSL). First, the FLIRT tool from FSL (Jenkinson and Smith, 2001) was used to perform linear affine regitration to translate and rotate the brain . The anatomical images were then deformed to MNI space using an ITK implementation of the Maxwell's demons algorithm (Thirion, 1998).

4.2.2.2 Lesion-side Normalization

Lesion-side normalization was performed by flipping each row of data in the x-dimension in stroke survivors with right lesions. This correction was done prior to anatomical image registration. However, the orientation distribution function (ODF) estimation and diffusion MRI tractography were performed with the raw diffusion MRI data. The resulting fractional anisotropy (FA) map was flipped and registered to the subject's flipped T1-weighted image using a 12-parameter affine registration. The BOLD fMRI data was similarly flipped and registered to the anatomical image. Intermodality and intersubject registration results were concatenated in order to map each subject's BOLD and diffusion images to MNI coordinates. Fiber trajectories were flipped over the mid-sagittal plane before warping into MNI space.

4.2.2.3 Resting-state Network Calculation

Resting-state networks were determined from raw BOLD time-course data using the Multivariate Exploratory Linear Decomposition into Independent Components (MELODIC) Version 3.14 available with the FSL (www.fmrib.ox.ac.uk/fsl). All 19 subjects were time concatenated for a single group ICA. The data were high-pass filtered with a cutoff of 100 seconds (Marchini and Ripley, 2000). Before time-concatenation, five TRs were discarded from each subject, leaving 175 volumes over 350 seconds. The functional image volumes were motion corrected using the MCFLIRT implementation (Jenkinson et al., 2002). Slice-time correction was applied using linear interpolation. Skull-stripping was automatically performed with the brain extraction tool (BET) (Smith, 2002), and the data were spatially smoothed with a 4 mm full-width half-max Gaussian kernel. The brain mask was used to exclude non-brain voxels from the remaining analysis. All subjects were spatially normalized to an anatomical MNI standard template using a 12-parameter affine registration implemented in FLIRT (Jenkinson and Smith, 2001). The voxel BOLD times series were demeaned, variance normalized, and whitened.

The number of independent components was estimated using a Bayesian approach described in (Minka, 2000). Using Probabilistic Independent Component Analysis (Beckmann and Smith, 2004), the whitened time data were projected onto a 83-dimension subspace. A fixed-point method (Hyvarinen, 1999) decomposed the data into 83 independent components that accounted for variability in temporal, spatial, and subject domains. The spatial components were normalized by the variance of the residuals, and a

mixture model was fit to their intensity histograms to determine a statistical threshold (Beckmann and Smith, 2004).

Once the group independent components were calculated, a dual regression (Beckmann et al., 2009) was used to estimate subject-specific spatial maps and time courses. Components with vertical stripes in the axial view were associated with motion and excluded from further analysis. 45 of the 83 components were excluded due to high amounts of frequency content above 0.1 Hz or were determined to be related to anatomical artifacts. The MELODIC tool was used to regress these components out of each subject's original fMRI data. Voxel-based t-tests were performed between stroke and age-matched controls for each independent component.

4.2.2.4 Structural Connectivity Analysis

The high-resolution diffusion-weighted images were processed with the Diffusion Toolkit to estimte the fiber orientation and model fiber tracts (Wang et al., 2007). At each voxel, Q-ball reconstruction was performed with 181 reconstruction points and 150 measurement points. Since access to the fiber trajectories was required for our model, the deterministic tractography module was used from the Diffusion Toolkit. Diffusion MRI tractography was performed in the subject's native space. At each voxel, 30 seeds were randomly distributed and a fiber trajectory was reconstructed. This path was warped into MNI space using a combination of the subject's intermodality registration and anatomical intersubject registration. Stopping criteria included an angle threshold of 35 degrees. These fibers were stored for later data analysis.

4.2.2.5 Structuro-functional Correlation

In this model, every fiber endpoint voxel was treated as a potential network node. All processing that combines structural and functional connectivity was performed in MNI space. Thus, both BOLD data and fiber trajectories were both spatially normalized using the anatomical image registration.

Rather than analyzing the functional connectivity of a voxel to every structurally connected location, signal averaging is first performed across connections by similar fiber path distance. Note that this model makes an assumption that functionally connected nodes in a network can be both distinguished and grouped by fiber distance in a meaningful way. Also note that since averaging was performed with fiber length fixed, metrics within this framework may be less biased by tractography seeding and spatial variations in fiber density.

To describe the analysis, first let $V(\mathbf{x}, l)$ be a map that provides a set of *N* voxel locations, $\{\mathbf{y}_1, \mathbf{y}_2, \ldots, \mathbf{y}_N\}$, that are structurally connected to voxel **x** by fibers with length l. Although *N* will vary with **x**, we write it as a constant in subsequent equations for simplicity. Let $S(\mathbf{x}, t)$ be the BOLD signal at time t and physical location **x**, with $\mathbf{x} \in \mathbb{R}^3$. With time fixed at frame , averaging this function across $V(\mathbf{x}, l)$ gives a new weighted time signal, $Z(\mathbf{x}, t, l)$. Let this structurally connected mean fMRI signal be

$$Z(\mathbf{x}, t, l) = N^{-1} \sum_{i=1}^{N} S(\mathbf{y}_i, t) \quad : \quad \mathbf{y}_i \in V(\mathbf{x}, l) \qquad \text{(Eq. 1)}$$

In this study, we were interested in the level of functional connectivity to the ensemble of structural connections at different fiber distances from a voxel. Here, we

define the structuro-functional correlation (SFC) index as the temporal correlation with a voxel's structurally connected mean fMRI signal at distance l,

$$\mathrm{SFC}_l\big(\mathbf{x}, f(t)\big) = \mathrm{Corr}\big(Z(\mathbf{x}, t, l), f(\mathrm{t})\big). \quad \text{(Eq. 2)}$$

If SFC is maximized over all fiber lenghs, then it provides the maximum functional connectivity of an arbitrary function, $f(t)$, to the structural connections of **x** at distance l. Here, we denote $\hat{l}$ as the fiber length that maximizes SFC. We define the maximum structuro-functional correlation (SFC_{max}) of voxel **x** as

$$\mathrm{SFC}_{\max}(\mathbf{x}, f(t)) = \mathrm{SFC}_{\hat{l}}(\mathbf{x}, f(t)) = \max_{l_{\min} \le l \le l_{\max}} \mathrm{SFC}_l(\mathbf{x}, f(t)). \quad \text{(Eq. 3)}$$

In the simplified example shown in Figure 4-1, the SFC is calculated for an arbitrary voxel **x** within the thalamus. Voxel **x** is connected to cortical voxels $\mathbf{y}_2$ and $\mathbf{y}_3$ by fibers with length l_1. The SFC of function $f(t)$ at length l_1 from **x** is its correlation with mean fMRI signal $\big(S(\mathbf{y_2}, \mathrm{t}) + S(\mathbf{y_3}, \mathrm{t})\big)/2$. Likewise, at fiber length l_2, **x** is structurally connected to cerebellar voxel $\mathbf{y}_1$. The SFC of $f(t)$ at distance l_2 from **x** is its correlation with $S(\mathbf{y_1}, \mathrm{t})$, which is the original BOLD signal at $\mathbf{y_1}$. SFC_{max} will be the larger of the correlations.

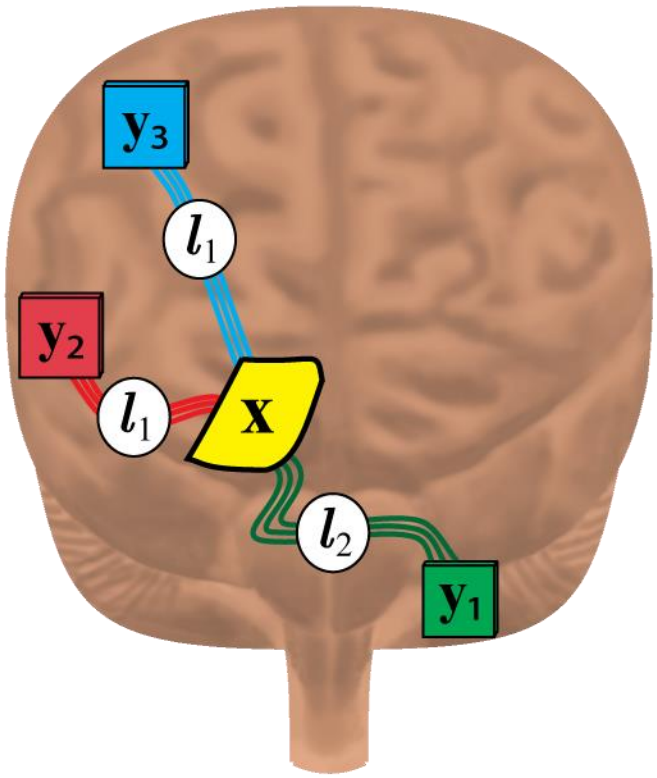

k	$V(\mathbf{x}, l_k)$	$Z(\mathbf{x}, t, l_k)$	$\mathrm{SFC}_{l_k}(\mathbf{x}, f(t))$
1	$\{\mathbf{y}_2, \mathbf{y}_3\}$	$\frac{S(\mathbf{y_2}, \mathrm{t}) + S(\mathbf{y_3}, \mathrm{t})}{2}$	$\mathrm{Corr}\left(\frac{S(\mathbf{y_2}, \mathrm{t}) + S(\mathbf{y_3}, \mathrm{t})}{2},\ f(\mathrm{t})\right)$
2	$\{\mathbf{y}_1\}$	$S(\mathbf{y_1}, \mathrm{t})$	$\mathrm{Corr}\big(S(\mathbf{y_1}, \mathrm{t}),\ f(\mathrm{t})\big)$

Figure 4-1: Example of SFC calculation.

Diagram depicting the structural-functional correlation (SFC) index of a thalamic voxel **x**. The SFC_{max} provides a maximum temporal correlation to the structural connections of **x** .

In the special case that $f(t)$ is the orginal BOLD signal at **x**, then SFC provides the functional connectivity of voxel **x** to its own structural connections. We define the intrinsic structuro-functional correlation (iSFC) as

$$\mathrm{iSFC}_l(\mathbf{x}) = \mathrm{SFC}_l\big(\mathbf{x}, S(\mathbf{x}, \mathrm{t})\big) \qquad \text{(Eq. 4)}$$

Combining this with Eq. 3, the maximum intrinsic SFC is

$$\mathrm{iSFC}_{\max}(\mathbf{x}) = \max_{l_{\min} \le l \le l_{\max}} \mathrm{Corr}\big(Z(\mathbf{x}, t, l),\ S(\mathbf{x}, \mathrm{t})\big) \qquad \text{(Eq. 5)}$$

4.2.2.6 Calculating the structural connectivity-weighted fMRI signal $Z(\mathbf{x}, t, l)$

The signal, $Z(\mathbf{x}, t, l)$, was calculated independently using Eq. 1 for each time frame, t, and fiber length interval, Δl. In this study, the minimum ($l_{\min}$) and maximum ($l_{\max}$) fiber distances were chosen as 20 mm and 300 mm. Eight intervals were chosen for this study: 20, 40, 70, 100, 130, 160, 190, 220, and 300 mm. A 4-D dataset with the same dimensions as the original fMRI data was created to store the filtered data for each fiber length interval. The fMRI signal $S(\mathbf{x}, t)$ had to be estimated for each fiber endpoint because of differences in resolution of the fMRI and anatomical images. Specifically, the signal at the endpoint of each tract was defined as the mean of the fMRI signals across the three endmost points of the fiber. Values at each of these three fiber points were extracted from the original fMRI signal by trilinear interpolation within MNI space. At each voxel, **x,** the weighted summation $Z(\mathbf{x}, t, \Delta l)$ was calculated as the sum of the structurally connected $S(\mathbf{x}, t)$**,** divided by the total number of fibers, N, at **x**. Thus, $Z(\mathbf{x}, t, \Delta l)$ is a mean BOLD signal across voxels that are structurally connected to **x**, for fibers within the specified length interval Δl.

4.2.2.7 Calculating the intrinsic structuro-functional correlation (iSFC)

According to Eqs. 2 and 4, each voxel's iSFC_l was calculated for every fiber length interval Δl. Next, using Eq. 5, the $\mathrm{iSFC}_{\max}$ at that voxel was calculated as the maximum iSFC_l.

4.2.2.8 Resting-state network enhancement based on SFC

Structural connections between and within different resting-state networks may have an impact on the functional integration of cortical regions involved in motor control after stroke. If $f(t)$ in Eq. 2 is a function of network activity, then the SFC becomes an enhanced form of that activity, or effectively, a connectivity map. ICA, as implemented in the MELODIC tool of FSL, decomposes the BOLD data $S(\mathbf{x}, t)$ into spatially independent networks, each with a spatial map, $M(\mathbf{x})$**,** and time-course, $A(t)$. As described by Joel *et al*. (Joel et al., 2011), these independent components are related to the original BOLD signal as

$$S(\mathbf{x}, t) = \sum_{j=1}^{J} M_j(\mathbf{x}) A_j(t) \qquad \text{(Eq. 6)}$$

By letting $f(t) = A(t)$, the resulting $\mathrm{SFC}_{\max}$ is an enhanced spatial map of a resting-state network's structural connections,

$$\mathrm{SFC}_{\max}(\mathbf{x}, A(t)) = \max_{l_{\min} \le l \le l_{\max}} \mathrm{Corr}(Z(\mathbf{x}, t, l),\ A(t)). \qquad \text{(Eq. 7)}$$

4.2.3 Statistical Analysis

4.2.3.1 Validation of enhanced resting-state network maps

Resting-state networks that were analyzed in this study included the posterior default-mode network (DMN), the prefrontal network (anterior DMN), the primary visual network, the ipsilesional and contralesional sensorimotor networks, the bilateral cerebellar network, and the basal ganglia network.

In order to validate the level of network map enhancement provided by SFC, it was compared against a correlation map of $A_j(t)$ and the original fMRI signal. Note that the independent component spatial maps, $M_j(\mathbf{x})$, in Eq. 6 are not correlation coefficients. Thus, SFC could not be compared directly with the original network maps. However, the correlation of the network's timecourse, $A_j(t)$, with the original BOLD signal, $S(\mathbf{x}, \mathrm{t})$, provided a composite network map with the greatest weight given to the j[th] network. We denote this baseline correlation as $r_0 = \mathrm{Corr}\left(S(\mathbf{x}, t),\ A_j(t)\right)$. Based on in Eq. 7 we then use a similar notation to define the enhanced correlation as $r_{SF} = \mathrm{SFC}_{\max}\left(\mathbf{x}, A_j(t)\right)$. The difference between the Fisher-transformed r_{SF} and r_0 was then used as a measure of network enhancement. The original and enhanced correlation maps were visualized for comparison using 3D isosurfaces at multiple isovalues.

4.2.3.2 Voxel-based analysis of group differences and clinical correlates

A voxel-based based analysis was used to measure differences in SFC between stroke survivors and age-matched controls. Metrics that were compared included the

intrinsic structuro-functional correlation ($iSFC_{max}$ in Eq. 5), and each enhanced resting-state network r_{SF}. In addition, the baseline and enhanced correlation maps for each resting-state network, r_0, and the SFC-enhanced correlation map, r_{SF}, of each resting-state network (Eq. 4) for the posterior DMN, prefrontal network, primary visual network, sensorimotor networks, cerebellar network, and basal ganglia network were compared. The Fischer transform was used to normalize r_{SF} and r_o for statistical testing. Stroke and control groups were compared by performing voxel-based Student's t-tests, using clusters of connected significant voxels that were more than 700 mm^3 in volume in order to correct for multiple comparisons. The initial t-tests were performed with an alpha of 0.01, and the 3dclustsim tool in AFNI was used to determine cutoff cluster sizes for a corrected p-value of 0.05. The maximum t-value, its MNI coordinate, and the size in number of voxels were reported for each cluster. A correlational analysis with behavioral measures in stroke subjects was performed by linearly regressing each voxel-wise metric with the Box and Blocks Score. The maximum Box and Blocks correlation coefficient was reported for each cluster of significant t-values. For the correlation analyses, p-values were not corrected based on multiple network comparisons. An F-test was used to test the slope of the Box and Blocks correlation for significance. Since clinical correlations were analyzed for significantly different clusters, no additional multiple comparisons corrections were applied.

4.3 RESULTS

4.3.1 Stroke survivors have decreased global structural-functional connectivity.

Shown by isosurfaces of the $iSFC_{max}$ metric in Figure 4-2, the voxels with greatest correlation maximized by fiber length were located within the precuneus, anterior cingulate gyrus, and sensorimotor cortex. Voxels having the greatest fiber length that maximizes functional connectivity were within the prefrontal and posterior parietal regions.

There are multiple brain areas in stroke survivors with significantly lower functional connectivity ($p < 0.01$) to their structural neighbors. Figure 4-2 shows that the $iSFC_{max}$ is greatest within the posterior parietal and sensorimotor areas within both controls and stroke survivors. The $iSFC_{max}$ was greater within the contralesional/right hemisphere in both groups. Nodes within the default-mode network have wide-spread decreases in functional connectivity in stroke survivors. Clusters that were significantly different in stroke survivors and correlated with Box and Blocks are shown in Figure 4-3 and Table 4-2. All significant differences ($p < 0.01$) in $iSFC_{max}$ were lower in stroke. These differences were located in the left superior frontal gyrus, left superior occipital gyrus, the right putamen, right superior frontal gyrus, the right cerebellum, the left midbrain, and the right insula. The only cluster with a maximum t-value that was also correlated with Box and Blocks was in the right/contralesional insula ($p < 0.01$, $R=0.770$).

Stroke survivors also had significant differences in the fiber distance, $\hat{l}$, associated with maximum intrinsic functional connectivity to a voxel, $iSFC_{max}$. There were

decreases in $\hat{l}$ within the contralesional hemisphere and increases in the ipsilesional hemisphere. The right postcentral gyrus, right superior frontal gyrus, and right insula all had significant decreases in $\hat{l}$.

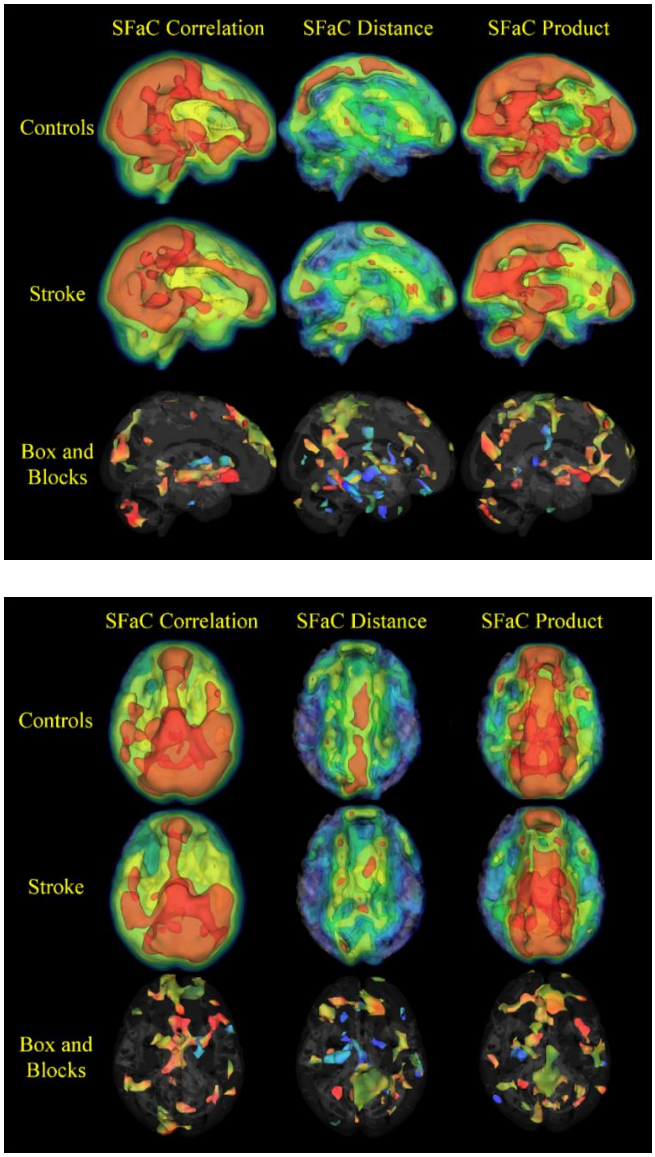

Figure 4-2: Intrinsic structuro-functional correlation in stroke and controls.

Shown are group differences in the structuro-functional correlation ($iSFC_{max}$ is displayed as $iSFC_{max}$) metric indicative of a voxel's maximum functional connectivity to structurally connected neighbors at a fixed fiber distance. SFC_{max} distance shows isosurfaces of distance associated with the maximum correlation. The SFC_{max} product displays the group averages and differences for the product of the first two metrics. On the bottom, clusters of significantly

different voxels ($p < 0.01$) with a minimum cluster size of $700mm^3$ are shown Correlation coefficients with Box and Blocks Score were used to color-code the cluster surfaces, with Red: R = 1.0; Green: R = 0.0; Blue: R = -1.0.

The product of the maximum functional connectivity and the fiber distance associated with that connectivity was used as a third metric to compare between stroke subjects and controls. This product was significantly lower ($p < 0.01$) in stroke subjects in the left cerebellum, frontoorbital gyrus, left middle frontal gyrus, left amygdala, right precentral gyrus, right insula, and left cuneus. The decrease within the left cerebellum was greater in stroke subjects with a lower Box and Blocks Scores (R=0.700).

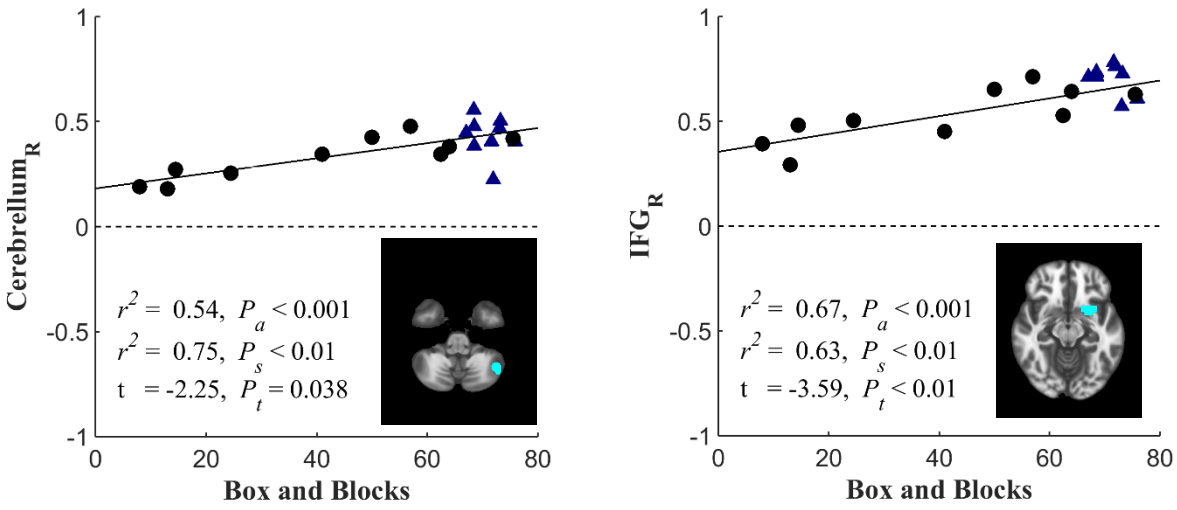

Figure 4-3: Scatter plots of clinical correlations with $iSFC_{max}$.

Scatterplots of the structuro-functional correlation ($iSFC_{max}$) spatial clusters significantly ($p < 0.01$) different between stroke survivors (black circles) and controls (blue triangles), and with significant correlations with Box and Blocks Score in stroke subjects. Regions shown include right inferior frontal gyrus (IFG_R) and right cerebellum.

†: p < 0.05, ††: p < 0.01

Metric	ROI	x	y	z	nVox	t	p (t)	corr B&B	p (slope)
SFCmax	IFG_R	38	27	-8	40	-3.55	†† 0.00262	0.781	†† 0.00916
coef	Cbl_R	34	-73	-40	30	-1.93	0.07368	0.859	†† 0.00163
	Midbrain_L	-2	-9	-12	21	-2.63	† 0.01840	0.606	0.07593
	Amyg_L	-10	3	-24	17	-1.61	0.12719	0.827	†† 0.00361
	AG_L	-46	-61	36	14	1.92	0.07522	-0.8023	†† 0.00624
	CingG_L	-2	-5	44	11	-1.75	0.10225	0.845	†† 0.00234
SFCmax	Thal_L	-14	-21	-4	50	1.98	0.06529	-0.814	†† 0.00492
dist	Cbl_L	-34	-49	-24	22	-3.22	†† 0.00536	0.631	0.05936
	ITG_L	-38	-13	-28	20	1.17	0.26051	-0.924	†† 0.00012
	Put_L	-22	19	0	12	2.16	† 0.04801	-0.692	† 0.03109
SFCmax	Ins_R	38	27	-4	30	-2.54	† 0.02228	0.783	†† 0.00865
prod	AG_L	-42	-61	40	27	2.41	† 0.02851	-0.758	† 0.01336
	STG_R	-62	-17	-4	15	-2.45	† 0.02651	0.786	†† 0.00801
	Cbl_L	-26	-49	-20	12	-3.89	†† 0.00124	0.704	† 0.02787
SFC(l=1)	IFG_L	38	31	-8	38	-3.18	†† 0.00578	0.705	† 0.02753
	Midbrain_R	-6	-13	-8	108	-3.47	†† 0.00312	0.697	† 0.02954
SFC(l=2)	PrCG_R	-26	-13	48	22	4.00	†† 0.00093	-0.699	† 0.02923
	SFG_R	-10	63	0	16	-2.56	† 0.02165	0.766	† 0.01189
	LFOWM_L	38	31	-12	32	-3.52	†† 0.00280	0.790	†† 0.00758
SFC(l=3)	MOWM_R	-26	-73	20	29	2.31	† 0.03439	-0.836	†† 0.00302

p-values are corrected for the number networks and metrics compared.

Table 4-2: Localized changes the structuro-functional correlation maps.

Student's t-values and Box and Blocks scores were both used to identify clusters for this table. The maximum t-value and its MNI coordinate are reported for each cluster. The maximum correlation with Box and Blocks Score is also reported. Clusters were identified by smoothing each metric map with a full-width-half-max Gaussian kernel of 4mm and performing voxel-wise t-tests between subject groups with initial p threshold of 0.01, followed by a minimum cluster size cutoff of 700mm^3.

4.3.2 Additional stroke-related differences in functional connectivity can be delineated with information provided by SFC at different fiber-lengths.

Voxel-wise differences in SFC between stroke survivors and age-matched controls reveal that network changes can be delineated at specific fiber lengths. As shown in Figure 4-4, the precentral gyrus has an increased functional connectivity ($p < 0.001$), specifically with its structural neighbors that are between 40-70mm in fiber distance. Likewise, stroke subjects have lower functional connectivity ($p < 0.001$), correlated with Box and Blocks ($R^2 = 0.58$), between the contralesional lateral

orbitofrontal cortex and its neighbors at this l=2 fiber length. These two connections approached a similar correlational strength and appeared to mirror one another across stroke subjects, as shown in Figure 4-4c.

4.3.3 Structural-functional correlation enhanced areas of the brain within each resting-state network.

Each resting-state network had additional regions enhanced by structural connectivity with the new SFC metric. As seen in Figure 4-5, the basal ganglia have enhanced connectivity to the amygdala, precentral gyrus, and frontal areas. The prefrontal network has enhanced connections to the precuneus, the cerebellum, and brainstem areas. An independent component that was localized to the medulla was enhanced throughout the brain at projection fiber endpoints. The primary visual network was enhanced completely along the pathway from V1, to the thalamus, and finally the orbitofrontal gyrus.

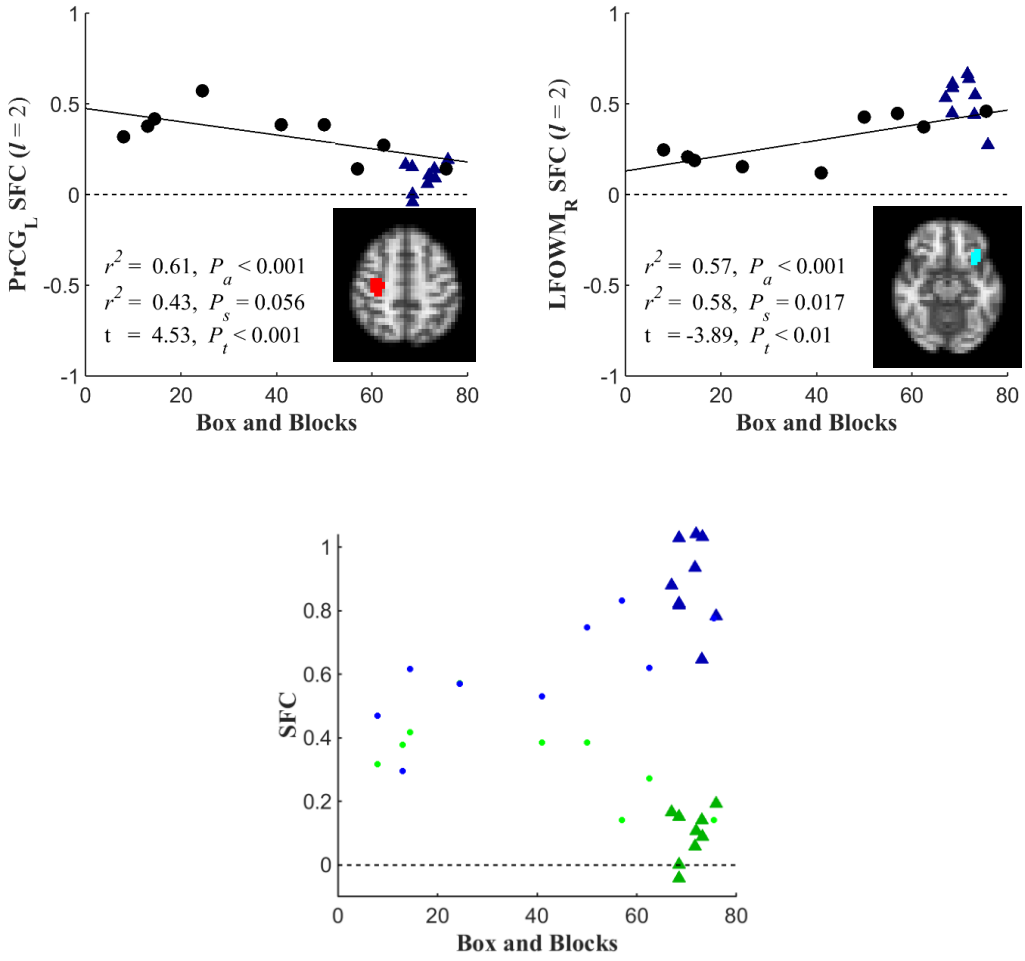

Figure 4-4: Scatter plots showing length-specific SFC group differences

Stroke survivors (circles) and controls (triangles), with Box and Blocks correlations.
a) Stroke survivors have increased functional connectivity of the ipsilesional/left precentral gyrus (PrCG_L) with surrounding structural connections within fiber distance interval *l*=2. b) The contralesional/right lateral frontoorbital gyrus (LFOG) has decreased functional connectivity at this fiber length. c) Scatter plot demonstrating an example of "structuro-functional equalization" of connectivity after stroke. Shown here is the structuro-functional correlation of the ipsilesional precentral gyrus at *l*=2 (green) and contralesional insula at *l*=1 (blue). In healthy adults (triangles), the precentral gyrus is not functionally connected to its structural neighbors at this particular fiber length. Likewise, the right insula has strong functional connections within a short fiber distance. In stroke subjects, the precentral gyrus increases its functional connectivity to structural neighbors at fiber length *l*=2 (40-70mm). Additionally, the contralesional insula becomes less connected.

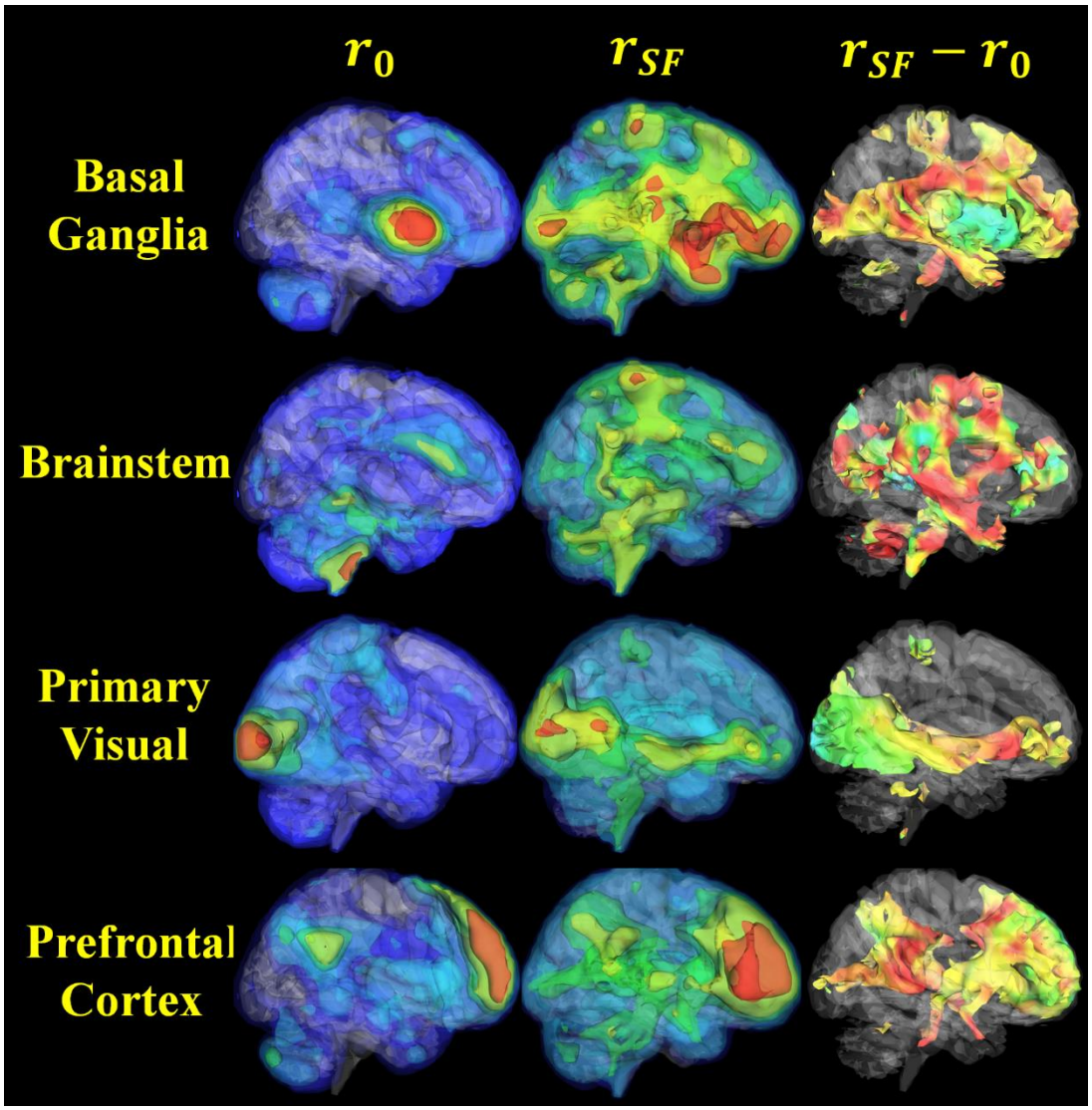

Figure 4-5: 3D visualization of SFC-enhanced resting-state networks.

Shown are four selected resting-state independent components from conventional MELODIC time-concatenated group ICA and the same components enhanced with the structuro-functional correlation metric. Voxels that are structurally connected to nodes from each network were enhanced intrinsically. Isosurface colors for individual r_0 and r_{SF} maps correspond to positive correlation coefficients of 0.3, 0.4, 0.5, 0.6, and 0.7. In the $r_{SF} - r_0$ column, an isovalue of 0.3 was extracted, and the surface is colored by $r_{SF} - r_0$ ranging from -1 to 1, , with Red: R = 1.0; Green: R = 0.0; Blue: R = -1.0.

4.3.4 The prefrontal cortex decreases its functional connectivity with its long-distance structural connections after stroke.

The prefrontal resting-state network decreases in functional connectivity with the posterior default-mode network and increases with lesioned motor network. As shown in Figure 4-6a, the SFC highlights additional areas in the posterior parietal cortex, the brainstem, and cerebellum. Differences between stroke survivors and controls reveal decreases within the cerebellum.

4.3.5 The cerebellum has decreased functional connectivity with structural connections to the prefrontal cortex.

Shown in Figure 4-6b and Table 4-3, control subjects have dilated indirect functional connectivity within cerebellum network's structural connections within frontal lobe. These enhancements are reduced in stroke survivors. This result compliments the previous finding that the cerebellum was reduced in the prefrontal network. The two lowest functioning stroke subjects, which had lesions to the right cerebellum and left pons, had the greatest reduction in the cerebellar network SFC map. Table 4-3 indicates that the contralesional inferior frontal gyrus has a lower SFC within the cerebellar network ($p < 0.01$), although this reduction is not correlated with Box and Blocks Score.

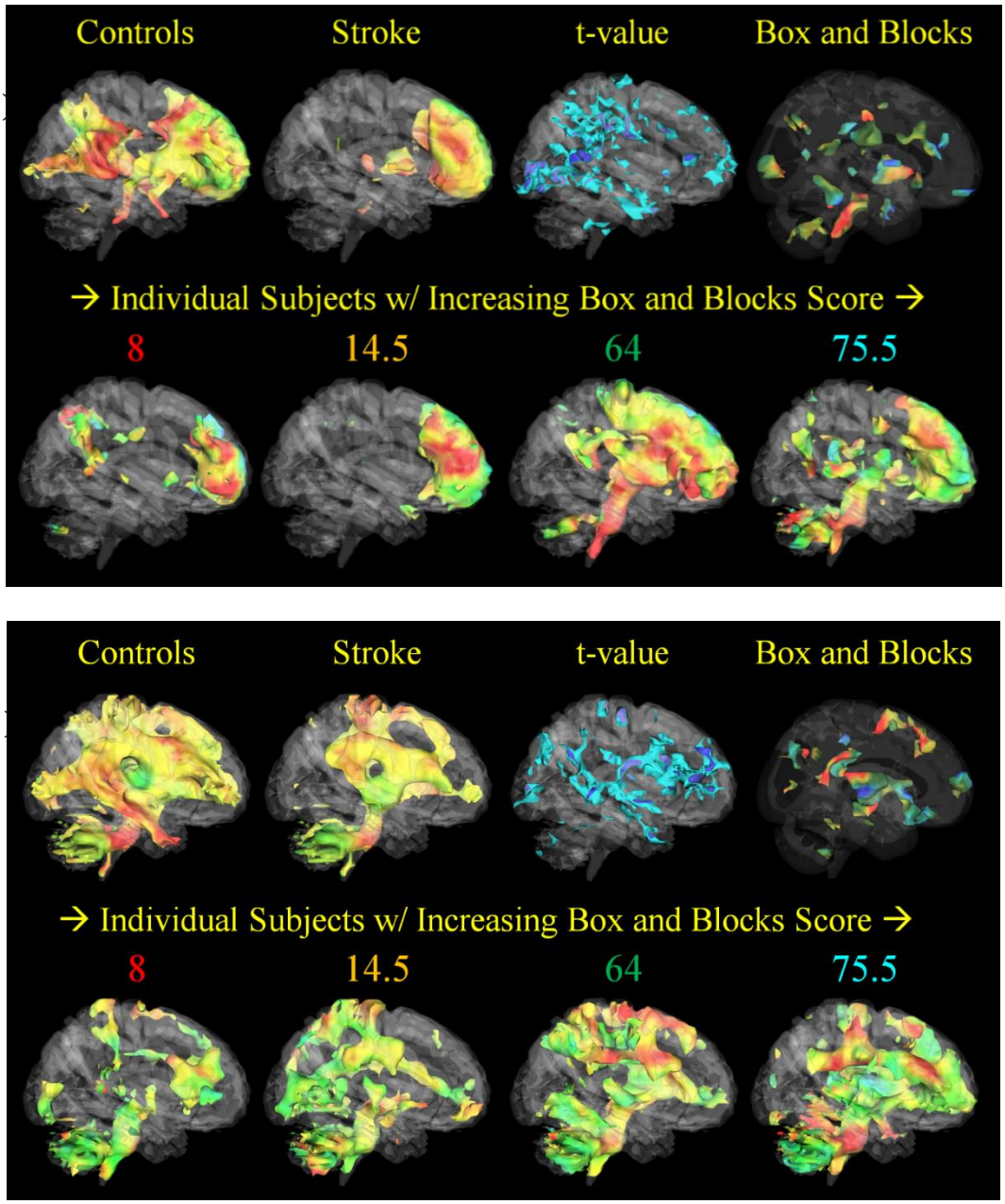

Figure 4-6: 3D visualization of functional trends in SFC-enhanced networks.

SFC-enhanced prefrontal (a) and cerebellar (b) resting-state networks are shown in stroke survivors, age-matched controls, and individual stroke subjects. Isosurfaces were extracted with r_{SF} = 0.3, and are colored based on the difference r_{SF} - r_0 . The "Box and Blocks" subpanel shows significant t-value clusters at p < 0.01, which are color-coded based on Box and Blocks correlation, with Red: R = 1.0; Green: R = 0.0; Blue: R = -1.0.

†: p < 0.05, ††: p < 0.01

Network	ROI	x	y	z	nVox	tmax	p (t)	R B&B	p (slope)
Cerebellum	IFG_R	46	35	12	166	-4.43	†† 0.00816	-0.593	0.08563
Prefrontal	MTG_R	46	-41	12	196	-5.70	†† 0.00053	0.762	† 0.01265
- - v - -	Fu_L	-42	-45	-16	103	-4.64	†† 0.00511	0.841	†† 0.00266
DMN ant	AG_L	-54	-45	40	460	-5.13	†† 0.00177	0.894	†† 0.00049
- - v - -	PreCu_L	-6	-61	40	298	-4.62	†† 0.00531	0.717	† 0.02422
- - v - -	SPG_R	30	-41	40	165	-4.31	† 0.01043	0.859	†† 0.00164
- - v - -	Ins_R	50	-1	0	106	-3.71	† 0.04035	-0.583	0.09310
aCingG	MFG_L	-34	63	4	113	-6.18	†† 0.00019	0.701	† 0.02863
dlPFC Left	SFG_R	18	-5	72	423	-5.55	†† 0.00070	0.953	†† 0.00002
- - v - -	STG_R	62	-33	20	177	-4.41	†† 0.00861	0.936	†† 0.00006
SMC Left	PrCG_R	26	-13	56	67	-3.36	0.08598	-0.780	†† 0.00936
Cerebellum	Thal_L	2	7	-20	553	-5.84	†† 0.00038	-0.755	† 0.01391
- - v - -	Ins_R	46	7	-8	121	-4.33	† 0.01003	-0.270	0.47865
Prefrontal	PreCun_L	-10	-29	28	167	-4.79	†† 0.00375	0.897	†† 0.00044
DMN ant	SFG_R	18	43	40	172	-5.01	†† 0.00231	-0.891	†† 0.00057
- - v - -	PreCu_R	6	-61	36	162	-7.01	†† 0.00004	-0.400	0.28083
- - v - -	SMG_L	-38	-29	20	109	-5.38	†† 0.00104	0.724	† 0.02215
dlPFC Right	MFWM_L	-18	51	28	110	4.99	†† 0.00240	0.847	†† 0.00220
dlPFC Left	ITG_R	50	3	-40	355	-5.73	†† 0.00050	0.856	†† 0.00177
- - v - -	LFOG_L	-22	27	-24	164	-5.17	†† 0.00158	0.842	†† 0.00258
- - v - -	PLIC_R	30	-17	4	101	-4.71031	†† 0.00444341	0.860	†† 0.00160
SMC Right	CGH_L	-14	-29	-8	141	5.29	†† 0.00125574	0.514	0.15032
- - v - -	SFG_R	26	31	40	104	5.05	†† 0.00212827	0.666	† 0.04369
- - v - -	PrCG_R	58	7	0	94	4.25	† 0.01152175	-0.425	0.24352
- - v - -	PoCG_L	-38	-25	52	6	-3.29	0.09858856	-0.507	0.15847
Salience	MTG_R	46	7	-28	105	-4.74	†† 0.00417189	0.787	†† 0.00788

Table 4-3: Voxel-based group differences in SFC-enhanced networks.

Clusters of significantly different voxels between stroke and age-matched controls are reported for the original resting-state network correlation coefficients (white background) and the same networks with SFC-enhancement (gray background). Acronyms: AG: angular gyrus, CGH: cingulate gyrus, Fu: fusiform gyrus, IFG: inferior frontal gyrus, Ins: insular cortex, ITG: inferior temporal gyrus, MFG: middle frontal gyrus, MFWM: middle frontal white matter, MTG: middle temporal gyrus, PoCG: postcentral gyrus, PrCG: precentral gyrus, PreCu: precuneus, SFG: superior frontal gyrus, SMG: supramarginal gyrus, SPG: superior parietal lobule, STG: superior temporal gyrus, Thal: thalamus.

Network acronyms: Salience: salience network nodes in anterior cingulate gyrus and bilateral insula, SMC: sensorimotor network and contralateral cerebellum, Cerebellum: bilateral cerebellum network, DMN ant: default-mode network anterior half, Prefrontal: prefrontal cortex near anterior surface, aCingG: anterior cingulate gyrus, dlPFC: dorsolateral prefrontal cortex

4.4 DISCUSSION AND CONCLUSIONS

The results indicate that structural connectivity can be used to estimate higher order expansions of conventional rest-state functional networks, and that these enhancements are predictive of both functional connectivity changes and motor function after stroke. Our new model of structural-functional connectivity successfully enhanced resting-state networks, and these changes correlated with motor function in stroke survivors. Structural and functional connectivity analyses were successfully married with our model.

The SFC index uniquely enhanced structurally connected regions to each resting-state network, making it viable extension to conventional ICA methods when structural connectivity information is also available**.** Our technique may be the first to explicitly fuse structural and functional connectivity by combining BOLD signals across fiber endpoints. We believe that our technique is the first to express each voxel's intrinsic functional connectivity distribution based on fiber length. This work is also the first to produce a new fMRI time course at each voxel that is a combined signal of its structural connections.

The structuro-functional correlation technique is different from others that combine structural and functional connectivity. Methods introduced in the past use structural connectivity to impose constraints on functional connectivity and dynamic causal models (Sporns et al., 2000; Stephan et al., 2009). The current approach attempts to enhance rather than constrain functional networks in order to estimate a broader network.

Although resting-state functional connectivity in itself can detect differences in stroke subjects that are correlated with function, SFC may predict the broader impact of lesions on these same networks. For example, our results suggest that the SFC enhances polysynaptic pathways between the sensorimotor cortex, pons, and contralateral cerebellum. This enhancement is reduced in individuals with stroke. Lu *et* al. found that local lesions to the pons led to reduced polysynaptic functional connectivity between the motor cortex, pons, and cerebellum (Lu et al., 2011). This polysynaptic pathway was revealed with SFC. This finding also underscores the importance of considering both the structural and functional properties of a network in assessing the impact of a lesion after stroke.

Stroke subjects had reduced functional connectivity between areas that are structurally connected at greater distances, as shown in Figure 4-2. These differences were notably seen in regions that are associated with nodes of the default-mode network. This result is consistent with studies that have found reduced anterior-posterior DMN connectivity in aging (Vidal-Piñeiro et al., 2014). Vidal-Pineiro *et al*. found that white matter integrity of the cingulum was correlated with reduced DMN functional connectivity in the aging population. The results in this study suggest that anterior-posterior DMN connectivity is also reduced after stroke when compared to age-matched individuals.

We found potential evidence of structuro-functional equalization of cortical networks after stroke, as shown in Figure 4-4. This also suggests that our model may be capable of measuring such forms of such phenomena. We speculate that after stroke,

reorganization may occur as a rebalancing or equalization of functional connections across residual structural pathways.

The intrinsic SFC_{max} metric was correlated with the Box and Blocks Score within the cerebellum and prefrontal cortex, suggesting that functional connectivity to the structural connections of these regions is important for motor function after stroke. The medial prefrontal cortex is densely connected to posterior parietal areas, forming the core of the default-mode network. It is possible that the nodes of integrative networks, such as the DMN or cerebellar networks, reorganization in connections in order to compensate for lost function after stroke. However, this speculation needs further evidence.

Combining structural and functional connectivity information overcomes the limitations of each individual analysis. A common limitation of diffusion MRI tractography is that voxels with crossing white matter fibers can lead to inaccurate structural mappings. Most tractography fibers originating in the cerebellum, for example, fail to cross at the pons, thus leading to many positive connections with the ipsilateral hemisphere and false negative connections with the contralateral hemisphere. In this study, we chose to exclude fibers that did not cross at the pons in order to mitigate the connectivity bias introduced by this limitation of tractography. However, it is known that there are in fact fibers that synapse at the red nucleus and influence the ipsilateral hemisphere. Thus, our technique was not able to detect these connections that may indeed play a role in alternative pathways after stroke.

Our approach shares many of the same limitations as functional MRI and diffusion MRI tractography. Functional connectivity MRI assumes that voxels with correlations in BOLD signal are co-active and thus functionally connected. Due to the

course temporal resolution of fMRI and the slow nature of the hemodynamic response, this modeled connectivity is left undirected. The accuracy of structural connectivity estimated by diffusion MRI tractography approaches is limited by the fiber orientation model. Models of the orientation distribution function at each voxel make the assumption that axon organization is the prime contributor to diffusion directionality.

Our technique also has unique limitations. Multiple assumptions made by our model must be considered. First, it assumes that every reconstructed fiber endpoint contains neurons that are connected to the neurons located at the other endpoint. Since there are cases in which reconstructed fibers terminate within the white matter, our current implementation occasionally mixes the BOLD signals of gray matter voxels with white matter voxels. These violations of our assumption led to the enhancement of white matter pathways within our resulting maps. Another limitation was the usage of deterministic tractography, which does not provide a connectivity distribution for every voxel as do probabilistic approaches. Probabilistic approaches are capable of generating more fibers from the cerebellum that cross at the brainstem, which would have been beneficial for studying the cerebellum's structural-functional connectivity. In the case of a stroke, there are alterations of the vasculature and white matter microstructure within and nearby the lesion that may impact the SFC model's assumptions.

The most important source of potential error in voxel-based approaches is intersubject and intermodality image registration. This study involved coregistration of functional, structural, and diffusion MRI within and between subjects. Each of these images has its own unique artifacts. Spatial distortions inherent to echo-planar imaging have different characteristics between diffusion and functional MRI, leading to a

nonlinear mapping between voxels. An additional field-correction map can be acquired before the EPI scan in order to correct the distortions. This study did not include this field-map in its acquisition. In order to improve mappings between diffusion and functional MRI spaces, a nonlinear deformable registration was performed on mean BOLD images between subjects. Such a registration between functional images has been subject to criticism.

In this study, respiration and cardiac cycle were not treated as coregressors, which leaves them as potential confounds. These physiological processes have been shown to introduce artifacts into resting-state connectivity analyses. It has been recommended that these data be collected during the scan and be treated as coregressors during the ICA and/or seed-based connectivity analyses. However, other investigators have argued against this correction measure since that there may be important cortical activity that is highly correlated with respiration and heart rate. Independent components that were determined to be related to artifact or noise were regressed out of our data before applying our analyses.

In conclusion, our novel analysis can detect changes in structure-function interactions in cortical networks after stroke. In future work, we would like to explore potential applications of independent component analysis to extract common patterns from our novel structurally filtered functional time-course datasets. Additionally, SFC will be validated with a publically available collection of young healthy adults.

CHAPTER 5: INTEGRATION OF RESULTS

5.1 SUMMARY OF RESULTS

5.1.1 Brief Summary

The scope of this dissertation was to detect voxel-level changes in connectivity-derived metrics within the brain after stroke in order to predict the greater impact on large-scale cortical networks and clinical outcomes. In Chapter 2, the results showed that the voxel-wise indirect structural connectivity (VISC) metric was able to detect stroke-related changes in cortical areas distant from the lesion. Specifically, the global structural connectivity to voxels within integrative association areas was correlated with level of motor impairment in chronic stroke survivors. Chapter 3 further investigated the role of multimodal sensory association areas within functional brain networks when engaged during movement. The results indicated that, after stroke, the nodes of integrative networks were less connected to one another, but they often had greater connectivity with the nodes of sensorimotor and visual networks. Additionally, the cerebellum appeared to have a central role in controlling these changes. Finally, in Chapter 4 the structure-function relationship in voxel-level connectivity after stroke was tested with a newly developed structuro-functional correlation (SFC) analysis. The SFC metric successfully enhanced functional resting-state networks with structural connectivity information. These enhancements within and between the cerebellum and prefrontal networks were significantly different in stroke survivors and were also correlated with motor function. Collectively, the results from these works suggest that global structural connectivity to integrative hubs allows for the brain to assist damaged

primary motor and sensory processing pathways during fine motor control. Furthermore, there is a close relationship between structure and function even in pathologic conditions following a stroke. Lastly, the cerebellum may play a central role in controlling these mechanistic changes in network topology.

5.1.2 Potential new insights into brain plasticity and motor recovery

The structuro-functional correlation technique introduced in this dissertation may resolve the black box that associates structural and functional connectivity with recovery after stroke. Resting-state motor networks enhanced by SFC account for both CST integrity and the strength of functional connections. Shown in Figure 5-1 is the left sensorimotor network in the stroke subject with the lowest Box and Blocks Score in this dissertation. The conventional resting-state network shows increased recruitment within the contralesional sensorimotor cortex. The lesion's influence on this increase is not clear. We may speculate that this subject had increased contralesional recruitment in order to control movement by the uncrossed corticospinal tract. The SFC-enhanced network reveals two additional unique insights. First, the ipsilesional pons is not enhanced due to the lesioned CST, which may explain the lack of recovery in this subject. Second, the contralesional pons had a positive SFC enhancement. Increased contralesional sensorimotor recruitment and an intact contralesional corticospinal tract were both necessary to achieve this enhancement. Thus, SFC may reveal details about the mechanisms behind cortical reorganization and their relationship with motor recovery.

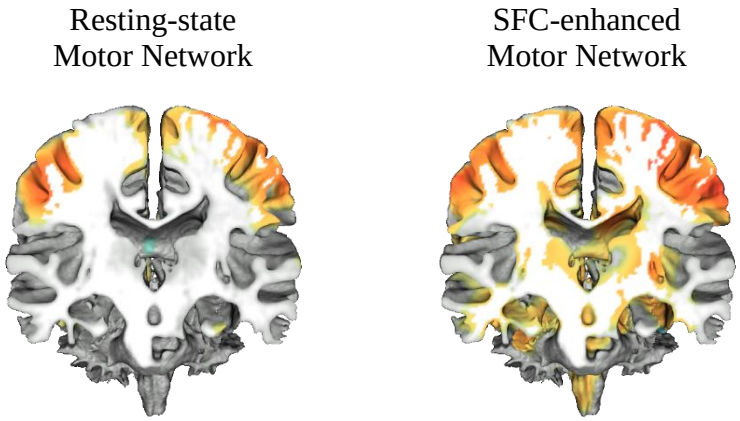

Figure 5-1: SFC motor network in lowest functioning stroke subject.

Comparison of the conventional resting-state motor network before and after being enhanced by structuro-functional correlation. Functional connectivity is used to color the gray matter, with hotter colors indicating greater network recruitment.

5.1.3 Translation to personalized rehabilitation strategies

The SFC-enhanced resting-state networks may be used to target system-specific recovery while selecting rehabilitation strategies. The residual structural and functional connectivity of the brain after stroke can be used to select a personalized treatment that maximizes functional outcomes. Such an algorithm for determining the optimal motor rehabilitation strategy based on brain connectivity was proposed by Stinear *et al*. (Stinear *et al.* 2010). Recovery, compensation, and substitution were distinguished as three possible goals of rehabilitation. The ideal goal is recovery, which involves regaining the ability to perform the same movements with the same effectors. When full recovery is not possible, compensation involves achieving a similar task by using the same effectors with altered movements. In the case that a stroke renders an effector dysfunctional, substitution involves using other effectors to complete a task (Stinear *et al.* 2010).

Shown in Figure 5-2, a similar algorithm was created here based on the results from this dissertation. Note that the images are from the same stroke patient as in Figure 5-1.

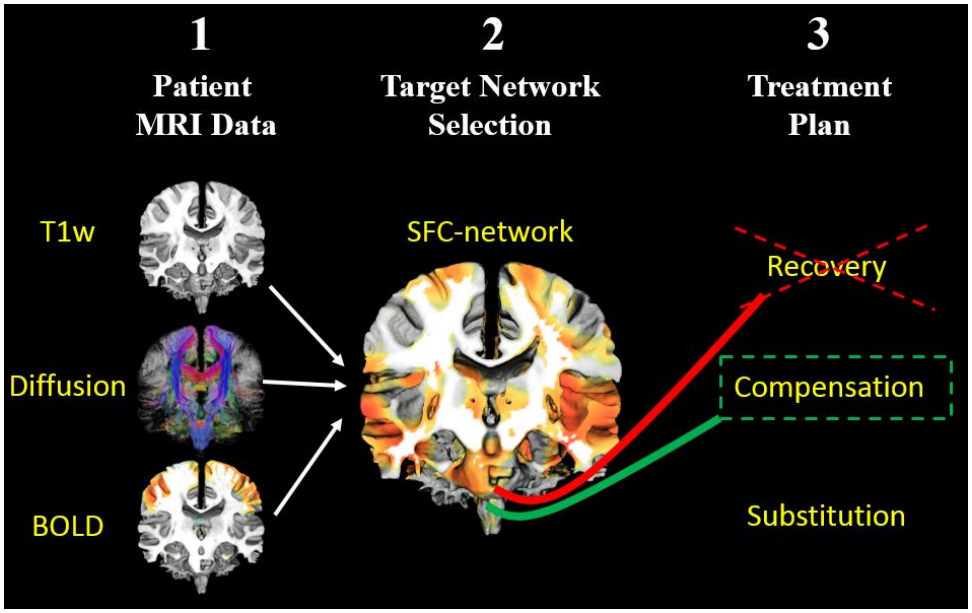

Figure 5-2: Personalized rehabilitation with SFC networks.

The first step is to collect structural MRI, diffusion MRI, and resting-state BOLD fMRI data. Second, the clinician would select a resting-state network to target with therapy. This network would be enhanced with the structuro-functional correlation (SFC) methods. The enhanced areas outside of the lesion would be used to select an appropriate treatment plan.

5.2 FUTURE INVESTIGATIONS

The structuro-functional correlation approach should be further developed and applied to further investigate differences in structure-function interactions of brain networks after stroke, particularly in the acute phase during recovery. If similar results can be reproduced with this technique in longitudinal studies, then it would confirm that the structural connectivity information in acute stroke can predict potential avenues for recovery in the context of brain connectivity. Furthermore, such findings would make patient-specific rehabilitation a reality in the near future.

CHAPTER 6: APPENDIX

6.1 VISC intersession and intersubject reproducibility

Intersubject and intersession reproducibility was a consideration when developing the VISC metric. However, the data collected in the first aim included exactly one scan per subject, making it impossible to test for intersession differences. While collecting data for the second and third aims, the HARDI protocol was repeated twice in one young healthy adult. These imaging sessions were performed on different days but with the same equipment and scan parameters. White matter fiber trajectories were calculated with the q-ball tractography methods used in Aim 3, and were then spatially normalized into MNI space using the subject's anatomical image registration result. The VISC metric was calculated in MNI space at a 4 mm isotropic resolution. At each voxel, **x**, the percent difference, $d(\mathbf{x})$, between the first session, $f_1(\mathbf{x})$, and second session $f_2(\mathbf{x})$ was used to estimate intersession reproducibility, with $d(\mathbf{x}) = \frac{|f_1(\mathbf{x}) - f_2(\mathbf{x})|}{\max(|f_1(\mathbf{x})|, |f_2(\mathbf{x})|)}$. In order to also estimate intersubject reproducibility, this VISC calculation was repeated for all stroke subjects and age-matched controls that were collected under the HARDI protocol. At each voxel, the intersubject coefficient of variation was calculated for the age-matched control group, with $\widehat{c_v} = \left(1 + \frac{1}{4n}\right)\frac{s}{\bar{x}}$, where n, $\bar{x}$, and s are the sample size, mean and standard deviation. In order to compare the reproducibility of other metrics, the $\widehat{c_v}$ was calculated for fractional anisotropy, VISC, the node degree (number of direct connections), the mean node degree of directly connected voxels. This analysis was

performed throughout the entire brain, but repeated for each of 170 regions from the Johns Hopkins Eve atlas.

Figure 6-1 shows the fractional anisotropy and VISC computed for the single young healthy control subject. The absolute percent difference between sessions throughout the brain was similar for FA (0.185 ± 0.061) and VISC (0.175 ± 0.083). However, the differences were greater in first-order node degree (0.944 ± 0.504) and second-order node degree (0.333 ± 0.160). This suggests that globally VISC has similar intersession reproducibility as fractional anisotropy. Shown on the right of Figure 6-1, FA had greater differences in gray matter areas, while VISC had lower intersession differences in these regions. Interregional variability in mean intersession difference was greater in VISC, suggesting it provided better intersession reproducibility for specific regions. In 122 of the 170 regions compared, VISC had a lower mean $|d|$. VISC had lower $|d|$ within the basal ganglia, thalamus, cerebellum, and gray matter cortical areas, while FA had lower $|d|$ within the occipital lobe and white matter tracts.

Intersubject reproducibility within the age-matched control group was similar to the intersession differences. Figure 6-2 shows the coefficient of variation for FA and VISC for stroke subjects and age-matched controls. The coefficient of variation between subjects for the whole brain was similar for FA (0.207 ± 0.072) and VISC (0.207 ± 0.066). However the VISC had lower variability in gray matter (0.212 ± 0.058) than white matter (0.255 ± 0.057), while FA was less variable in the white matter (0.224 ± 0.054) than gray matter (0.250 ± 0.064).

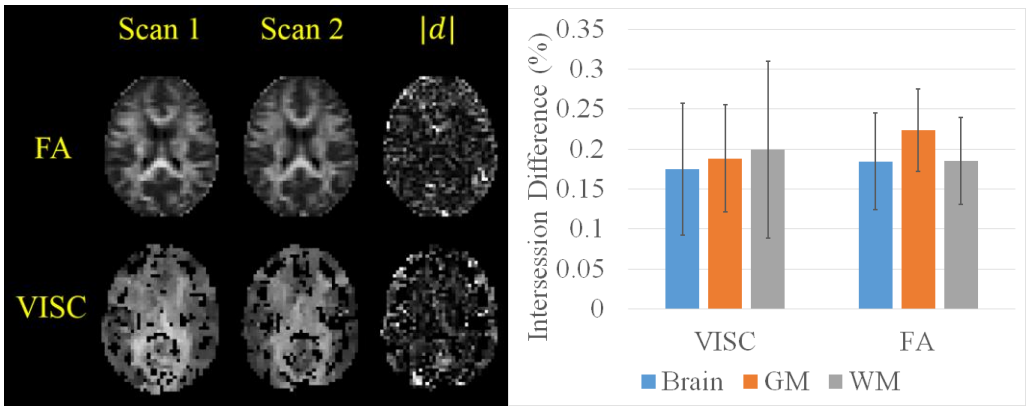

Figure 6-1: Intersession reproducibility of FA and VISC for one subject.

Comparison of two separate HARDI acquisitions (Scan 1 and Scan 2) within the same subject, showing differences in fractional anisotropy (FA) and voxel-based indirect structural connectivity (VISC). Left: Images of FA, VISC, and percent difference between scans. Right: Intersession differences for gray matter (GM), white matter (WM), and all brain regions. Error bars indicate standard deviation between voxels within each tissue type. Percentages are on scale of 0.0 to 1.0.

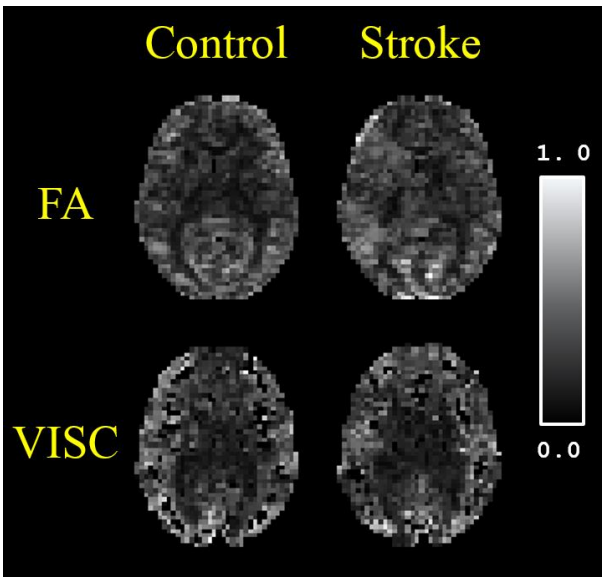

Figure 6-2: Coefficient of variation of FA and VISC in stroke and controls.

Comparison of intersubject coefficient of variation of stroke subjects and age-matched controls, shown for fractional anisotropy (FA) and voxel-based indirect structural connectivity (VISC).

6.2 Head motion and task performance differences in stroke subjects

Head motion during MRI data collection leads to spatial artifacts that contaminate connectivity measurements. Past literature has shown that patient populations often have greater head motion during MRI, even at rest. This leads to potential confounding factors that cannot be ignored in any study that tests differences between patient and control populations. Head movement during BOLD fMRI was estimated for all subjects that participated in Aims 2 and 3. Six 3D head motion parameters (3 rotations and 3 translations) were estimated at every time point by the MCFLIRT motion correction tool in FSL. The frame-to-frame absolute difference in head translation was calculated for every time point. With x_i, y_i, and z_i being the x, y, and z positions of the head at the ith time point, the average head translation was calculated as

$$\text{Total translation } = \frac{1}{T}\sum_{i=2}^{T}\sqrt{\begin{matrix}(x_i - x_{i-1})^2 \ + \\ (y_i - y_{i-1})^2 \ + \\ (z_i - z_{i-1})^2\end{matrix}}$$

The total head translation was calculated for every run and subject. Figure 6-3 shows the total head translation of the young adults, age-matched controls, and stroke survivors during the resting-state fMRI scan. There was a significant difference in total head translation between stroke and age-matched controls ($p < 0.05$) during all conditions.

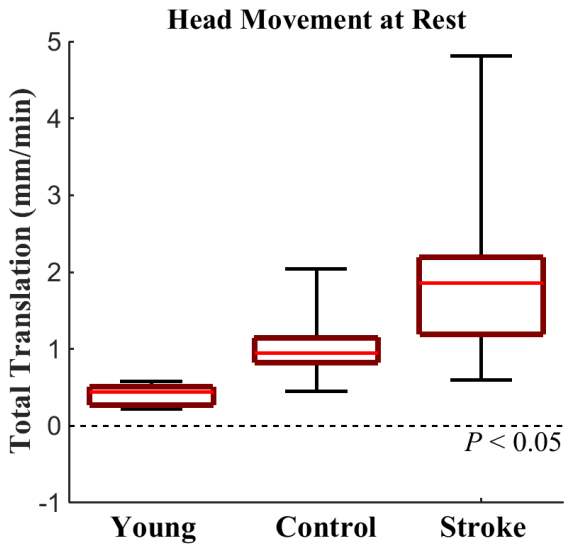

Figure 6-3: Comparison of head motion during the search task in Aim 2.

BIBLIOGRAPHY

Alexander, A.L., Hasan, K.M., Lazar, M., Tsuruda, J.S., Parker, D.L., 2001. Analysis of partial volume effects in diffusion-tensor MRI. Magn. Reson. Med. 45, 770–780. doi:10.1002/mrm.1105

Andersen, R. a., Cui, H., 2009. Intention, Action Planning, and Decision Making in Parietal-Frontal Circuits. Neuron 63, 568–583. doi:10.1016/j.neuron.2009.08.028

Ashburner, J., Friston, K.J., 2000. Voxel-based morphometry--the methods. Neuroimage 11, 805–21. doi:10.1006/nimg.2000.0582

Avants, B.B., Epstein, C.L., Grossman, M., Gee, J.C., 2008. Symmetric Diffeomorphic Image Registration with Cross-Correlation: Evaluating Automated Labeling of Elderly and Neurodegenerative Brain. Med Image Anal 12, 26–41.

Baarbé, J., Yielder, P., Daligadu, J., Behbahani, H., Haavik, H., Murphy, B., 2014. A novel protocol to investigate motor training-induced plasticity and sensorimotor integration in the cerebellum and motor cortex. J. Neurophysiol. 111, 715–21. doi:10.1152/jn.00661.2013

Bamiou, D.-E., Werring, D., Cox, K., Stevens, J., Musiek, F.E., Brown, M.M., Luxon, L.M., 2012. Patient-reported auditory functions after stroke of the central auditory pathway. Stroke 43, 1285–9. doi:10.1161/STROKEAHA.111.644039

Basser, P.J., Mattiello, J., LeBihan, D., 1994. MR diffusion tensor spectroscopy and imaging. Biophys. J. 66, 259–67. doi:10.1016/S0006-3495(94)80775-1

Bates, E., Wilson, S.M., Saygin, A.P., Dick, F., Sereno, M.I., Knight, R.T., Dronkers, N.F., 2003. Voxel-based lesion–symptom mapping. Nat. Neurosci. 6, 448–450. doi:10.1038/nn1050

Bauer, C.C.C., Pasaye, E.H., Romero-romo, J.I., Barrios, F.A., 2012. The Integrative Role of the Basal Ganglia.

Beckmann, C.F., Smith, S.M., 2005. Tensorial extensions of independent component analysis for multisubject FMRI analysis. Neuroimage 25, 294–311. doi:10.1016/j.neuroimage.2004.10.043

Beckmann, C.F., Smith, S.M., 2004. Probabilistic independent component analysis for functional magnetic resonance imaging. IEEE Trans. Med. Imaging 23, 137–52. doi:10.1109/TMI.2003.822821

Beckmann, Mackay, Filippini, Smith, 2009. Group comparison of resting-state FMRI data using multi-subject ICA and dual regression. Neuroimage 47, S148. doi:10.1073/pnas.0811879106

Beg, M., Miller, M., Trouvé, A., Younes, L., 2005. Computing large deformation metric mappings via geodesic flows of diffeomorphisms. IJCV 61, 139–157.

Behrens, T.E.J., Berg, H.J., Jbabdi, S., Rushworth, M.F.S., Woolrich, M.W., 2007. Probabilistic diffusion tractography with multiple fibre orientations: What can we gain? Neuroimage 34, 144–155. doi:10.1016/j.neuroimage.2006.09.018

Behrens, T.E.J., Woolrich, M.W., Jenkinson, M., Johansen-Berg, H., Nunes, R.G., Clare, S., Matthews, P.M., Brady, J.M., Smith, S.M., 2003. Characterization and propagation of uncertainty in diffusion-weighted MR imaging. Magn. Reson. Med. 50, 1077–88. doi:10.1002/mrm.10609

Beurze, S.M., Lange, F.P. De, Toni, I., Medendorp, W.P., 2007. Integration of Target and Effector Information in the Human Brain During Reach Planning Integration of Target and Effector Information in the Human Brain During Reach Planning 188–199. doi:10.1152/jn.00456.2006

Biswal, B., Yetkin, F.Z., Haughton, V.M., Hyde, J.S., 1995. Functional connectivity in the motor cortex of resting human brain using echo-planar MRI. Magn. Reson. Med. 34, 537–41.

Bohannon, R.W., Smith, M.B., 1987. Interrater reliability of a modified Ashworth scale of muscle spasticity. Phys. Ther. 67, 206–7.

Bonan, I. V., Colle, F.M., Guichard, J.P., Vicaut, E., Eisenfisz, M., Tran Ba Huy, P., Yelnik, A.P., 2004. Reliance on Visual Information after Stroke. Part I: Balance on Dynamic Posturography. Arch. Phys. Med. Rehabil. 85, 268–273. doi:10.1016/j.apmr.2003.06.017

Bookstein, F.L., 2001. "Voxel-based morphometry" should not be used with imperfectly registered images. Neuroimage 14, 1454–62. doi:10.1006/nimg.2001.0770

Bosnell, R. a, Kincses, T., Stagg, C.J., Tomassini, V., Kischka, U., Jbabdi, S., Woolrich, M.W., Andersson, J., Matthews, P.M., Johansen-Berg, H., 2011. Motor practice promotes increased activity in brain regions structurally disconnected after subcortical stroke. Neurorehabil. Neural Repair 25, 607–16. doi:10.1177/1545968311405675

Buch, E.R., Modir Shanechi, A., Fourkas, A.D., Weber, C., Birbaumer, N., Cohen, L.G., 2012. Parietofrontal integrity determines neural modulation associated with grasping imagery after stroke. Brain 135, 596–614. doi:10.1093/brain/awr331

Budde, M., Frank, J., 2010. Neurite beading is sufficient to decrease the apparent diffusion coefficient after ischemic stroke. Proc. Natl. Acad. Sci. USA 107, 14472–14477. doi:10.1073/pnas.1004841107/-/DCSupplemental.www.pnas.org/cgi/doi/10.1073/pnas.1004841107

Bullmore, E., Sporns, O., 2009. Complex brain networks: graph theoretical analysis of structural and functional systems. Nat. Rev. Neurosci. 10, 186–98. doi:10.1038/nrn2575

Castellanos, F.X., Di Martino, A., Craddock, R.C., Mehta, A.D., Milham, M.P., 2013. Clinical applications of the functional connectome. Neuroimage 80, 527–540. doi:10.1016/j.neuroimage.2013.04.083

Chenevert, T.L., Brunberg, J.A., Pipe, J.G., 1990. Anisotropic diffusion in human white matter: demonstration with MR techniques in vivo. Radiology 177, 401–405. doi:10.1148/radiology.177.2.2217776

Cheng, L., Wu, Z., Fu, Y., Miao, F., Sun, J., Tong, S., 2012. Reorganization of functional brain networks during the recovery of stroke: A functional MRI study. Conf Proc IEEE Eng Med Biol Soc 2012, 4132–4135. doi:10.1109/EMBC.2012.6346876

Douek, P., Turner, R., Pekar, J., Patronas, N., Le Bihan, D., 1991. MR color mapping of myelin fiber orientation. J. Comput. Assist. Tomogr. doi:10.1097/00004728-199111000-00003

Du, Y., Fan, Y., 2013. Group information guided ICA for fMRI data analysis. Neuroimage 69, 157–197. doi:10.1016/j.neuroimage.2012.11.008

Dukart, J., Bertolino, A., 2014. When structure affects function - The need for partial volume effect correction in functional and resting state magnetic resonance imaging studies. PLoS One 9, 1–18. doi:10.1371/journal.pone.0114227

Evans, A.C., 2013. Networks of anatomical covariance. Neuroimage 80, 489–504. doi:10.1016/j.neuroimage.2013.05.054

Filimon, F., 2010. Human cortical control of hand movements: parietofrontal networks for reaching, grasping, and pointing. Neuroscientist 16, 388–407. doi:10.1177/1073858410375468

Filimon, F., Nelson, J.D., Huang, R.-S., Sereno, M.I., 2009. Multiple parietal reach regions in humans: cortical representations for visual and proprioceptive feedback during on-line reaching. J. Neurosci. 29, 2961–71. doi:10.1523/JNEUROSCI.3211-08.2009

Forn, C., Rocca, M. a, Boscá, I., Casanova, B., Sanjuan, a, Filippi, M., 2013. Analysis of "task-positive" and "task-negative" functional networks during the performance of the Symbol Digit Modalities Test in patients at presentation with clinically isolated syndrome suggestive of multiple sclerosis. Exp. brain Res. 225, 399–407. doi:10.1007/s00221-012-3380-5

Friston, K.J., 1994. Functional and effective connectivity in neuroimaging: A synthesis. Hum. Brain Mapp. 2, 56–78. doi:10.1002/hbm.460020107

Fugl-Meyer, A.R., 1975. THE POST-STROKE HEMIPLEGIC PATIENT. Scand. J. Rehab. Med. 7, 13–31.

Funes, J., Guzma, A., 2009. Pleasant music overcomes the loss of awareness. Star 106.

Grefkes, C., Fink, G.R., 2014. Connectivity-based approaches in stroke and recovery of function. Lancet Neurol. 13, 206–216. doi:10.1016/S1474-4422(13)70264-3

Grefkes, C., Fink, G.R., 2011. Reorganization of cerebral networks after stroke: New insights from neuroimaging with connectivity approaches. Brain 134, 1264–1276. doi:10.1093/brain/awr033

Grefkes, C., Nowak, D.A., Eickhoff, S.B., Dafotakis, M., Küst, J., Karbe, H., Fink, G.R., 2008. Cortical connectivity after subcortical stroke assessed with functional magnetic resonance imaging. Ann. Neurol. 63, 236–246. doi:10.1002/ana.21228

Greicius, M.D., Supekar, K., Menon, V., Dougherty, R.F., 2009. Resting-state functional connectivity reflects structural connectivity in the default mode network. Cereb. Cortex 19, 72–8. doi:10.1093/cercor/bhn059

Hagmann, P., Cammoun, L., Gigandet, X., Meuli, R., Honey, C.J., Wedeen, V.J., Sporns, O., 2008. Mapping the structural core of human cerebral cortex. PLoS Biol. 6, e159. doi:10.1371/journal.pbio.0060159

Hagmann, P., Kurant, M., Gigandet, X., Thiran, P., Wedeen, V.J., Meuli, R., Thiran, J.-P., 2007. Mapping human whole-brain structural networks with diffusion MRI. PLoS One 2, e597. doi:10.1371/journal.pone.0000597

Horn, A., Ostwald, D., Reisert, M., Blankenburg, F., 2013. The structural-functional connectome and the default mode network of the human brain. Neuroimage 102, 142–151. doi:10.1016/j.neuroimage.2013.09.069

Hyvarinen, A., 1999. Fast and robust fixed-point algorithms for independent component analysis. Neural Networks, IEEE Trans. 10, 626–634.

James, T.W., Stevenson, R.A., 2015. Chapter 8 The Use of fMRI to Assess Multisensory Integration 1–20. doi:NBK92856 [bookaccession]

Jang, S., Cho, S., Kim, Y., Han, B., 2005. Diffusion anisotrophy in the early stages of stroke can predict motor outcome. Restor. Neurol. Neurosci. 23, 11–7.

Jenkinson, M., Bannister, P., Brady, M., Smith, S., 2002. Improved Optimization for the Robust and Accurate Linear Registration and Motion Correction of Brain Images. Neuroimage 17, 825–841. doi:10.1006/nimg.2002.1132

Jenkinson, M., Smith, S., 2001. A global optimisation method for robust affine registration of brain images. Med. Image Anal. 5, 143–156. doi:10.1016/S1361-8415(01)00036-6

Jiang, L., Xu, H., Yu, C., 2013. Brain connectivity plasticity in the motor network after ischemic stroke. Neural Plast. 2013, 924192. doi:10.1155/2013/924192

Joel, S.E., Caffo, B.S., Van Zijl, P.C.M., Pekar, J.J., 2011. On the relationship between seed-based and ICA-based measures of functional connectivity. Magn. Reson. Med. 66, 644–657. doi:10.1002/mrm.22818

Johansson, B.B., 2011. Current trends in stroke rehabilitation. A review with focus on brain plasticity. Acta Neurol. Scand. 123, 147–159. doi:10.1111/j.1600-0404.2010.01417.x

Kandel, E.R., Schwartz, J.H., Jessell, T.M., 2000. Principles of neural science (4th ed.), 4th ed. McGraw-Hill, Health Professions Division, New York.

Keir, S.L., Wardlaw, J.M., 2000. Systematic review of diffusion and perfusion imaging in acute ischemic stroke. Stroke. 31, 2723–2731.

Kötter, R., Sommer, F.T., 2000. Global relationship between anatomical connectivity and activity propagation in the cerebral cortex. Philos. Trans. R. Soc. Lond. B. Biol. Sci. 355, 127–34. doi:10.1098/rstb.2000.0553

Kuceyeski, A., Maruta, J., Niogi, S.N., Ghajar, J., Raj, A., 2011. The generation and validation of white matter connectivity importance maps. Neuroimage 58, 109–21. doi:10.1016/j.neuroimage.2011.05.087

Lang, C.E., Schieber, M.H., 2004. Reduced muscle selectivity during individuated finger movements in humans after damage to the motor cortex or corticospinal tract. J. Neurophysiol. 91, 1722–33. doi:10.1152/jn.00805.2003

Li, S., Eloyan, A., Joel, S., Mostofsky, S., Pekar, J., Bassett, S.S., Caffo, B., 2012. Analysis of group ICA-based connectivity measures from fMRI: application to Alzheimer's disease. PLoS One 7, e49340. doi:10.1371/journal.pone.0049340

Lindenberg, R., Renga, V., Zhu, L.L., Betzler, F., Alsop, D., Schlaug, G., 2010. Structural integrity of corticospinal motor fibers predicts motor impairment in chronic stroke. Neurology 74, 280–287. doi:10.1212/WNL.0b013e3181ccc6d9

Lotze, M., Beutling, W., Loibl, M., Domin, M., Platz, T., Schminke, U., Byblow, W.D., 2012. Contralesional Motor Cortex Activation Depends on Ipsilesional Corticospinal Tract Integrity in Well-Recovered Subcortical Stroke Patients. Neurorehabil. Neural. Repair 26, 594–603. doi:10.1177/1545968311427706

Lu, J., Liu, H., Zhang, M., Wang, D., Cao, Y., Ma, Q., Rong, D., Wang, X., Buckner, R.L., Li, K., 2011. Focal Pontine Lesions Provide Evidence That Intrinsic Functional Connectivity Reflects Polysynaptic Anatomical Pathways. J. Neurosci. 31, 15065–15071. doi:10.1523/JNEUROSCI.2364-11.2011

Marchini, J.L., Ripley, B.D., 2000. A new statistical approach to detecting significant activation in functional MRI. Neuroimage 12, 366–80. doi:10.1006/nimg.2000.0628

Mathiowetz, V., Volland, G., Kashman, N., Weber, K., 1985. Adult norms for the Box and Block Test of manual dexterity. Am. J. Occup. Ther. 39, 386–391.

Meskaldji, D.E., Fischi-Gomez, E., Griffa, A., Hagmann, P., Morgenthaler, S., Thiran, J.-P.P., 2013. Comparing connectomes across subjects and populations at different scales. Neuroimage 80, 416–425. doi:10.1016/j.neuroimage.2013.04.084

Minka, T., 2000. Automatic choice of dimensionality for PCA. NIPS 1–16.

Mori, S., Crain, B., Chacko, V., Zijl, P. Van, 1999. Three-• dimensional tracking of axonal projections in the brain by magnetic resonance imaging. Ann. Neurol. 45, 265–9.

Murphy, T.H., Corbett, D., 2009. Plasticity during stroke recovery: from synapse to behaviour. Nat. Rev. Neurosci. 10, 861–72. doi:10.1038/nrn2735

Nagy, A., Eördegh, G., Paróczy, Z., Márkus, Z., Benedek, G., 2006. Multisensory integration in the basal ganglia. Eur. J. Neurosci. 24, 917–24. doi:10.1111/j.1460-9568.2006.04942.x

Nielsen, J. a., Zielinski, B. a., Ferguson, M. a., Lainhart, J.E., Anderson, J.S., 2013. An Evaluation of the Left-Brain vs. Right-Brain Hypothesis with Resting State Functional Connectivity Magnetic Resonance Imaging. PLoS One 8. doi:10.1371/journal.pone.0071275

Ogawa, S., Lee, T., 1990. Brain magnetic resonance imaging with contrast dependent on blood oxygenation. Proc. … 87, 9868–72. doi:10.1073/pnas.87.24.9868

Oishi, K., Faria, A., Jiang, H., Li, X., Akhter, K., 2009. -based whole brain white matter analysis using large deformation diffeomorphic metric mapping: application to normal elderly and Alzheimer's disease participants. Neuroimage 46, 486–499.

Olivot, J.M., Mlynash, M., Thijs, V.N., Kemp, S., Lansberg, M.G., Wechsler, L., Schlaug, G., Bammer, R., Marks, M.P., Albers, G.W., 2008. Relationships between infarct growth, clinical outcome, and early recanalization in diffusion and perfusion imaging for understanding stroke evolution (DEFUSE). Stroke 39, 2257–2263. doi:10.1161/STROKEAHA.107.511535

Park, B., Kim, D.-S., Park, H.-J., 2014. Graph independent component analysis reveals repertoires of intrinsic network components in the human brain. PLoS One 9, e82873. doi:10.1371/journal.pone.0082873

Promjunyakul, N., Schmit, B.D., Schindler-Ivens, S.M., 2015. A novel fMRI paradigm suggests that pedaling-related brain activation is altered after stroke. Front. Hum. Neurosci. 09, 324. doi:10.3389/fnhum.2015.00324

Proville, R.D., Spolidoro, M., Guyon, N., Dugué, G.P., Selimi, F., Isope, P., Popa, D., Léna, C., 2014. Cerebellum involvement in cortical sensorimotor circuits for the control of voluntary movements. Nat. Neurosci. 17, 1233–1239. doi:10.1038/nn.3773

Pynn, L.K., DeSouza, J.F.X., 2013. The function of efference copy signals: Implications for symptoms of schizophrenia. Vision Res. 76, 124–133. doi:10.1016/j.visres.2012.10.019

Raichle, M.E., MacLeod, a M., Snyder, a Z., Powers, W.J., Gusnard, D. a, Shulman, G.L., 2001. A default mode of brain function. Proc. Natl. Acad. Sci. USA 98, 676–82. doi:10.1073/pnas.98.2.676

Ray, K.L., McKay, D.R., Fox, P.M., Riedel, M.C., Uecker, A.M., Beckmann, C.F., Smith, S.M., Fox, P.T., Laird, A.R., 2013. ICA model order selection of task co-activation networks. Front. Neurosci. 7, 237. doi:10.3389/fnins.2013.00237

Rehme, A.K., Fink, G.R., von Cramon, D.Y., Grefkes, C., 2011. The role of the contralesional motor cortex for motor recovery in the early days after stroke assessed with longitudinal FMRI. Cereb. Cortex 21, 756–68. doi:10.1093/cercor/bhq140

Rehme, A.K., Grefkes, C., 2013. Cerebral network disorders after stroke: evidence from imaging-based connectivity analyses of active and resting brain states in humans. J. Physiol. 591, 17–31. doi:10.1113/jphysiol.2012.243469

Riley, J.D., Le, V., Der-Yeghiaian, L., See, J., Newton, J.M., Ward, N.S., Cramer, S.C., 2011. Anatomy of stroke injury predicts gains from therapy. Stroke 42, 421–6. doi:10.1161/STROKEAHA.110.599340

Roberts, T.P.L., Liu, F., Kassner, A., Mori, S., Guha, A., 2005. Fiber density index correlates with reduced fractional anisotropy in white matter of patients with glioblastoma. AJNR 26, 2183–6.

Romero-Romo, J.I., Bauer, C.C.C., Pasaye, E.H., Gutierrez, R.A., Favila, R., Barrios, F.A., 2010. Abnormal Functioning of the Thalamocortical System Underlies the Conscious Awareness of the Phantom Limb Phenomenon. Neuroradiol. J. 23, 671–679. doi:10.1177/197140091002300605

Rordorf, G., Koroshetz, W.J., Copen, W. a, Cramer, S.C., Schaefer, P.W., Budzik, R.F., Schwamm, L.H., Buonanno, F., Sorensen, a G., Gonzalez, G., 1998. Regional ischemia and ischemic injury in patients with acute middle cerebral artery stroke as defined by early diffusion-weighted and perfusion-weighted MRI. Stroke. 29, 939–943. doi:10.1161/01.STR.29.5.939

Rubinov, M., Sporns, O., 2011. Weight-conserving characterization of complex functional brain networks. Neuroimage 56, 2068–79. doi:10.1016/j.neuroimage.2011.03.069

Rubinov, M., Sporns, O., 2010. Complex network measures of brain connectivity: uses and interpretations. Neuroimage 52, 1059–69. doi:10.1016/j.neuroimage.2009.10.003

Rytty, R., Nikkinen, J., Paavola, L., Abou Elseoud, A., Moilanen, V., Visuri, A., Tervonen, O., Renton, A.E., Traynor, B.J., Kiviniemi, V., Remes, A.M., 2013. GroupICA dual regression analysis of resting state networks in a behavioral variant of frontotemporal dementia. Front. Hum. Neurosci. 7, 461. doi:10.3389/fnhum.2013.00461

Schaechter, J., Fricker, Z., 2009. Microstructural status of ipsilesional and contralesional corticospinal tract correlates with motor skill in chronic stroke patients. Hum. Brain Mapp. 30, 3461–3474. doi:10.1002/hbm.20770.Microstructural

Scheinost, D., Benjamin, J., Lacadie, C.M., Vohr, B., Schneider, K.C., Ment, L.R., Papademetris, X., Constable, R.T., 2012. The intrinsic connectivity distribution: A novel contrast measure reflecting voxel level functional connectivity. Neuroimage 62, 1510–1519. doi:10.1016/j.neuroimage.2012.05.073

Seitz, R.J., Meisel, S., Weller, P., Junghans, U., Wittsack, H.-J., Siebler, M., 2005. Initial ischemic event: perfusion-weighted MR imaging and apparent diffusion coefficient for stroke evolution. Radiology 237, 1020–1028. doi:10.1148/radiol.2373041435

Sharma, N., Baron, J.-C., Rowe, J.B., 2009. Motor imagery after stroke: Relating outcome to motor network connectivity. Ann. Neurol. 66, 604–616. doi:10.1002/ana.21810

Smith, S.M., 2002. Fast robust automated brain extraction. Hum. Brain Mapp. 17, 143–55. doi:10.1002/hbm.10062

Smith, S.M., Beckmann, C.F., Andersson, J., Auerbach, E.J., Bijsterbosch, J., Douaud, G., Duff, E., Feinberg, D. a., Griffanti, L., Harms, M.P., Kelly, M., Laumann, T., Miller, K.L., Moeller, S., Petersen, S., Power, J., Salimi-Khorshidi, G., Snyder, A.Z., Vu, A.T., Woolrich, M.W., Xu, J., Yacoub, E., Uğurbil, K., Van Essen, D.C., Glasser, M.F., 2013. Resting-state fMRI in the Human Connectome Project. Neuroimage 80, 144–168. doi:10.1016/j.neuroimage.2013.05.039

Smith, S.M., Jenkinson, M., Johansen-Berg, H., Rueckert, D., Nichols, T.E., Mackay, C.E., Watkins, K.E., Ciccarelli, O., Cader, M.Z., Matthews, P.M., Behrens, T.E.J., 2006. Tract-based spatial statistics: voxelwise analysis of multi-subject diffusion data. Neuroimage 31, 1487–505. doi:10.1016/j.neuroimage.2006.02.024

Sporns, O., 2013. The human connectome: Origins and challenges. Neuroimage 80, 53–61. doi:10.1016/j.neuroimage.2013.03.023

Sporns, O., 2011. The human connectome: a complex network. Ann. N. Y. Acad. Sci. 1224, 109–25. doi:10.1111/j.1749-6632.2010.05888.x

Sporns, O., Tononi, G., Edelman, G.M., 2000. Theoretical neuroanatomy: relating anatomical and functional connectivity in graphs and cortical connection matrices. Cereb. Cortex 10, 127–41.

Sporns, O., Tononi, G., Kötter, R., 2005. The human connectome: A structural description of the human brain. PLoS Comput. Biol. 1, e42. doi:10.1371/journal.pcbi.0010042

Stephan, K.E., Tittgemeyer, M., Knösche, T.R., Moran, R.J., Friston, K.J., 2009. Tractography-based priors for dynamic causal models. Neuroimage 47, 1628–38. doi:10.1016/j.neuroimage.2009.05.096

Stinear, C.M., Barber, P.A., Smale, P.R., Coxon, J.P., Fleming, M.K., Byblow, W.D., 2007. Functional potential in chronic stroke patients depends on corticospinal tract integrity. Brain 130, 170–180. doi:10.1093/brain/awl333

Thirion, J.-P., 1998. Image matching as a diffusion process: an analogy with Maxwell's demons. Med. Image Anal. 2, 243–260.

Thomalla, G., Glauche, V., Koch, M. a, Beaulieu, C., Weiller, C., Röther, J., 2004. Diffusion tensor imaging detects early Wallerian degeneration of the pyramidal tract after ischemic stroke. Neuroimage 22, 1767–74. doi:10.1016/j.neuroimage.2004.03.041

Tuch, D.S., 2004. Q-ball imaging. Magn. Reson. Med. 52, 1358–1372. doi:10.1002/mrm.20279

Tuch, D.S., Reese, T.G., Wiegell, M.R., 2003. Diffusion MRI of Complex Neural Architecture. Neuron 40, 885–895. doi:10.1016/S0896-6273(03)00758-X

Tuch, D.S., Reese, T.G., Wiegell, M.R., Makris, N., Belliveau, J.W., Van Wedeen, J., 2002. High angular resolution diffusion imaging reveals intravoxel white matter fiber heterogeneity. Magn. Reson. Med. 48, 577–582. doi:10.1002/mrm.10268

Van den Heuvel, M.P., Hulshoff Pol, H.E., 2010. Exploring the brain network: a review on resting-state fMRI functional connectivity. Eur. Neuropsychopharmacol. 20, 519–34. doi:10.1016/j.euroneuro.2010.03.008

Van Dijk, K.R.A., Sabuncu, M.R., Buckner, R.L., 2012. The influence of head motion on intrinsic functional connectivity MRI. Neuroimage 59, 431–438. doi:10.1016/j.neuroimage.2011.07.044

Van Essen, D.C., Smith, S.M., Barch, D.M., Behrens, T.E.J., Yacoub, E., Ugurbil, K., 2013. The WU-Minn Human Connectome Project: An overview. Neuroimage 80, 62–79. doi:10.1016/j.neuroimage.2013.05.041

Vidal-Piñeiro, D., Valls-Pedret, C., Fernández-Cabello, S., Arenaza-Urquijo, E.M., Sala-Llonch, R., Solana, E., Bargalló, N., Junqué, C., Ros, E., Bartrés-Faz, D., 2014. Decreased Default Mode Network connectivity correlates with age-associated structural and cognitive changes. Front. Aging Neurosci. 6, 256. doi:10.3389/fnagi.2014.00256

Wang, L., Yu, C., Chen, H., Qin, W., He, Y., Fan, F., Zhang, Y., Wang, M., Li, K., Zang, Y., Woodward, T.S., Zhu, C., 2010. Dynamic functional reorganization of the motor execution network after stroke. Brain 133, 1224–38. doi:10.1093/brain/awq043

Ward, N.S., 2005. Plasticity and the functional reorganization of the human brain. Int. J. Psychophysiol. 58, 158–61. doi:10.1016/j.ijpsycho.2005.02.009

Ward, N.S., Brown, M.M., Thompson, a J., Frackowiak, R.S.J., 2003. Neural correlates of motor recovery after stroke: a longitudinal fMRI study. Brain 126, 2476–96. doi:10.1093/brain/awg245

Wieloch, T., Nikolich, K., 2006. Mechanisms of neural plasticity following brain injury. Curr. Opin. Neurobiol. 16, 258–264. doi:10.1016/j.conb.2006.05.011

Wolf, S.L., Catlin, P.A., Ellis, M., Archer, A.L., Morgan, B., Piacentino, A., 2001. Assessing Wolf motor function test as outcome measure for research in patients after stroke. Stroke. 32, 1635–9.

Yeh, F.-C., Tang, P.-F., Tseng, W.-Y.I., 2013. Diffusion MRI connectometry automatically reveals affected fiber pathways in individuals with chronic stroke. NeuroImage. Clin. 2, 912–21. doi:10.1016/j.nicl.2013.06.014

Yeo, B.T.T., Krienen, F.M., Sepulcre, J., Sabuncu, M.R., Lashkari, D., Hollinshead, M., Roffman, J.L., Smoller, J.W., Zollei, L., Polimeni, J.R., Fischl, B., Liu, H., Buckner, R.L., 2011. The organization of the human cerebral cortex estimated by intrinsic functional connectivity. J. Neurophysiol. 106, 1125–1165. doi:10.1152/jn.00338.2011.

Zhang, W., Olivi, A., Hertig, S.J., Zijl, P. Van, 2009. Automated Fiber Tracking of Human Brain White Matter Using Diffusion Tensor Imaging. Neuroimage 42, 771–777. doi:10.1016/j.neuroimage.2008.04.241.Automated

Zhu, L.L., Lindenberg, R., Alexander, M.P., Schlaug, G., 2010. Lesion load of the corticospinal tract predicts motor impairment in chronic stroke. Stroke 41, 910–5. doi:10.1161/STROKEAHA.109.577023

Zuo, X.N., Kelly, C., Adelstein, J.S., Klein, D.F., Castellanos, F.X., Milham, M.P., 2010. Reliable intrinsic connectivity networks: Test-retest evaluation using ICA and dual regression approach. Neuroimage 49, 2163–2177. doi:10.1016/j.neuroimage.2009.10.080